

STATUS OF THESIS

Title of thesis

Development of An Optical Strain Measurement Method

I KHOO SZE WEI

hereby allow my thesis to be placed at the Information Resource Center (IRC) of Universiti Teknologi PETRONAS (UTP) with the following conditions:

1. The thesis becomes the property of UTP
2. The IRC of UTP may make copies of the thesis for academic purposes only.
3. This thesis is classified as

Confidential

Non-confidential

If this thesis is confidential, please state the reason:

The contents of the thesis will remain confidential for _____ years.

Remarks on disclosure:

Endorsed by

Signature of Author

Signature of Supervisor

Permanent address:

9, Lebuhrapat Baru 2,
Taman Song Choon,
31350 Ipoh, Perak,
Malaysia.

Name of Supervisor

Dr. Saravanan Karuppanan

Date : _____

Date : _____

UNIVERSITI TEKNOLOGI PETRONAS

DEVELOPMENT OF AN OPTICAL STRAIN MEASUREMENT METHOD

by

KHOO SZE WEI

The undersigned certify that they have read, and recommend to the Postgraduate Studies Programme for acceptance this thesis for the fulfilment of the requirements for the degree stated.

Signature: _____

Main Supervisor: _____

Signature: _____

Co-Supervisor: _____

Signature: _____

Head of Department: _____

Date: _____

DEVELOPMENT OF AN OPTICAL STRAIN MEASUREMENT METHOD

by

KHOO SZE WEI

A Thesis

Submitted to the Postgraduate Studies Programme

as a Requirement for the Degree of

MASTER OF SCIENCE

MECHANICAL ENGINEERING DEPARTMENT

UNIVERSITI TEKNOLOGI PETRONAS

BANDAR SERI ISKANDAR,

PERAK

JULY 2011

DECLARATION OF THESIS

Title of thesis

Development of An Optical Strain Measurement Method

I KHOO SZE WEI
hereby declare that the thesis is based on my original work except for quotations and citations which have been duly acknowledged. I also declare that it has not been previously or concurrently submitted for any other degree at UTP or other institutions.

Witnessed by

Signature of Author

Signature of Supervisor

Permanent address:

Name of Supervisor

9, Lebuhrapat Baru 2,
Taman Song Choon,
31350 Ipoh, Perak,
Malaysia.

Dr. Saravanan Karuppanan

Date : _____

Date : _____

ACKNOWLEDGEMENTS

My utmost gratitude is dedicated to my supervisor, Dr. Saravanan Karuppanan and my co. supervisor, Mr. Muhamad Ridzuan Bin Abdul Latif for their excellent guidance and support. I would like to thank both of them personally as their supervision and caring nature whenever I faced problem have more or less given me the encouragement to finish my research study. Besides, their confidences in me by giving me numerous challenging tasks, have given me a lot of learning opportunities.

I would like to extend my appreciation to Assoc. Prof. Dr. Mustafar Bin Sudin, Assoc. Prof. Dr. Patthi Bin Hussain, Dr. Mohamad Zaki Bin Abdullah and Dr. Azmi Bin Abdul Wahab who have provided me the advices and invaluable ideas. At the same time, their affluent experiences have also enhanced my knowledge in the field of strain analysis.

Last but no means least, I would like to thank my family, friends, lab technicians who have contributed in a way or another to the completion of my research study. I am deeply grateful for their remarkable assistance offered unconditionally to me.

ABSTRACT

Strain measurement is important in mechanical testing. There are many strain measurement methods; namely electrical resistance strain gauge, extensometer, Geometric Moiré technique, optical strain measurement method and *etc.* Each method has its own advantages and disadvantages. There is always a need to develop a precise and yet simple strain measurement method in mechanical testing. The objective of this study is to develop a two-dimensional measurement algorithm that calculates the strain in a loaded structural component. This can be achieved by using the Digital Image Correlation technique which compares the displacement of the random speckles pattern in the reference (undeformed) and the deformed images. In the development of the strain measurement algorithm, it was coded into MATLAB program by using the MATLAB's Image Processing Toolbox. Next, the tensile tests were conducted where two types of samples made of mild steel and polypropylene materials were tested using the Universal Testing Machine. Simultaneously, videos were recorded using a consumer version of high-definition video camera. The recorded videos (images) were then analyzed and the strain values were determined by using the optical strain measurement method (MATLAB program). In the results and discussions section, the stress-strain curves were plotted for the mild steel and the polypropylene specimens. From the stress-strain curves, the modulus of elasticity of the respective materials was determined and the results determined by the extensometer and the optical strain measurement method were compared to each other. The obtained results had been verified as the modulus of elasticity of the mild steel and the polypropylene specimens were found to be 5.14% and 2.35% off the benchmark values respectively. A good agreement was achieved upon comparison between the results determined by the two methods mentioned above. In conclusion, the two-dimensional deformation measurement algorithm had been successfully developed.

ABSTRAK

Pengukuran terikan adalah penting dalam ujian mekanik. Terdapat banyak kaedah pengukuran terikan iaitu tolok terikan, *extensometer*, teknik Moiré geometri, kaedah pengukuran terikan optik dan lain-lain. Setiap kaedah memiliki kelebihan dan kekurangan yang tersendiri. Dengan demikian, sentiasa ada keperluan untuk membangunkan suatu kaedah pengukuran terikan yang tepat, namun mudah dalam ujian mekanik. Tujuan kajian ini adalah untuk mengembangkan algoritma dua dimensi ukuran yang menghitung terikan dalam komponen struktur yang sedang disaratkan. Ini dapat dicapai dengan membandingkan perpindahan pola bintik rawak yang ada dalam imej rujukan (asal) and imej yang bercacat dari segi bentuk. Bagi pengembangan algoritma pengukuran terikan, ia diberikan kod dan ditukar menjadi program MATLAB dengan menggunakan *Image Processing Toolbox* dalam MATLAB. Selanjutnya, ujikaji ketegangan dilakukan di mana dua jenis sampel yang dibuat daripada keluli lembut dan polipropilena diuji dengan menggunakan *Universal Testing Machine*. Serentakannya, video direkodkan dengan menggunakan versi pengguna kamera video definisi tinggi sepanjang ujikaji ketegangan. Video (imej) yang diambil kemudian dianalisis dan nilai terikan diperolehi dengan menggunakan kaedah pengukuran terikan optik (program MATLAB). Pada bahagian keputusan dan perbincangan, garis lengkung tegasan-terikan diplotkan untuk sampel keluli lembut dan polipropilena. Dari garis lengkung tegasan-terikan yang diplotkan, modulus elastisitas bagi sampel masing-masing ditentukan dan keputusan yang diperolehi daripada *extensometer* dan kaedah pengukuran terikan optik dibandingkan antara satu sama lain. Keputusan yang diperolehi telah disahkan kerana modulus elastisitas bagi sampel keluli lembut dan polipropilena hanya didapati 5.14% dan 2.35% lari daripada nilai penanda aras. Perbezaan yang amat kecil telah diperolehi pada perbandingan antara keputusan yang ditentukan oleh dua kaedah yang disebutkan di atas. Kesimpulannya, algoritma pengukuran deformasi dua dimensi telah berjaya dibangunkan.

In compliance with the terms of the Copyright Act 1987 and the IP Policy of the university, the copyright of this thesis has been reassigned by the author to the legal entity of the university,

Institute of Technology PETRONAS Sdn Bhd.

Due acknowledgement shall always be made of the use of any material contained in, or derived from, this thesis.

© KHOO SZE WEI, 2011

Institute of Technology PETRONAS Sdn Bhd

All rights reserved.

TABLE OF CONTENTS

STATUS OF THESIS	i
APPROVAL PAGE	ii
TITLE PAGE	iii
DECLARATION	iv
ACKNOWLEDGEMENTS	v
ABSTRACT.....	vi
ABSTRAK	vii
COPYRIGHT PAGE	viii
TABLE OF CONTENTS	ix
LIST OF TABLES	xii
LIST OF FIGURES	xiii
NOMENCLATURES	xvi
Chapter	
1. INTRODUCTION	1
1.1 Chapter Overview	1
1.2 Definition of Strain.....	1
1.3 Analysis of Strain	2
1.4 Strain Measurement Methods.....	2
1.4.1 Scratch Strain Gauge	3
1.4.2 Electrical Resistance Strain Gauge	4
1.4.3 Extensometer	5
1.4.4 Brittle Coating Method	5
1.4.5 Photoelasticity.....	6
1.4.6 Photoelastic-Coating Method	7
1.4.7 Geometric Moiré Technique	9
1.4.8 Holographic Interferometry	10
1.4.9 Digital Image Correlation	11
1.5 Problem Statement	12
1.6 Objectives.....	13
1.7 Scope of Study	14
1.8 Chapter Summary.....	14

2.	LITERATURE REVIEW	15
2.1	Chapter Overview	15
2.2	Fundamental Concepts of Digital Image Correlation	15
2.3	Development of the Digital Image Correlation Algorithms	19
2.4	Accuracy Analysis of the Digital Image Correlation.....	31
2.5	Applications of the Digital Image Correlation in 2D Measurement	33
2.6	Chapter Summary.....	35
3.	METHODOLOGY	37
3.1	Chapter Overview	37
3.2	Validation of the Geometric Approach Equation.....	39
3.2.1	Numerical Analysis by ANSYS Simulation Models.....	40
3.2.1.1	Pre-Processing Phase	41
3.2.1.2	Processing Phase	44
3.2.1.3	Post-Processing Phase.....	45
3.2.2	Analytical Analysis by Microsoft Excel Spreadsheet	50
3.3	Development of the Strain Measurement Algorithm.....	53
3.4	Development of the MATLAB Program	55
3.4.1	Input the Two Images that were Acquired at Two Different States.....	55
3.4.2	Enter the Image Resolution	55
3.4.3	Conversion of the Images' Format and the Enhancement of the Images' Features	57
3.4.4	Selection of the Four Speckles from the Random Speckles Pattern.....	58
3.4.5	Determination of the Speckles' Centroid	58
3.4.6	Conversion of the Centroid's Unit.....	59
3.4.7	Embed the Geometric Approach Equation and Perform the Calculations	59
3.4.8	Displaying the Obtained Results in the MATLAB Command Windows.....	60
3.5	Verification of the Optical Strain Measurement Method with AutoCAD Images.....	61
3.6	Preparation of the Samples and the Experimental Set-Up.....	62
3.6.1	Mild Steel Samples	62
3.6.2	Polypropylene Samples	64
3.6.3	Experimental Set-Up	65
3.7	Performing the Tensile Test and Recording of the Videos during the Strain Inducing Event.....	68
3.8	Validation of the Optical Strain Measurement Method with the Experimental Results	69
3.9	Chapter Summary.....	71

4. RESULTS AND DISCUSSIONS	74
4.1 Chapter Overview	74
4.2 Validation of the Geometric Approach Equation.....	74
4.3 Verification of the Optical Strain Measurement Method with AutoCAD Images	78
4.4 Validation of the Optical Strain Measurement Method with the Experimental Results.....	79
4.4.1 Mild Steel Specimens	81
4.4.2 Polypropylene Specimens.....	84
4.4.3 Comparison of the Specimens' Material Properties	88
4.4.3.1 Mild Steel Specimens.....	88
4.4.3.2 Polypropylene Specimens	89
4.5 Chapter Summary.....	91
 5. CONCLUSIONS AND FUTURE WORK.....	 95
5.1 Conclusions	95
5.2 Future Work	98
 REFERENCES.....	 99
 PUBLICATIONS	 107
 APPENDICES	
A. Mild Steel Certificate	
B. Two-Dimensional Strain Measurement MATLAB Program	
C. Stress-Strain Curves for the Mild Steel Specimens	
D. Stress-Strain Curves for the Polypropylene Specimens	
E. Determination of the Modulus of Elasticity For the Mild Steel Specimens	
F. Determination of the Modulus of Elasticity For the Polypropylene Specimens	

LIST OF TABLES

Table 2.1 The development and the improvement of the DIC algorithms	30
Table 2.2 The accuracy analysis of the DIC algorithms	32
Table 2.3 The applications of the DIC in two-dimensional measurements	34
Table 3.1 Parameters for the modelling of mild steel and polypropylene samples ...	41
Table 3.2 Dimensions of the mild steel specimen	63
Table 3.3 Dimensions of the polypropylene specimen	64
Table 3.4 Settings for the video camera and the light sources	68
Table 4.1 Comparison of the strain values for two-dimensional models	75
Table 4.2 Comparison of the strain values for three-dimensional models	75
Table 4.3 Verification of the optical strain measurement method	78
Table 4.4 Comparison of the modulus of elasticity determined by the extensometer and the optical strain measurement method	89
Table 4.5 Comparison of the modulus of elasticity determined by the extensometer and the optical strain measurement method	91

LIST OF FIGURES

Fig. 1.1 Scratch strain gauge	3
Fig. 1.2 Actual scratch on the brass disc	3
Fig. 1.3 Electrical resistance strain gauge	4
Fig. 1.4 Axial extensometer with 50 mm gauge length and $\pm 5\%$ measuring range .	5
Fig. 1.5 The crack patterns on the connecting rod	6
Fig. 1.6 The calibrator and the strain scale	6
Fig. 1.7 Fringe pattern observed in photoelasticity method.....	7
Fig. 1.8 Reflection polariscope	8
Fig. 1.9 Basic arrangements for reflection polariscope.....	8
Fig. 1.10 Moiré interference fringes	9
Fig. 1.11 Holographic Interferometry setup.....	10
Fig. 1.12 Images at two different states	11
Fig. 2.1 The aperture problem for a line in an image.....	16
Fig. 2.2 Schematic diagram of the experiment set-up for DIC system	19
Fig. 2.3 Digital intensities for a 10×10 subset	20
Fig. 2.4 Schematic diagram of a planar object undergoing deformation process	20
Fig. 2.5 Gray Scale images	26
Fig. 2.6 The speckle coordinates in an image	27
Fig. 2.7 The orientations of the line element PQ in the reference image	28
Fig. 3.1 Project work flow of this study.....	38
Fig. 3.2 Meshing of two-dimensional bar model	42
Fig. 3.3 Meshing of three-dimensional bar model	42
Fig. 3.4 Boundary conditions for the two-dimensional bar model	43
Fig. 3.5 Boundary conditions for the three-dimensional bar model	44
Fig. 3.6 Results obtained by ANSYS for two-dimensional mild steel models	46
Fig. 3.7 Results obtained by ANSYS for three-dimensional polypropylene models	48

Fig. 3.8 Cartesian coordinates of the nodes in the undeformed model.....	49
Fig. 3.9 Displacements of the respective nodes in x direction after deformation	49
Fig. 3.10 Nodes' Cartesian coordinates entered in the Microsoft Excel spreadsheets	50
Fig. 3.11 The embedded Geometric Approach equation in the Microsoft Excel spreadsheets	52
Fig. 3.12 Work flow for the development of the strain measurement algorithm.....	54
Fig. 3.13 The image resolutions of the images in y direction	56
Fig. 3.14 The image resolutions of the images in x direction	57
Fig. 3.15 Selection of the four speckles from the random speckles pattern	58
Fig. 3.16 Labelling of the selected speckles according to the number in sequence ..	59
Fig. 3.17 The obtained strain values in the MATLAB command windows	60
Fig. 3.18 Images with white dots created by AutoCAD software	61
Fig. 3.19 The shape of the mild steel specimen.....	62
Fig. 3.20 Mild steel specimen with black random speckles pattern	63
Fig. 3.21 The shape of the polypropylene specimen	64
Fig. 3.22 Polypropylene specimen with black random speckles pattern	65
Fig. 3.23 Schematic diagram of the experimental set-up.....	66
Fig. 3.24 Mirror image used to prevent out-of-plane displacement	67
Fig. 3.25 The equipment used in the tensile test.....	69
Fig. 3.26 Elongation values extracted from the data logger	70
Fig. 4.1 The embedded Geometric Approach equation in the Microsoft Excel spreadsheet.....	77
Fig. 4.2 Calculation of the important properties from the tensile test data in Microsoft Excel spreadsheet.....	80
Fig. 4.3 Stress-strain curve for the mild steel specimen	81
Fig. 4.4 Yield point phenomenon of the mild steel specimen	82
Fig. 4.5 Luders Bands observed in the captured images.....	83
Fig. 4.6 Stress-strain curve for the polypropylene specimen.....	85
Fig. 4.7 Necking observed during the tensile test.....	86
Fig. 4.8 Determination of the modulus of elasticity for the mild steel specimen	88

Fig. 4.9 Determination of the modulus of elasticity for the polypropylene specimen 90

NOMENCLATURES

ε	Normal strain
γ	Shear strain
ΔL	Change in length
L_o	Original length
CCD	Charge-Coupled device
CMOS	Complementary Metal-Oxide-Semiconductor
DIC	Digital Image Correlation
CGH	Computer-Generated Hologram
FAS	Fast and Simple
GCV	Generalized Cross-Validation
FFT	Fast-Fourier Transform
$f(x, y)$	Intensity patterns corresponding to the reflected light from the reference (undeformed) specimens
$f^*(x^*, y^*)$	Intensity patterns corresponding to the reflected light from the deformed specimens
S	Subimage in the reference state
S^*	Subimage in the deformed state
u_p	In-plane displacement of point P in x direction
v_p	In-plane displacement of point P in y direction
x	Position of x in the reference image (x -axis)
x^*	The translated position of x in the deformed image (x -axis)
u	In-plane displacement for x direction
y	Position of y in the reference image (y -axis)
y^*	The translated position of y in the deformed image (y -axis)
v	In-plane displacement for y direction
C	Cross-correlation coefficient
$\frac{\partial u}{\partial x}$	Displacement derivative of point P (differentiation of u in terms of x direction)

$\frac{\partial u}{\partial y}$	Displacement derivative of point P (differentiation of u in terms of y direction)
$\frac{\partial v}{\partial x}$	Displacement derivative of point P (differentiation of v in terms of x direction)
$\frac{\partial u}{\partial y}$	Displacement derivative of point P (differentiation of v in terms of y direction)
$f^*(x + \xi, y + \eta)$	Intensity values of the deformed subset
dA	Derivative of the area of scanning
ξ	Total displacement in the x direction
η	Total displacement in the y direction
Δx	Distance between point P and point Q in x direction
Δy	Distance between point P and point Q in y direction
Δz	Distance between point P and point Q in z direction
x_p	Coordinate of point P in the subset S (x -axis)
y_p	Coordinate of point P in the subset S (y -axis)
x^*_p	Coordinate of point P in the subset S^* (x -axis)
y^*_p	Coordinate of point P in the subset S^* (y -axis)
u_p	Displacement of point P in x direction
v_p	Displacement of point P in y direction
$f(x_p, y_p)$	Intensity values at point P for the reference image
$f^*(x^*_p, y^*_p)$	Intensity values at point P for the deformed image
ΔP_i	Initial guess for the six deformation parameters
$H(P_i)$	Hessian matrix
$\nabla (P_i)$	Jacobian matrix
W_o	Out-of-plane component
u_x	First order displacement gradient
u_{xx}	Second order displacement gradient
X_c	Centroid coordinate in x -axis
Y_c	Centroid coordinate in y -axis
x_i	Pixel coordinate in x -axis
y_i	Pixel coordinate in y -axis
Δa_i	Pixel area
A	Sum of the number of pixels in the total area

ε_{PQ}	Relative change in distance between point P and Q
Δs	Length of PQ
Δs^*	Length of P^*Q^*
ε_{xx}	Normal strain in x -axis
ε_{yy}	Normal strain in y -axis
ε_{zz}	Normal strain in z -axis
ε_{xy}	Shear strain in xy -plane
ε_{xz}	Shear strain in xz -plane
ε_{yz}	Shear strain in yz -plane
θ_x	Orientation of the line element PQ in the reference image (x -axis)
θ_y	Orientation of the line element PQ in the reference image (y -axis)
θ_z	Orientation of the line element PQ in the reference image (z -axis)
σ	Stress vector
D	Elastic stiffness matrix
ε^{el}	Elastic strain vector
UTM	Universal Testing Machine
RGB	Red, green and blue
JPEG	Joint Photographic Experts Group
ASTM	American Society for Testing and Materials
ISO	International Organization for Standardization
EDM	Electrical-Discharge Machining

CHAPTER 1

INTRODUCTION

1.1 Chapter Overview

The knowledge of strain is vital to the engineers as it plays an important role in most of the engineering designs and experimental works. As a result, the strain measurement becomes ultimately important in many engineering applications since the manmade structures and machines are getting more complex than before. In this chapter, the basic concept of the strain analysis was studied and various types of the strain measurement methods were reviewed. Next, the problem statement, objectives and the scope of study are presented in this chapter.

1.2 Definition of Strain

When a force is applied to a body, there is a change in the body's shape and size called deformation. More specifically, this deformation is referred as strain. Strain can be resolved into two categories, normal strain and shear strain which are denoted by ε and γ respectively [1]. Normal strain is defined as the change in dimension per unit length of a stressed element in a particular direction. Since the normal strain is the ratio of change in length, ΔL over the original length, L_o , it is a dimensionless quantity (the numerator and denominator have the same units in length) and expressed as in./in. or cm/cm [2]. For the sign convention, the normal strain is considered positive when the load produces an increase in length and negative when the load produces a decrease in length.

While for the shear strain, it is also a dimensionless radian and is defined as the change in angle of the initial right angle of a stressed element [3]. In other words, the

length of the element in the x , y , and z directions do not elongate or shorten when the shear stresses are applied on it, only the shape of the element get distorted and becomes a rhomboid. For the sign convention, it is assumed that the faces oriented toward the positive directions of the axes as the positive faces and vice versa. Hence, the shear strain is considered positive when the angle between two positive (or two negative) faces is reduced and negative when the angle between two positive (or two negative) faces is increased [4].

1.3 Analysis of Strain

The knowledge of strain is vital to the engineers as it plays an important role in most of the engineering designs and experimental works. For example, almost all the engineering designs are adopting small strain analysis. It means only small deformations are allowed and most of the structural members are designed to be rigid or the deformations are barely noticeable. This assumption has been widely adopted in engineering and it is assumed that the normal strain that occurs within a structural members are very small compared to the value of 1 [5].

In the experimental works, strain is very important as it is a directly measurable quantity while stress is not. Furthermore, misnomer happens as the people addressed this experimental works as experimental stress analysis although strain is normally measured and stress is calculated afterwards using stress-strain relationship [6]. The majority of the strain measurement in loaded structural components is carried out in two-dimension. For example, the extensions or normal strains in x and y directions are regularly being measured [7]. Since strain has a direct relationship to the stress, it is used to calculate the stress during the structural analysis when the material properties are known. On the other hand, the material properties of a sample are determined by using the known stress and the measured strain.

1.4 Strain Measurement Methods

In the 21st century, the manmade structures and machines are getting more complex than before. As a result, the strain measurement becomes ultimately important in many engineering applications and most of the time, the obtained strain values are

used to visualise the strength problems in a structural member. Thus, a precise strain measurement method is needed as a misleading result might cause a catastrophic incident and also put human lives in jeopardy. In order to overcome this situation, different types of strain measurement methods are invented as described below.

1.4.1 Scratch Strain Gauge

Scratch strain gauge is a mechanical strain measurement device capable to measure and record the total deformation within the length of the scratch gauge. The scratch strain gauge consists of two main parts, first is the recording stylus and the second is the brass recording disc as shown in Fig. 1.1. This device is attached to the specimen by clamping, screwing or bonding the ends of each base plate. The working principle for this scratch strain gauge is when the structure is deformed during the dynamic events, the stylus scratch the disc and record the total deformation as the two plates move relative to each other [8]. Fig. 1.2 shows the actual scratch on the brass disc. The scratched disc is analyzed with a microscope to obtain the peak-to-peak strains. Besides, the strains are determined by using the lasers or optical telescopes to evaluate the motion of scratched marks [9].

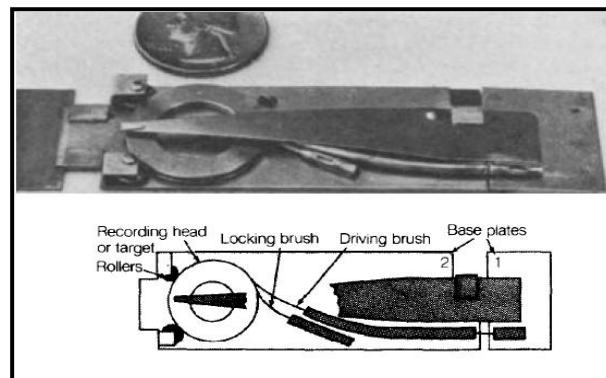


Fig. 1.1 Scratch strain gauge [8]

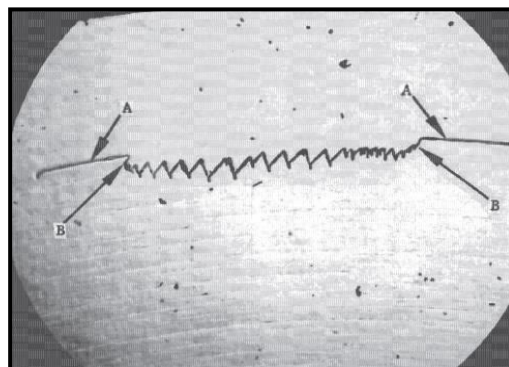


Fig. 1.2 Actual scratch on the brass disc

1.4.2 Electrical Resistance Strain Gauge

In the earlier years, the electrical resistance strain gauges as shown in Fig. 1.3 are the most versatile device used to measure surface deformation for the structural members and machines. The working principle for these strain gauges is that the electrical resistance of a metal wire varies with strain. By using the ordinary ohmmeter, it is difficult to measure the strain accurately since the resistance change in a strain gauge is very small. Therefore, a more practical Wheatstone bridge is invented and used to measure the strain precisely. These strain gauges actually take advantage of the physical property of electrical conductance's and conductor geometry. For example, when an electrical conductor elongates under a tensile load within the limits of elasticity, it will become narrower and longer. These changes will increase the electrical resistance continuously or vice-versa. Since a typical strain gauge is constructed with a long and thin conductive strip in a zigzag pattern of parallel lines, a small amount of load will create a large amount of strain over the effective length of the conductor [10]. Hence, a small amount of stress in strain gauges will change the resistance dramatically and provides precise result in strain measurement.

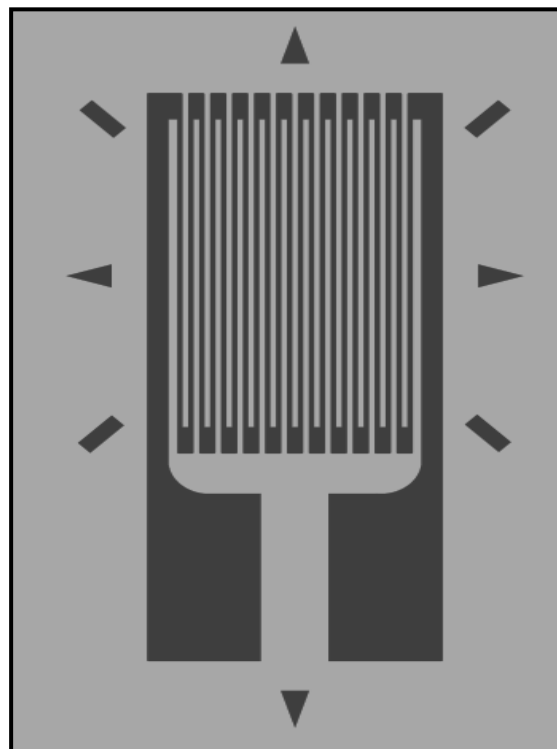


Fig. 1.3 Electrical resistance strain gauge

1.4.3 Extensometer

During a tensile test, the extensometer as shown in Fig. 1.4 is used to measure the elongation or axial strain by clipping it on the specimen. Normally the extensometers have fixed gauge lengths of 10, 25 or 50 mm and a measuring range of 5% to 100% strain. Extensometers are capable to measure the elongation for a wide range of materials, i.e. metal, plastics, ceramics and composites. Due to the dual flexure design, the extensometers work well in both tension and compression. Besides, it is rugged and insensitive to vibrations and hence allows higher frequency operation [11].



Fig. 1.4 Axial extensometer with 50 mm gauge length and $\pm 5\%$ measuring range [11]

1.4.4 Brittle Coating Method

The brittle coating method is used for strain measurement when high precision is not required. It provides direct approach for experimental stress analysis as the preparation works before the experiment is rather easy. For example, the surface of the specimen is lightly sanded before coating, followed by the application of a reflective undercoat to ease the crack observation. Finally, a thin layer of coating which exhibits brittle behaviour is sprayed evenly on the surface of the specimen. The working principle for this technique is the crack patterns as shown in Fig. 1.5 are formed when the specimen is loaded. Since the coating cracks are perpendicular to the principle tensile strain, the coating shows the direction and magnitude of the stress within the elastic limit of the specimen. Besides, the coating patterns provide a

detail picture of the distribution, location, direction, sequence and lastly the magnitude of the tensile strains by using the calibrator and the strain scale as shown in Fig. 1.6 [12].

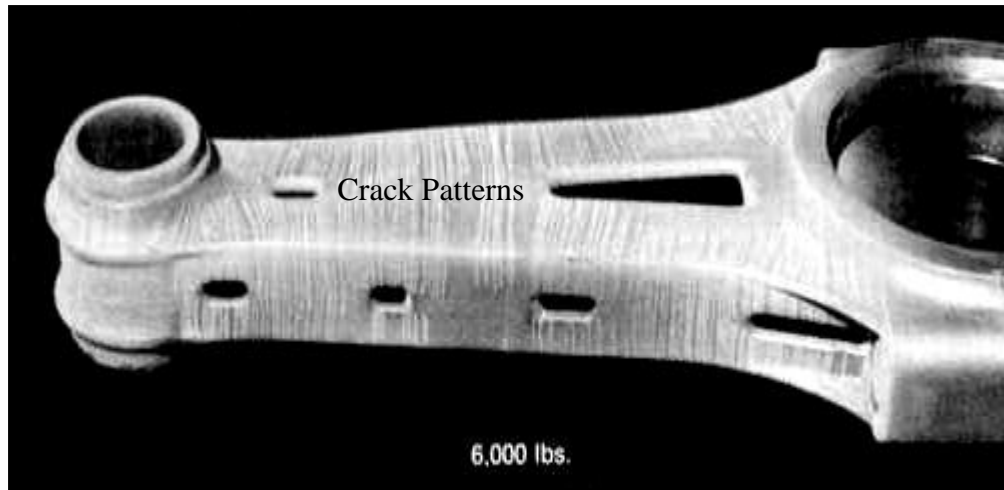


Fig. 1.5 The crack patterns on the connecting rod [12]

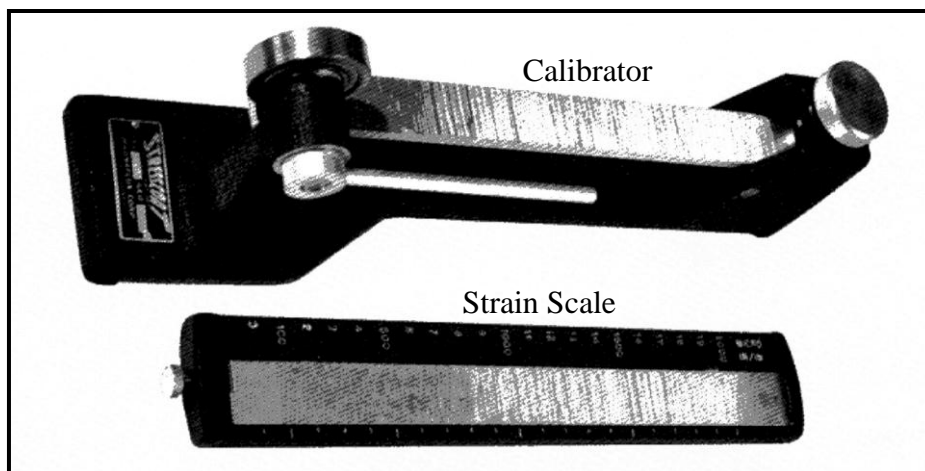


Fig. 1.6 The calibrator and the strain scale [12]

1.4.5 Photoelasticity

Photoelasticity was once the standard experimental technique for analyzing stress or strain distribution if the parts to be analyzed are made out of transparent polymers or plastics. This is because the transparent materials exhibit the property of double refraction or birefringence (two different indices of refraction in the two

perpendicular directions) when the light passes through the materials [13]. The working principle for this technique is the fringe patterns as shown in Fig. 1.7 are observed when the transparent material is placed in between the two polarizing mediums and viewed from the opposite side of the light source. The observed fringe patterns reveal the distributions and magnitudes of the stresses and strains. For example, high fringe order indicates that the material is experiencing high stress level while low fringe order indicates an unstressed area.

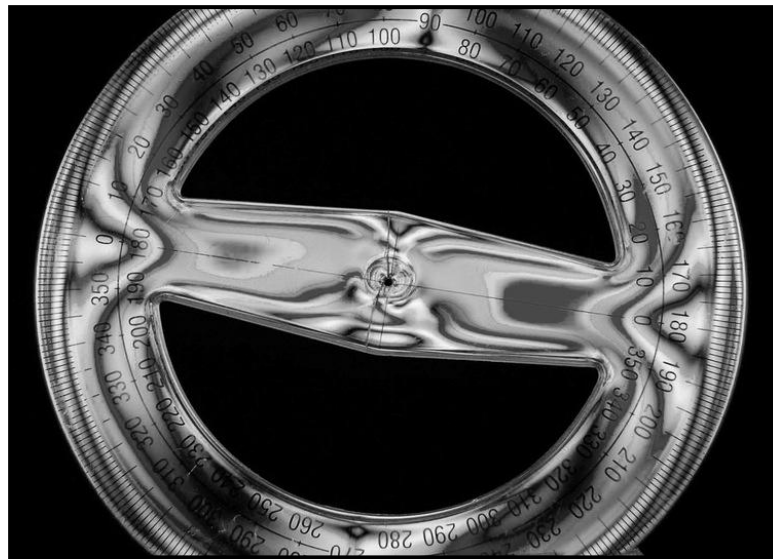


Fig. 1.7 Fringe pattern observed in photoelasticity method

1.4.6 Photoelastic-Coating Method

In general, photoelastic-coating method extends the photoelasticity technique to direct measurement of surface strains. This method is considered as an optical method since it uses the word “photo”. Meanwhile, elastic means interpretation of the experimental results by utilizing the theory of elasticity. Before the specimen is being analyzed, a thin sheet of photoelastic material is attached on the well-polished surface of the specimen with the reflective adhesive. The working principle of this method is that the surface of the specimen and the photoelastic coating will be deformed when the specimen is loaded. Hence, a strain field is developed in the coating and the fringe patterns are recorded by using reflection polariscope as shown in Fig. 1.8. Basically there are two different types of arrangement for the reflection polariscope. Fig. 1.9a shows the simple portable polariscope where the incident light

is not normal to the coating surface and so is the reflected light in the coating. The second type of arrangement shown in Fig. 1.9b is referred as beam splitter polariscope. This arrangement provides more accurate results as the incident and reflected lights are perpendicular to the coating surface [14]. Finally, the fringe patterns recorded by the reflection polariscope are analyzed and the strain values are determined.



Fig. 1.8 Reflection polariscope

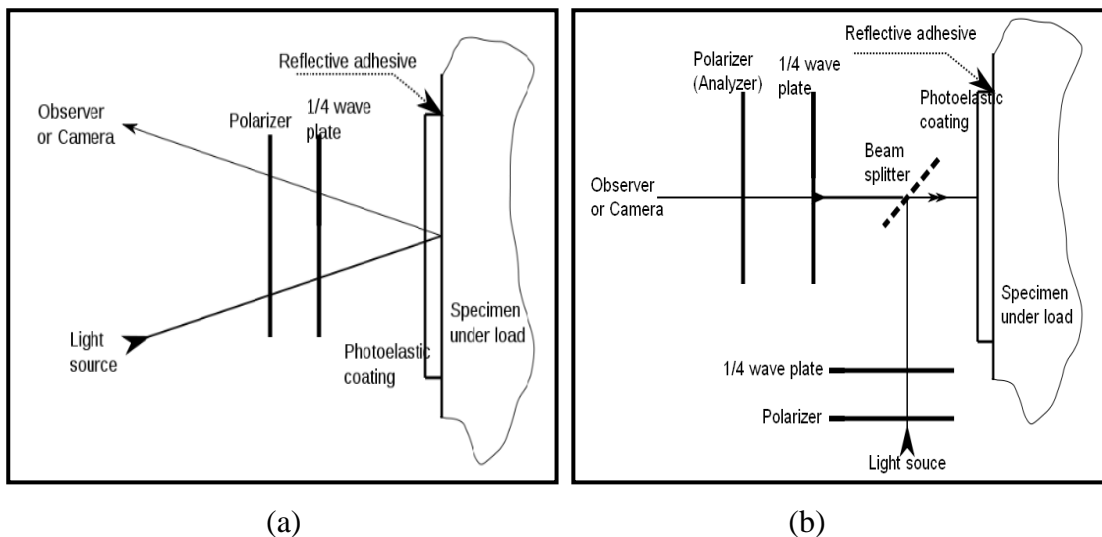


Fig. 1.9 Basic arrangements for reflection polariscope (a) Simple portable polariscope (b) Beam splitter polariscope

1.4.7 Geometric Moiré Technique

Geometric Moiré technique is another optical method used in strain analysis. The moiré interference fringes as shown in Fig. 1.10 are produced by superimposing two or more sets of gratings where the lines or dots are closely spaced. At the same time, the moiré fringes are used in strain analysis to determine the in-plane or out-of-plane displacements, rotations, curvatures and lastly the strains in x and y directions. Therefore, the gratings quality plays an important role in the strain analysis by moiré method. For example, a straight line, uniform line/space ratio and a uniform pitch is crucial to meet the requirement of this experiment. In Geometric Moiré technique, these fringes are observed through the transmitted or reflected lights. For example, a light fringe will be observed when two lines coincided together and a dark fringe will be observed when a line of one set coincided with the space of another set. In general, the grating applied in moiré technique is composed of 1 to 100 lines per mm and usually not visible to human naked eyes. However, by using the Charge-Coupled Device (CCD) or Complementary Metal-Oxide-Semiconductor (CMOS) digital camera, the fringe patterns are easily captured and the strain values are determined by using the proper magnification [15].

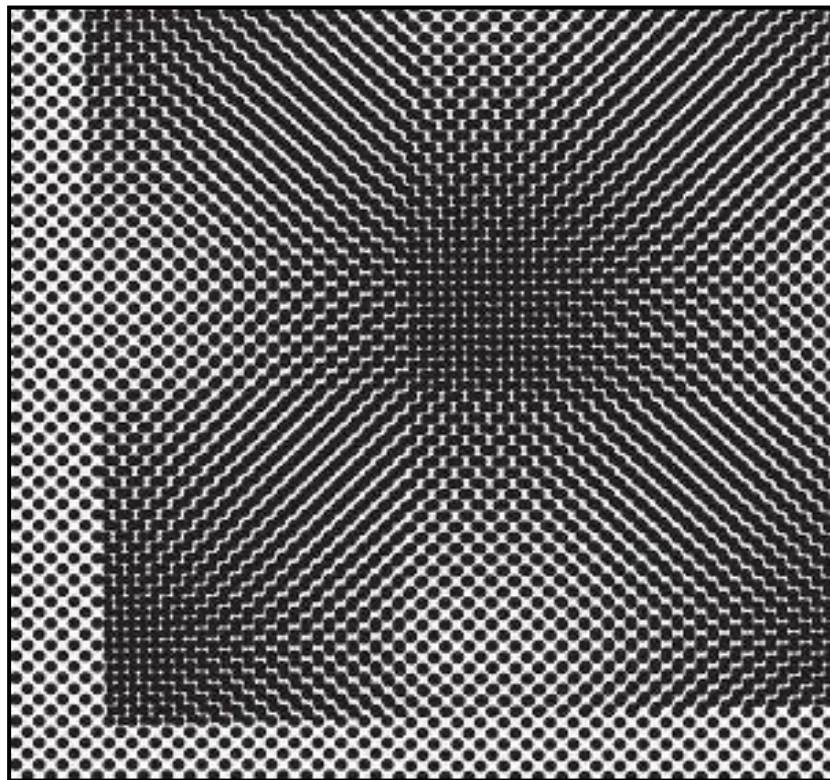


Fig. 1.10 Moiré interference fringes

1.4.8 Holographic Interferometry

Holographic interferometry has been widely used for the measurement of small in-plane and out-of-plane surface displacements in a specimen. The basic equipment for this measurement method includes a laser, recording medium, beam splitter, mirror and others as shown in Fig. 1.11. This method has many advantages over the previously discussed measurement techniques. For example, holographic interferometry provides full-field measurement, high degree of accuracy or sensitivity; it does not require any surface preparation and can be applied to any types of material surfaces [16]. The working principle of this method is that the light waves field (which includes the amplitude and the phase information) scattered from an object is recorded, followed by the reconstruction of the reflected fringe patterns. As a result, it emerges as if the object is in the same position relative to the recording medium, referred as hologram. Basically, the separate light waves are combined together by using the principle of superposition and the fringe patterns are captured by the video camera. The fringe patterns show the maps of the surface displacement and extremely sensitive towards the motion experienced by the specimen [17].

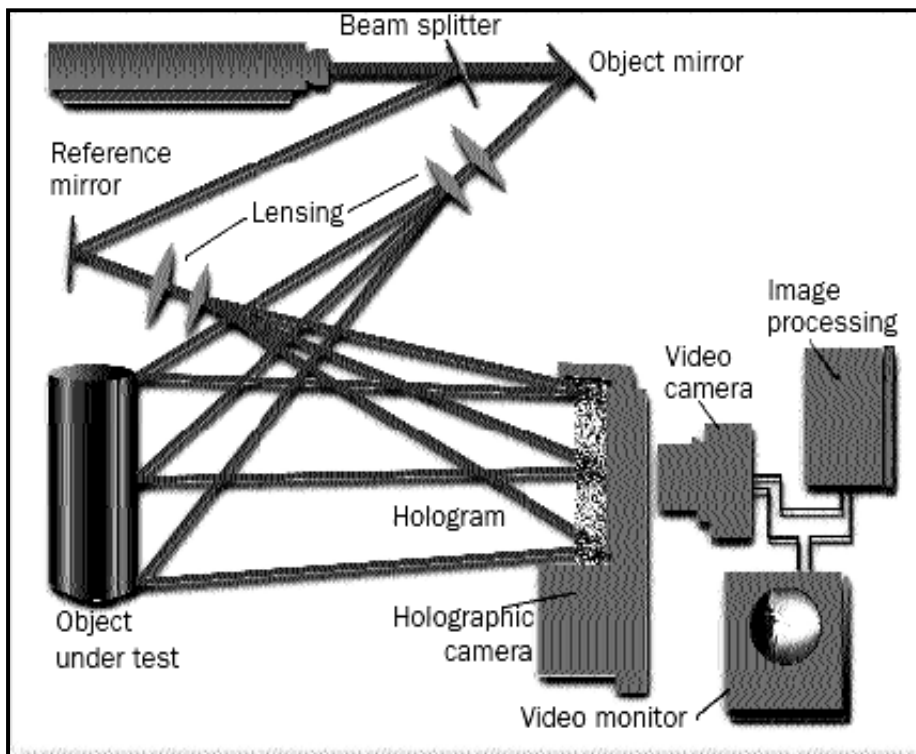


Fig. 1.11 Holographic Interferometry setup [17]

1.4.9 Digital Image Correlation

Digital image correlation (DIC) is an improved version of the optical strain measurement method. This vision metrology is ideally suitable for non-contact strain measurement in a remote system. For this system, the equipment consist of a video camera, image capture card, PC, image processing software and light source. In general, the DIC is a technique for full-field deformation measurement that mathematically compares two images that are acquired at two different states, one before deformation and the other one after deformation as shown in Fig. 1.12. The measurement of deformation of a structural component under loading can be achieved by tracking the displacement of the speckles which are deposited on the surface of sample. Therefore, the pixels resolution within the images is important in this method [18].

In 1980's, the DIC was introduced for two-dimension applications. Later, engineers extended this technique for shape and three-dimensional displacement measurement. This can be accomplished by using two cameras in a system and the images are captured from two different positions. In fact, the DIC technique has many advantages if compared with the other optical strain measurement methods. For example, the setup for DIC is easy as only a light source is needed during the experiment. Besides, fringe patterns or phase reconstruction analysis is not necessary in DIC technique as the displacement information is obtained directly by comparing the speckle position of the images that are acquired at two different states.

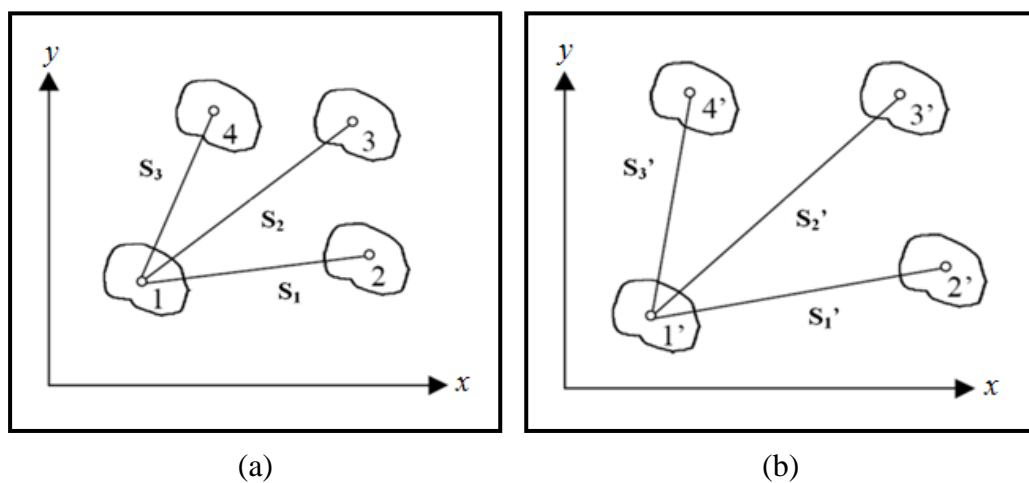


Fig. 1.12 Images at two different states (a) Before deformation
(b) After deformation

1.5 Problem Statement

Over the years, many strain measurement methods have been invented or improved in order to cope with the new challenges faced by the engineers in the field of engineering. However, each of the strain measurement methods discussed previously has its own disadvantages. For example, the scratch strain gauge is valuable in measuring the dynamic events, but it is an expensive method to determine the strain in a single location. While for the electrical resistance strain gauges, although they provide precise results in strain measurement, their high price tag and handling difficulty makes them an imperfect strain measurement method, especially the tedious bonding procedures of the strain gauges onto the specimen. By using the extensometer, the handling difficulty is solved as the extensometer is easily mounted on the specimen. In contrast, the contact points between the extensometer's arms and the specimen surface create unwanted stress concentration to the specimens. As for the brittle coating method, the preparation works before the experiment is easy, but the coating is not commonly acceptable as it exhibits both flammability and toxicity. Therefore, safety precautions against these dangers must be taken into account.

The photoelasticity method is getting less popular as the finite element analysis grows rapidly. In addition, this technique is limited to the transparent materials which exhibit the property of birefringence. Therefore, the photoelastic-coating method is introduced and the above problem is solved as a thin sheet of photoelastic material is attached on the well-polished surface of the specimen with reflective adhesive. However, this technique is facing the same problem as the electrical resistance strain gauges, where a perfect bond between the coating and the specimen is crucial. Attention must be paid to the adhesive selection and the surface preparations. The geometric moiré technique is still facing the same problem too. Moreover, this technique is not suitable for high temperature strain measurement and is not sensitive enough to measure small strains accurately. The holographic interferometry method has received substantial attention since it provides full-field deformation measurement with high degree of accuracy. At the same time, it does not require any surface preparation and can be applied to any types of material surfaces. Nevertheless, the drawback of this method is that the entire equipment must

be completely isolated from the vibrations. This is because the vibrations would alter the optical path and the recorded hologram becomes blur.

In the recent years, the Digital Image Correlation (DIC) technique is widely used for displacement measurement in experimental mechanics as it has many advantages over other optical methods. For example, it is free from the handling difficulty issue, the equipment will not create unwanted stress concentration to the specimen, the strain analysis is not limited to certain type of the materials, no tedious fringe patterns analysis or light waves field reconstruction are required in order to obtain the strain values. The theoretical simplicity is attractive but the iteration procedure for strain measurements are lengthy and always cause the errors. Besides, the video camera used to capture the images during the strain inducing event is expensive. Therefore, it is always desirable if the DIC technique can be simplified further without compromising its accuracy. In this study, a consumer version of high-definition video camera is proposed to capture the images during the tensile test with the intention of improving the robustness of this technique.

1.6 Objectives

Various strain measurement methods have been studied and reviewed. Each method mentioned previously has its own advantages and disadvantages. Thus, there is a great need to develop a precise and yet simple strain measurement method in mechanical testing. The objectives of this study are:

- i. To develop a two-dimensional measurement algorithm that calculates the strain for a loaded structural component using Digital Image Correlation technique.
- ii. To verify the accuracy of the measurement program by comparing the results with the experimental results.

1.7 Scope of Study

In this project, the scope of study is focused on the following:

- i. Development of a measurement algorithm by using the MATLAB image processing software.
- ii. Enhancement of strain measurement method using Digital Image Correlation technique compared to extensometer.
- iii. Comparison of the results obtained by the optical strain measurement method and the experimental results.

1.8 Chapter Summary

For the introduction, the definition of strain was presented. At the same time, the units and the sign conventions for the normal and the shear strain were discussed. In the second part, the concepts of strain were revealed and the roles of strain in experimental mechanics were studied. The strain measurement methods were then reviewed. The advantages and disadvantages of each method were also presented. Finally, the problem statement, objective and scope of study were established.

CHAPTER 2

LITERATURE REVIEW

2.1 Chapter Overview

In this chapter, the fundamental concepts of Digital Image Correlation (DIC) technique were discussed. Next, the development of the DIC algorithms over the years were reviewed in detail. Lastly, the accuracy analysis of the DIC technique was studied, followed by the review of the applications of the DIC in two-dimensional strain measurement.

2.2 Fundamental Concepts of Digital Image Correlation

Digital Image Correlation (DIC) is widely used for displacement measurement in experimental mechanics. More specifically, the term Digital Image Correlation refers to non-contact strain measurement method that mathematically compares two images that are acquired at two different states. The acquired images are then stored in the digital form, followed by the analysis of the images and lastly the extraction of the full-field deformation measurement values. During the image analysis, DIC or image matching has been executed by choosing two subsets (small aperture for pattern matching) from the reference (undeformed) and the deformed images for correlation. As a result, the two subsets must have the same level of light intensity or contrast, so that the image matching can be performed accurately. In general, DIC is able to correlate with many types of patterns, including grids, dots, lines and random patterns [19]. On the other hand, a few limitations such as the aperture and the correspondence problem within the DIC need to be resolved before this technique can be adopted.

Due to the aperture problem, it is nearly impossible to find the correspondence of a single pixel information in a reference image in a deformed image. For example, the gray value of a single pixel in the reference image can be easily matched with other pixels in the deformed image, but there is still no unique correspondence. Therefore, the researchers suggested to find the correspondence of a small neighbourhood around the pixel of interest. This technique is able to provide additional information, but the matching problem has not been solved. Fig. 2.1 shows the aperture problem for a line in an image. For example, the motion within the line cannot be resolved although the component of the motion vector is perpendicular to the line. This is because a point located on the line in the reference image can be matched with an arbitrary point on the line in the deformed image as shown in Fig. 2.1a. However, the aperture problem can be resolved and the motion vector becomes unique correspondence when the aperture has been enlarged to include the end points of the line as shown in Fig. 2.1b [18].

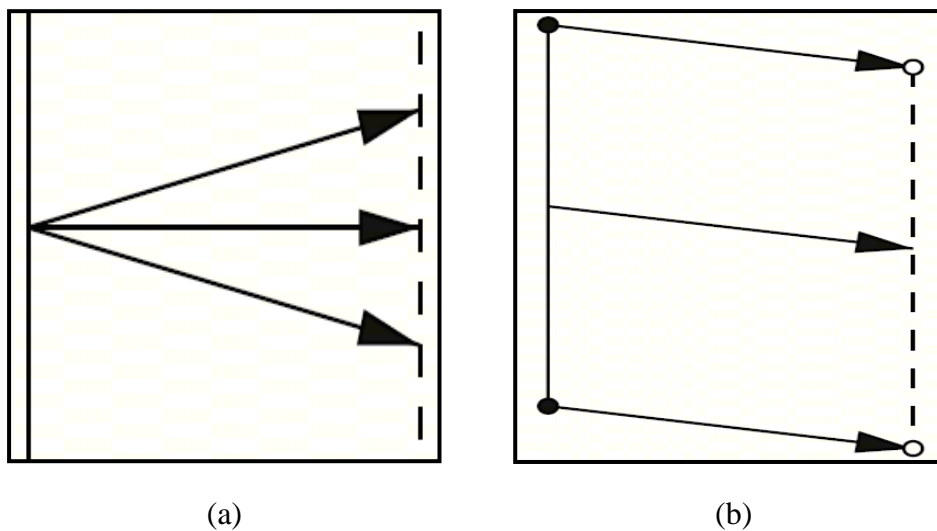


Fig. 2.1 The aperture problem for a line in an image (a) The point located on the line in the reference image can be matched with an arbitrary point on the line in the second image (b) The motion vector becomes unique correspondence when the aperture has been enlarged to include the end points

Although the aperture problem has been solved, there are many circumstances where the unique correspondence between two images is difficult to establish. For example, the repeating structure such as a grid of small dots or no texture surfaces,

no motion information can be obtained within its boundaries as no features are presented. Besides, this correspondence problem becomes more difficult to be determined as the DIC technique do not restrict the image analysis to rigid motion, but treat cases where the structure undergoing deformation. In order to overcome the correspondence problem, the structure surface has to demonstrate certain properties as the oriented textures such as lines and a grid of small dots limit the determination of motion vectors. The ideal surface texture must exhibit the isotropic behavior and do not have a preferred orientation since the repeating textures will lead to the misregistration problems. Therefore, this condition required the use of random textures such as the speckle pattern. Basically, the speckle pattern used in DIC is adhered to the surface and therefore deformed along with the surface. There are several advantages for the usage of random speckle pattern in DIC. For example, the correlations during the image analysis will not be lost even though the object is under large deformations and the speckle pattern itself contains much information. This information is available everywhere on the surface as the random speckle pattern is located on the entire surface. Therefore, random speckle pattern permits the use of a subset during the correlation process [18].

By using the random speckle pattern, the aperture and the correspondence problems mentioned above are solved effortlessly. However, another problem called as the null measurement limitation has been occurred as the consequence of using the random speckle pattern in a DIC system. Basically, the null measurement is a diagnostic test to quantify the accuracy of a DIC system and a perfect DIC system is expected to provide a null result. The working principle of this test is that the measured value from the DIC system is compared to the benchmark value, so that the difference between the two values is observed and further adjusted until zero. Although the knowledge of null measurement is crucial in improving the accuracy of the DIC system, but the diagnostic test is extremely difficult to be designed especially when the test objects have the nonconic aspheric surfaces. In order to cope with this challenge, a null lens or a computer-generated hologram (CGH) is designed by the engineers or the researchers. Nonetheless, the null lens or the CGH need to be tested before they can be used in the diagnostic test and this indirectly leads to another quality assurance issue in the null measurement. Over the years, the national

standards are still unable to set the standard guidelines for the null measurement. Therefore the null lens or the CGH served as the two techniques that are used to quantify the accuracy of the DIC system [20].

During the image matching process, DIC algorithm is applied to match the intensity pattern between the undeformed and the deformed images. For example, a few points within the reference image are selected for the calculation of displacement field. For each point, a subset is selected and correlated to the corresponding subset in the deformed image. This concept has successfully been executed as the neighboring points in the undeformed image are assumed to remain as neighboring points even after the deformation took place. In DIC, there is no guideline or rule in determining the size of the subset and therefore is a very subjective matter. A large subset will require much computation time and provides an average result on the resultant displacement field. However, for a small subset, it contains inadequate features and the correlation process becomes difficult to be distinguished from the other subsets. As a consequence, the correlation may not provide a reliable result [21].

In the early stage, the coarse-fine searching method was the commonly used DIC algorithm. This algorithm search for the best match of the two subsets or correlates the subsets in the reference image with a series of subsets in the deformed image. After that, interpolation method was applied to reconstruct the intensity distribution and fine searching was performed to identify the correlation peak with the accuracy of subpixel level. Lastly, the DIC algorithm was used to calculate the displacement parameters and the deformation fields in the samples were then determined. In the last two decades, these algorithms were improved and modified in order to increase its accuracy and shorten the determination time. The details about the development of the DIC algorithms are discussed in the next section.

2.3 Development of the Digital Image Correlation Algorithms

The Digital Image Correlation (DIC) was first introduced by Peters and Ranson [22] in 1980's for experimental stress analysis. They proposed the digital imaging technique for measuring the surface displacement of the speckle patterns in a reference and deformed images. From the images, subsets from the deformed images were numerically correlated with the reference image and the surface displacement was calculated. Lastly, stresses within the structure were determined. In 1983, Sutton *et al.* [23] improved the DIC technique to obtain the full-field in-plane deformations of a cantilever beam. Fig. 2.2 shows the schematic diagram of the experimental set-up for DIC system. In the experiment, a specimen with random speckle pattern on the surface was placed perpendicular to the optical axis of the video camera. During the strain inducing event, an image was captured at its undeformed state; followed by continuous capturing of the deformed images. From these images, they suggested that the intensity distribution of light reflected by the specimen can be stored as a set of grey levels in a computer where the values were ranged from 0 to 255 (0 represents zero light intensity and 255 represents maximum light intensity). Fig. 2.3 shows the graphical portrayal of digital intensities for a 10×10 subset. Since the sensors recorded the continuously varying intensity pattern in a discrete form, a surface fit method known as the bilinear interpolation was applied in order to represent the data in a continuous form as shown in Fig. 2.3b.

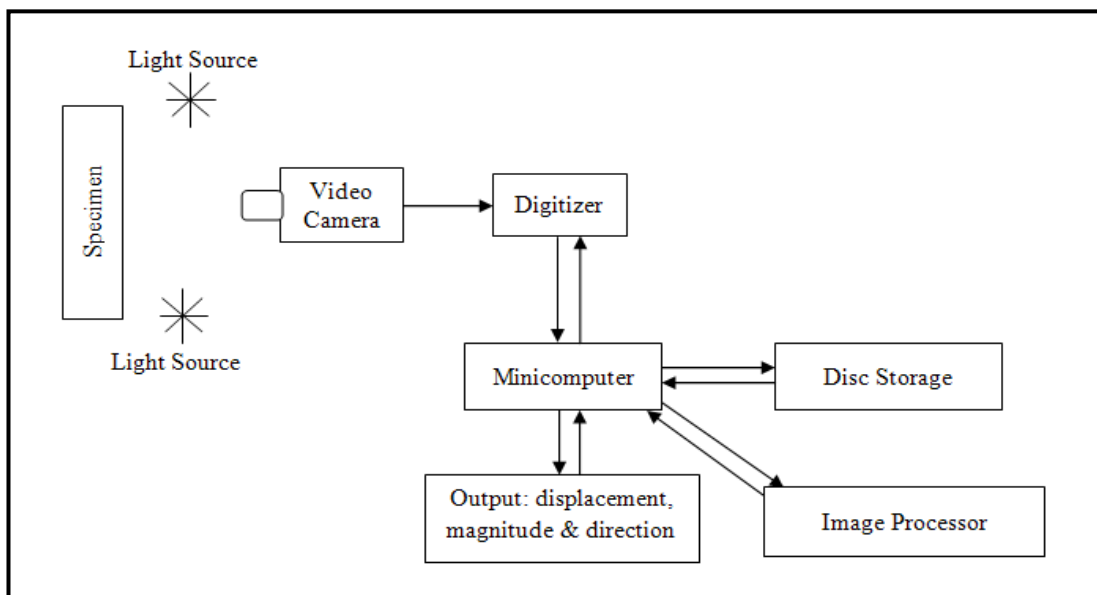
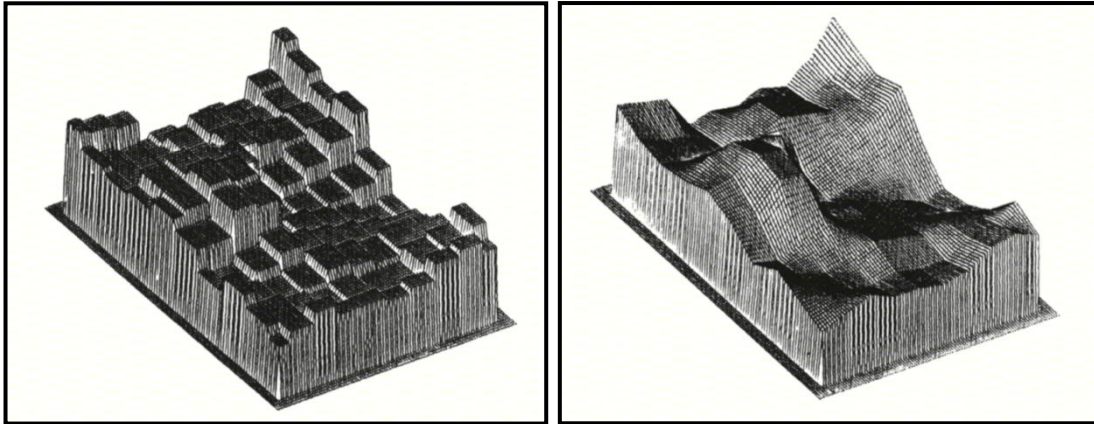


Fig. 2.2 Schematic diagram of the experimental set-up for DIC system



(a)

(b)

Fig. 2.3 Digital intensities for a 10×10 subset (a) Intensity distribution in a discrete form (b) Intensity distribution in a continuous form

In 1985, Chu *et al.* [24] explained the basic theory and the assumptions used in the correlation method. They assigned the intensity patterns corresponding to the reflected light from the undeformed and deformed specimens as $f(x, y)$ and $f^*(x^*, y^*)$ respectively. The intensity patterns were assumed to be unique and one-to-one correspondence. Besides, a schematic diagram was used to describe the deformation process of a planar object as shown in Fig. 2.4. The quadrangle S represents the subimage in the reference state and the quadrangle S^* represents the subimage in the deformed state. Based on the schematic diagram, they performed a series of iteration

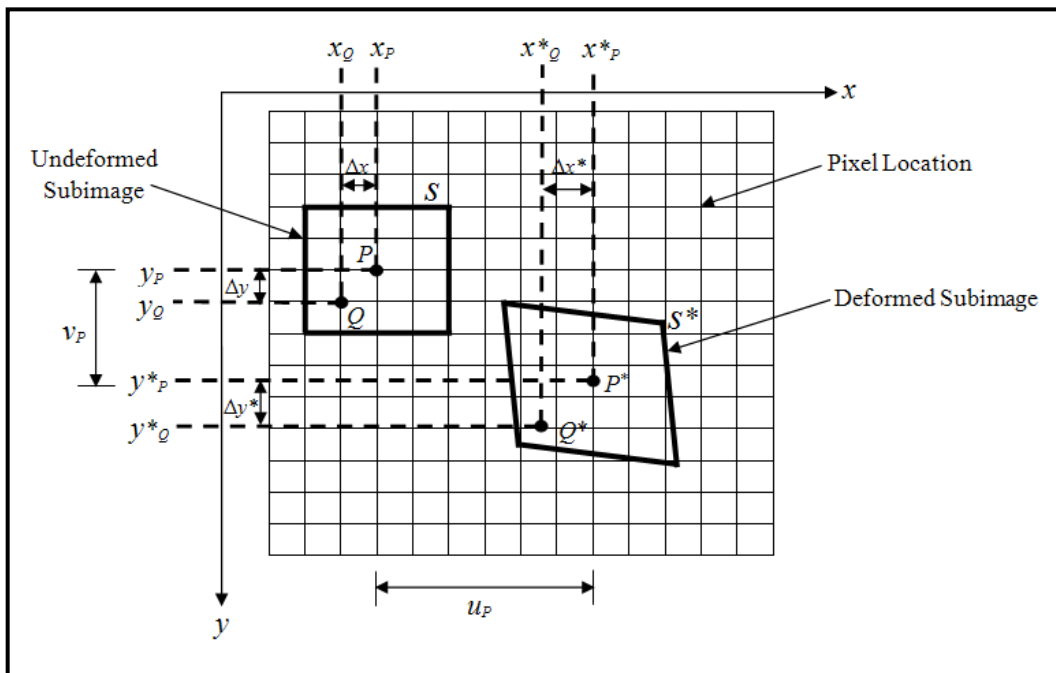


Fig. 2.4 Schematic diagram of a planar object undergoing deformation process

procedure in order to determine the in-plane displacement of u_p and v_p . To start the analysis, P was selected from the undeformed object subset and the range of the displacement values of u and v were estimated while the remaining variables were set to zero. Within the undeformed subset, the intensity values $f(x, y)$ at selected points were compared to the intensity values $f^*(x^*, y^*)$ of the deformed subset. The assumption was validated if the subset only translated without distortion such as the positions of $x^* = x + u$ and $y^* = y + v$ were followed. Finally, they applied the cross-correlation coefficient, C to compare the two subsets and the equation is expressed as

$$C(u, v, \frac{\partial u}{\partial x}, \frac{\partial u}{\partial y}, \frac{\partial v}{\partial x}, \frac{\partial v}{\partial y}) = \frac{\int_{S^*} f(x, y) \cdot f^*(x + \xi, y + \eta) dA}{\sqrt{\int_S [f(x, y)]^2 dA \cdot \int_{S^*} [f^*(x + \xi, y + \eta)]^2 dA}} \quad (2.1)$$

where S is the subimage in the undeformed image, S^* is the subimage in the deformed image, u and v are the displacements in x and y directions, $\frac{\partial u}{\partial x}$, $\frac{\partial u}{\partial y}$, $\frac{\partial v}{\partial x}$, $\frac{\partial v}{\partial y}$ are the displacement derivatives of point P , $f(x, y)$ is the intensity values of the undeformed subset, $f^*(x + \xi, y + \eta)$ is the intensity values of the deformed subset and dA is the derivative of the area of scanning. The total displacements of ξ and η in the x and y directions are given by

$$\xi = u + \frac{\partial u}{\partial x} \Delta x + \frac{\partial u}{\partial y} \Delta y \quad (2.2)$$

$$\eta = v + \frac{\partial v}{\partial x} \Delta x + \frac{\partial v}{\partial y} \Delta y \quad (2.3)$$

where Δx and Δy are the distance between point P and point Q in x and y directions respectively in subset S . The values of u , v , $\frac{\partial u}{\partial x}$, $\frac{\partial u}{\partial y}$, $\frac{\partial v}{\partial x}$ and $\frac{\partial v}{\partial y}$ were the local deformation values for the subset if the cross-correlation coefficient was maximized.

Sutton *et al.* [25] modified the iterative Digital Image Correlation algorithm used earlier in 1986. The modified method has reduced the strain determination time and still managed to achieve the accuracy equivalent to the previously used coarse-fine iterative techniques. In their work, they applied the Newton-Raphson method with

differential corrections to speed up the searching time. In 1989, Bruck *et al.* [26] optimized the DIC algorithms which converged faster and hence fewer calculations were needed. Based on Fig. 2.4, they suggested that if the subset S is small, the coordinates of point P , x_p^* and y_p^* in the subset S^* are expressed as

$$x_p^* = x_p + u_p + \frac{\partial u}{\partial x} / p \cdot \Delta x + \frac{\partial u}{\partial y} / p \cdot \Delta y \quad (2.4)$$

$$y_p^* = y_p + v_p + \frac{\partial v}{\partial x} / p \cdot \Delta x + \frac{\partial v}{\partial y} / p \cdot \Delta y \quad (2.5)$$

where x_p and y_p are the coordinates of the point P in subset S , u_p and v_p are the displacements of point P in x and y directions, $\frac{\partial u}{\partial x} / p$, $\frac{\partial u}{\partial y} / p$, $\frac{\partial v}{\partial x} / p$ and $\frac{\partial v}{\partial y} / p$ are the displacement derivatives of point P , Δx and Δy are the distance between point P and point Q in x and y directions respectively in subset S . Besides, they assigned the intensity values at point P as $f(x_p, y_p)$ and $f^*(x_p^*, y_p^*)$ for the reference and the deformed image respectively. Hence, the correlation coefficient C is expressed as

$$C = \frac{\sum_{P \in S} [f(x_p, y_p) - f^*(x_p^*, y_p^*)]^2}{\sum_{P \in S} f(x_p, y_p)^2} \quad (2.6)$$

or

$$C = 1 - \frac{\sum_{P \in S} f(x_p, y_p) \cdot f^*(x_p^*, y_p^*)}{\sqrt{\sum_{P \in S} f(x_p, y_p)^2 \cdot \sum_{P \in S} f^*(x_p^*, y_p^*)^2}} \quad (2.7)$$

From the above equation, the correlation coefficient C would be zero if the parameters u_p and v_p are the real displacements of point P in x and y directions and $\frac{\partial u}{\partial x} / p$, $\frac{\partial u}{\partial y} / p$, $\frac{\partial v}{\partial x} / p$ and $\frac{\partial v}{\partial y} / p$ are the displacement derivatives of point P . Therefore, the best estimation for these values was determined by minimizing the correlation coefficient C . In their work, they developed the complete model of Newton-Raphson method of partial differential corrections which determines the six parameters by using less computation time if compared to the previously used coarse-fine search method. This method was based on the calculation of the correction terms and the

initial estimations were improved significantly. The correction for guess is expressed as

$$\Delta P_i = -H^I(P_i) * \nabla(P_i) \quad (2.8)$$

where ΔP_i is the initial guess for the six deformation parameters, $H(P_i)$ is the Hessian matrix which contains the second derivatives of the correlation function and $\nabla(P_i)$ is the Jacobian matrix which contains the derivative of the correlation function. The initial guess for the six deformation parameters is given by

$$\Delta P_i = \begin{Bmatrix} u \\ v \\ \frac{\partial u}{\partial x} \\ \frac{\partial u}{\partial y} \\ \frac{\partial v}{\partial x} \\ \frac{\partial v}{\partial y} \end{Bmatrix} \quad (2.9)$$

where $u, v, \frac{\partial u}{\partial x}, \frac{\partial u}{\partial y}, \frac{\partial v}{\partial x}, \frac{\partial v}{\partial y}$ are the six deformation parameters. The Hessian matrix,

$H(P_i)$, containing the second derivatives of the correlation function is given by

$$H(P_i) = \begin{Bmatrix} \frac{\partial^2 C}{\partial u \partial u} & \frac{\partial^2 C}{\partial u \partial v} & \frac{\partial^2 C}{\partial u \partial (\frac{\partial u}{\partial x})} & \frac{\partial^2 C}{\partial u \partial (\frac{\partial u}{\partial y})} & \frac{\partial^2 C}{\partial u \partial (\frac{\partial v}{\partial x})} & \frac{\partial^2 C}{\partial u \partial (\frac{\partial v}{\partial y})} \\ \frac{\partial^2 C}{\partial v \partial u} & \frac{\partial^2 C}{\partial v \partial v} & \frac{\partial^2 C}{\partial v \partial (\frac{\partial u}{\partial x})} & \frac{\partial^2 C}{\partial v \partial (\frac{\partial u}{\partial y})} & \frac{\partial^2 C}{\partial v \partial (\frac{\partial v}{\partial x})} & \frac{\partial^2 C}{\partial v \partial (\frac{\partial v}{\partial y})} \\ \frac{\partial^2 C}{\partial (\frac{\partial u}{\partial x}) \partial u} & \frac{\partial^2 C}{\partial (\frac{\partial u}{\partial x}) \partial v} & \frac{\partial^2 C}{\partial (\frac{\partial u}{\partial x}) \partial (\frac{\partial u}{\partial x})} & \frac{\partial^2 C}{\partial (\frac{\partial u}{\partial x}) \partial (\frac{\partial v}{\partial y})} & \frac{\partial^2 C}{\partial (\frac{\partial u}{\partial x}) \partial (\frac{\partial v}{\partial x})} & \frac{\partial^2 C}{\partial (\frac{\partial u}{\partial x}) \partial (\frac{\partial v}{\partial y})} \\ \frac{\partial^2 C}{\partial (\frac{\partial v}{\partial x}) \partial u} & \frac{\partial^2 C}{\partial (\frac{\partial v}{\partial x}) \partial v} & \frac{\partial^2 C}{\partial (\frac{\partial v}{\partial x}) \partial (\frac{\partial u}{\partial x})} & \frac{\partial^2 C}{\partial (\frac{\partial v}{\partial x}) \partial (\frac{\partial v}{\partial y})} & \frac{\partial^2 C}{\partial (\frac{\partial v}{\partial x}) \partial (\frac{\partial v}{\partial x})} & \frac{\partial^2 C}{\partial (\frac{\partial v}{\partial x}) \partial (\frac{\partial v}{\partial y})} \\ \frac{\partial^2 C}{\partial (\frac{\partial u}{\partial y}) \partial u} & \frac{\partial^2 C}{\partial (\frac{\partial u}{\partial y}) \partial v} & \frac{\partial^2 C}{\partial (\frac{\partial u}{\partial y}) \partial (\frac{\partial u}{\partial x})} & \frac{\partial^2 C}{\partial (\frac{\partial u}{\partial y}) \partial (\frac{\partial v}{\partial y})} & \frac{\partial^2 C}{\partial (\frac{\partial u}{\partial y}) \partial (\frac{\partial v}{\partial x})} & \frac{\partial^2 C}{\partial (\frac{\partial u}{\partial y}) \partial (\frac{\partial v}{\partial y})} \\ \frac{\partial^2 C}{\partial (\frac{\partial v}{\partial y}) \partial u} & \frac{\partial^2 C}{\partial (\frac{\partial v}{\partial y}) \partial v} & \frac{\partial^2 C}{\partial (\frac{\partial v}{\partial y}) \partial (\frac{\partial u}{\partial x})} & \frac{\partial^2 C}{\partial (\frac{\partial v}{\partial y}) \partial (\frac{\partial v}{\partial y})} & \frac{\partial^2 C}{\partial (\frac{\partial v}{\partial y}) \partial (\frac{\partial v}{\partial x})} & \frac{\partial^2 C}{\partial (\frac{\partial v}{\partial y}) \partial (\frac{\partial v}{\partial y})} \end{Bmatrix} \quad (2.10)$$

The Jacobian Matrix, $\nabla (P_i)$ containing the derivative of the correlation function is given by

$$\nabla (P_i) = \left\{ \begin{array}{l} \frac{\partial C}{\partial u} \\ \frac{\partial C}{\partial v} \\ \frac{\partial C}{\partial \left(\frac{\partial u}{\partial x}\right)} \\ \frac{\partial C}{\partial \left(\frac{\partial u}{\partial y}\right)} \\ \frac{\partial C}{\partial \left(\frac{\partial v}{\partial x}\right)} \\ \frac{\partial C}{\partial \left(\frac{\partial v}{\partial y}\right)} \end{array} \right\} \quad (2.11)$$

By using the Newton-Raphson method, the initial estimation for the six deformation parameters, $u, v, \frac{\partial u}{\partial x}, \frac{\partial u}{\partial y}, \frac{\partial v}{\partial x}, \frac{\partial v}{\partial y}$ were first determined and the partial corrections were then calculated by using eq. (2.8). Finally, the corrections were added to the initial estimation values and the iteration process was terminated once convergence was obtained. In 1998, Vendroux and Knauss [27] proposed an alternative approach in determining the two-dimensional surface displacement. In their work, Scanning Tunnelling Microscopy (STM) was used to scan the surface topographies and the out-of-plane displacement was extracted from the in-plane components. An out-of-plane displacement, W_o was introduced into the correlation coefficient and it was minimized together with the others six in-plane deformation parameters. The modified approach was named as a least squares correlation coefficient and is expressed as

$$C = \frac{\sum_{P \in S} \{ f(x_p, y_p) - [f^*(x^*_p, y^*_p) - W_o] \}^2}{\sum_{P \in S} f(x_p, y_p)^2} \quad (2.12)$$

where W_o is the out-of-plane component. They applied a least squares correlation coefficient together with the Hessian matrix. This simplified the Newton-Raphson scheme and 25% of improvement was achieved in speed, as well as the convergence robustness of the algorithm code.

Lu and Cary [28] applied a second-order approximation to determine the first and second order displacement gradient. They also implemented a third-order polynomial interpolation known as bicubic spline to reconstruct the gray values at any location within the images. This was carried out as the previous DIC algorithms only assumed a first order approximation in determining the deformation parameters. In their work, the second-order Taylor series approximation of the displacement field was adopted and the assumption for the coordinates of point P , x_p^* and y_p^* in the subset S^* are expressed as

$$x_p^* = x_p + u_p + u_x \Delta x + u_y \Delta y + \frac{1}{2} u_{xx} \Delta x^2 + \frac{1}{2} u_{yy} \Delta y^2 + u_{xy} \Delta x \Delta y \quad (2.13)$$

$$y_p^* = y_p + v_p + v_x \Delta x + v_y \Delta y + \frac{1}{2} v_{xx} \Delta x^2 + \frac{1}{2} v_{yy} \Delta y^2 + v_{xy} \Delta x \Delta y \quad (2.14)$$

where x_p and y_p are the coordinates of the point P in subset S , u_p and v_p are the displacements of point P in x and y directions, u_x , v_x , u_y and v_y are the first order displacement gradients, u_{xx} , v_{xx} , u_{yy} , v_{yy} , u_{xy} and v_{xy} are the second order displacement gradients, Δx and Δy are the distance between point P and point Q in x and y directions respectively in subset S . By using the 12 parameters, the deformation range was increased and the large deformation measurement was accurately obtained. In addition, Cheng *et al.* [29] applied further the Bicubic Spline (B-Spline) deformation function to represent the two-dimensional continuous intensity fields throughout the entire image area. By doing this, the arbitrary decision of the subset size was eliminated and the results showed that the B-Spline deformation function had increased the accuracy, as well as the computational efficiency for the deformation measurement.

In 2003, Hung *et al.* [30] presented a simple search algorithm known as Fast and Simple (FAS) for the measurement of the surface deformation in two-dimension. This algorithm was developed as the Newton-Raphson method with partial differential corrections suffered from the lengthy computation time. Although the algorithm reduced the strain determination time, the accuracy was decreased if compared to the Newton-Raphson method. In 2007, Meng *et al.* [31] improved the accuracy of the displacement field results by introducing an iteration spatial gradient,

finite element smoothing and two-dimensional Generalized Cross-Validation (GCV) algorithm. The algorithm was implemented for smoothing the full-field displacement results that were determined by Newton-Raphson iteration scheme. They claimed that this process was necessary because of the strain data obtained were not perfectly representing the actual strain values as the high level of noise occurred within the reference and the deformed images. Recently, Cofaru *et al.* [32] improved further the Newton-Raphson iteration scheme by introducing an adaptive spatial regularization in the minimization process of correlation coefficient. In their algorithm, the neighbouring motions information were utilized and processed. As a result, only relevant data or coordinates were selected for correlation and this increased the motion and strain accuracy.

However in 1989, Hovis [33] developed an algorithm known as Centroidal Tracking algorithm which performed the two-dimensional full-field deformation measurements by tracking the displacement of the speckles' centroid. By using this method, the interpolation procedures in smoothing the intensity values of the subset in the reference and the deformed images were avoided. Besides, the initial estimations of the displacement values, u , v and the correlation coefficient were no longer be necessary as the coordinates of the speckles in the deformed images were determined using the centroidal tracking algorithm. Before the analyzing process was carried out, image processing such as filtering and edge enhancement were performed to enhance the surface features as shown in Fig. 2.5.

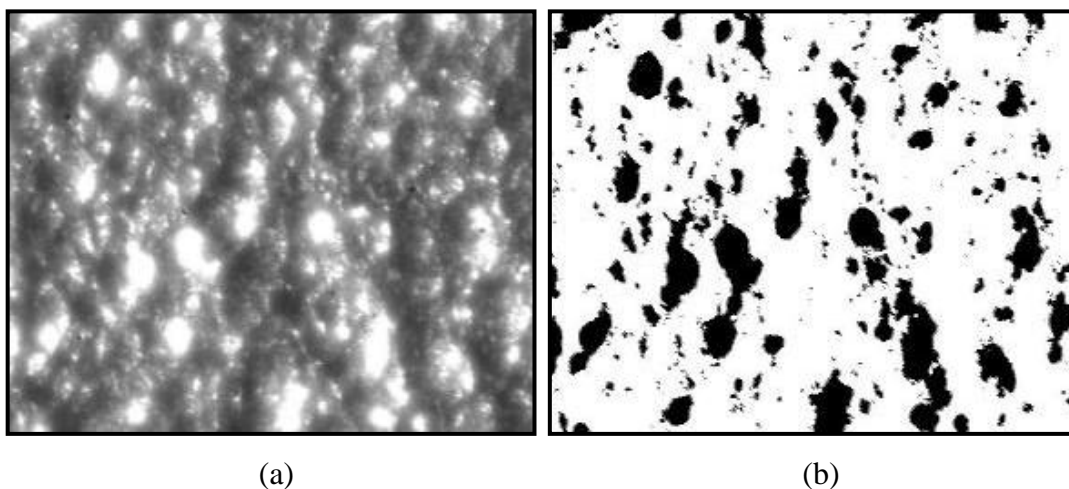


Fig. 2.5 Gray Scale images (a) Before surface enhancement
(b) After surface enhancement

Based on Fig. 2.5b, the position of the speckles' centroid were determined and the centroid coordinates, X_c and Y_c were computed using the equation expressed as

$$X_c = \frac{\Sigma [x_i \Delta a_i]}{A} \quad (2.15)$$

$$Y_c = \frac{\Sigma [y_i \Delta a_i]}{A} \quad (2.16)$$

$$A = \Sigma [\Delta a_i] \quad (2.17)$$

where x_i and y_i are the pixel coordinates of the speckles, Δa_i is the pixel area where the value is equal to 1, A is the sum of the number of pixels in the total area. After obtaining the centroid coordinates, the change of the interested speckles in the distance between the two subsequent images was determined as shown in Fig. 2.6.

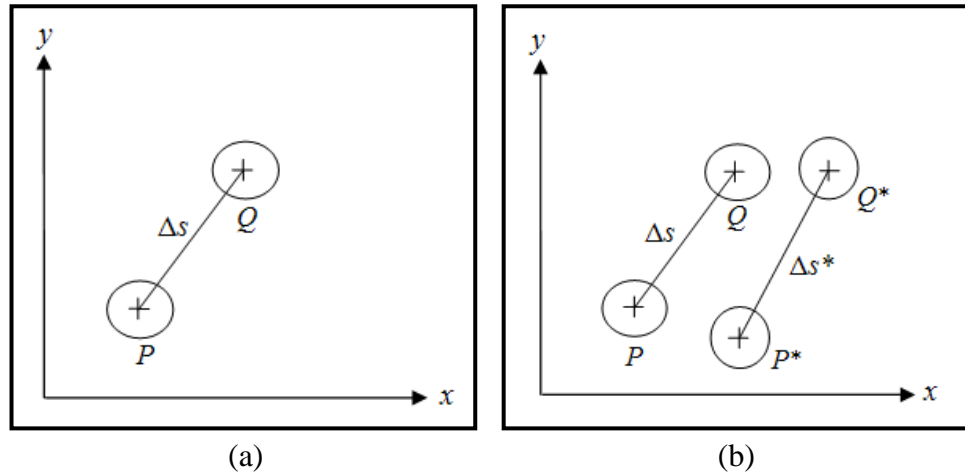


Fig. 2.6 The speckles coordinates in an image (a) Before deformation
(b) Before and after deformation

As shown in Fig. 2.6, point P and Q were displaced to point P^* and Q^* after the strain inducing event took place. As a result, the relative change in distance, ϵ_{PQ} between point P and Q was determined by

$$\epsilon_{PQ} = \frac{\Delta s^* - \Delta s}{\Delta s} \quad (2.18)$$

where Δs is the length of PQ and Δs^* is the length of P^*Q^* . Hovis suggested that the relative elongation at the point P in the direction of Q , ϵ_{PQ} can be expanded in terms

of the strain components ε_{ij} and the strain components were then determined using the Geometric Approach equation [34] as shown below

$$\begin{aligned} \frac{1}{2} \varepsilon_{PQ}^2 + \varepsilon_{PQ} = & \varepsilon_{xx} \cos^2 \theta_x + \varepsilon_{yy} \cos^2 \theta_y + \varepsilon_{zz} \cos^2 \theta_z + 2\varepsilon_{xy} \cos \theta_x \cos \theta_y \\ & + 2\varepsilon_{xz} \cos \theta_x \cos \theta_z + 2\varepsilon_{yz} \cos \theta_y \cos \theta_z \end{aligned} \quad (2.19)$$

where ε_{xx} , ε_{yy} and ε_{zz} are the normal strain in x , y and z -axis respectively, ε_{xy} , ε_{xz} and ε_{yz} are the shear strain in xy , xz and yz -plane respectively, θ_x , θ_y and θ_z are the orientations of the line element PQ in the reference or undeformed image as shown in Fig. 2.7.

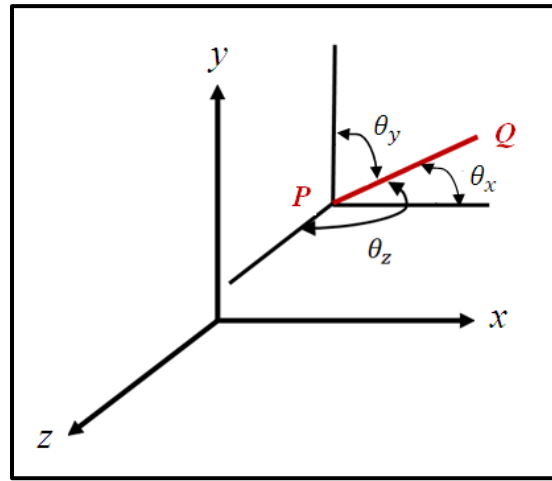


Fig. 2.7 The orientations of the line element PQ in the reference image

The orientations of the line element PQ in the reference image were calculated using the equations given by

$$\cos \theta_x = \frac{\Delta x}{\Delta s} \quad (2.20)$$

$$\cos \theta_y = \frac{\Delta y}{\Delta s} \quad (2.21)$$

$$\cos \theta_z = \frac{\Delta z}{\Delta s} \quad (2.22)$$

where Δx , Δy and Δz are the distance between point P and point Q in x , y and z directions respectively in the reference image, Δs is the length of PQ . However for

the surface measurements, the Geometric Approach equation is reduced to two-dimension and the Geometric Approach equation is expressed in the form

$$\frac{1}{2} \varepsilon_{PQ}^2 + \varepsilon_{PQ} = \varepsilon_{xx} \cos^2 \theta_x + \varepsilon_{yy} \cos^2 \theta_y + 2\varepsilon_{xy} \cos \theta_x \cos \theta_y \quad (2.23)$$

Based on eq. 2.23, a minimum of four points were selected within the reference and the deformed image respectively in order to calculate the strain components, ε_{xx} , ε_{yy} and ε_{xy} . It was reported in their finding that the accuracy of the results was increased by selecting more than four points. This Geometric Approach is so attractive since the equation used is rather simple and yet precise enough when compared to the other methods proposed by the previous researchers. In 1999, Hovis and Ranson *et al.* [35] adopted the simplicity of the Geometric Approach concept and developed a compact instrument for strain measurement in a variety of environment. The instrument consisted of a video camera, image capture card, computer, image processing software and a light source. In their work, Microsoft Visual C++ software was used to load pairs of images manually and the strain results were determined successfully. In contrast, the presented algorithm was limited by manual method of measuring the two points and there was a great need to develop an automated measurement algorithm.

Besides using the correlation method and the Geometric Approach, Chen *et al.* [36] suggested that the whole field u and v displacements of the specimen can be determined by Fast-Fourier transform (FFT). They claimed that the reference and the deformed images were simply analyzed by two-step FFT. First, two complex spectra of both subimages were determined and the new resultant spectrum was constructed according to the phase difference and amplitude. After this, the second step FFT was applied to create an outstanding signal peak and the local displacement vector was determined. D. Amodio *et al.* [37] presented the FFT technique that was used to increase the speed of image processing. In order to achieve high accuracy, they suggested that more than 100 images have to be acquired within the 1% of strain. As a result, there was a need to shorten the processing time. They claimed that the algorithm was able to process hundreds of images within a reasonable time and hence increased the subset analyzing size. Table 2.1 summarizes the development and the improvement of the DIC algorithms over the years.

Table 2.1 The development and the improvement of the DIC algorithms

Researchers	Year	Remarks for the DIC Algorithms
Peters and Ranson	1982	<ul style="list-style-type: none"> • Introduced the DIC for experimental stress analysis • Applied DIC to determine the stresses within a structure
Sutton <i>et al.</i>	1983	<ul style="list-style-type: none"> • Improved the DIC method to obtain the full-field in-plane deformations of a cantilever beam • Introduced surface fit method to smooth intensity value • Suggested the application of correlation coefficient
Chu <i>et al.</i>	1985	<ul style="list-style-type: none"> • Introduced the cross-correlation coefficient
Sutton <i>et al.</i>	1986	<ul style="list-style-type: none"> • Applied Newton-Raphson method with differential corrections to speed up the searching time
Bruck <i>et al.</i>	1989	<ul style="list-style-type: none"> • Optimized the correlation coefficient which converges faster and fewer calculations were needed • Developed a complete model of Newton-Raphson method of partial differential corrections
Hovis	1989	<ul style="list-style-type: none"> • Developed a Centroidal Tracking algorithm which performed the 2D full-field deformation measurements by tracking the displacement of the speckles' centroid • Suggested that the strain components can be determined by Geometric Approach equation
Chen <i>et al.</i>	1993	<ul style="list-style-type: none"> • Suggested the Fast-Fourier Transform to determine the whole field deformation displacement
Vendroux and Knauss	1998	<ul style="list-style-type: none"> • Introduced an out-of-plane displacement parameter into the correlation coefficient and reduced the computational time by 25%
Hovis and Ranson <i>et al.</i>	1999	<ul style="list-style-type: none"> • Developed a compact instrument for strain measurement in a variety of environment based on the Geometric Approach equation
Lu and Cary	2000	<ul style="list-style-type: none"> • Applied a second-order approximation to determine the first and second-order displacement gradient • Implemented a third-order polynomial interpolation to reconstruct the gray values
Cheng <i>et al.</i>	2002	<ul style="list-style-type: none"> • Introduced the Bicubic Spline deformation function to represent the 2D continuous intensity fields
Hung <i>et al.</i>	2003	<ul style="list-style-type: none"> • Introduced an algorithm known as Fast And Simple
D. Amodio <i>et al.</i>	2003	<ul style="list-style-type: none"> • Revised the Fast-Fourier Transform to process hundreds of images within a reasonable time
Meng <i>et al.</i>	2007	<ul style="list-style-type: none"> • Introduced an iteration spatial gradient, finite element smoothing and 2D generalized cross-validation algorithm
Cofaru <i>et al.</i>	2010	<ul style="list-style-type: none"> • Improved the Newton-Raphson iteration scheme by introducing an adaptive spatial regularization • Minimized the correlation process by utilizing the neighboring motions information

2.4 Accuracy Analysis of the Digital Image Correlation

For the last three decades, the Digital Image Correlation (DIC) algorithms has been invented, developed, modified and improved in order to increase the accuracy of the strain measurement and also to reduce the computational time drastically. At the same time, researchers were always aware of the potential errors encountered in the DIC algorithms and researches have been carried out to investigate the systematic errors, as well as to optimize the parameters that were used in the DIC algorithms. In 1988, Sutton *et al.* [38] observed the systematic errors such as wrong approximation of the deformed subimage shape and the acquired images were out of focus during the experiment. A modelling work was conducted and the primary factors that influenced the accuracy of DIC method were pointed out. B. Wattrisse *et al.* [39] and Schreier *et al.* [40, 41] further investigated the systematic errors such as inappropriate correlation function, improper intensity interpolation and undermatched subset shape function. In their work, they proposed methods to reduce and limit these errors to an acceptable level.

In 2003, Zhang *et al.* [42] examined the influences of the speckle size and the speckle density in terms of accuracy for strain measurement by DIC. A quantitative estimation of the optimum speckle size was suggested to increase the accuracy of the results. In their report, the optimal speckle size was found to be depended on the subset size. For example, the optimal speckle size was found to be 2 pixels when the subset size was 11×11 pixels. Meanwhile, little contribution of the speckle density was reported to the accuracy of subpixel registration. Lecompte *et al.* [43] studied the efficiency of the speckle pattern for in-plane displacements with respect to the subset size. In their work, the speckle pattern's images were numerically deformed and the deformation was simulated by using the finite element software. Since the coordinate system for the deformed image and the finite element model were identical, all the nodal displacements were obtained successfully. Sun *et al.* [44] further investigated the influences of the subset size and the image pattern quality. They claimed that the larger the subset size, the smaller the standard deviations and higher level of accuracy was achieved.

In 2007, Haddadi *et al.* [45] studied on the errors associated to the lighting, optical lens, video camera sensor, out-of-plane displacement, speckle pattern, grid

pitch, subset size and the correlation algorithm. They concluded that the light source must provide a uniform lighting condition throughout the entire zone of interest, special clumps to be used in order to minimize the out-of-plane displacement, an optimize pattern must be printed on the sample in order to get a more reproducible results and the choice of the grid pitch depends according to the application objective. Recently, Jerabek *et al.* [46] further analyzed the effects of various parameters related to the DIC experimental set-up. The light intensity, camera shutter time, speckle pattern structure, machine, temperature and vibrations were the parameters tested in this work. They revealed that the fine speckle pattern and a light intensity provided an accurate result when it was under overexposure condition. Besides, they reported that the vibration had not much effect in decreasing the strain measurement accuracy. In contrast, pronounced influence was observed in terms of the accuracy for the operational temperature. Table 2.2 summarizes the accuracy analysis of the DIC algorithms over the years.

Table 2.2 The accuracy analysis of the DIC algorithms

Researchers	Year	Remarks for the Accuracy Analysis of the DIC Algorithms
Sutton <i>et al.</i>	1988	<ul style="list-style-type: none"> Observed the systematic errors such as wrong approximation of the deformed subimage shape and the images were out of focus during the experiment
B. Wattrisse <i>et al.</i> and Schreier <i>et al.</i>	2000	<ul style="list-style-type: none"> Investigated the systematic errors such as inappropriate correlation function, improper intensity interpolation and undermatched subset shape function
Zhang <i>et al.</i>	2003	<ul style="list-style-type: none"> Examined the influences of the speckle size and the speckle density in terms of accuracy Suggested the optimum speckle size
Lecompte <i>et al.</i>	2006	<ul style="list-style-type: none"> Studied the efficiency of the speckle pattern for in-plane displacements with respect to the subset size
Sun <i>et al.</i>	2007	<ul style="list-style-type: none"> Investigated the influences of the subset size and the image pattern quality
Haddadi <i>et al.</i>	2007	<ul style="list-style-type: none"> Studied on the errors associated to the lighting, optical lens, video camera sensor, out-of-plane displacement, speckle pattern, subset size and the correlation algorithm
Jerabek <i>et al.</i>	2010	<ul style="list-style-type: none"> Analyzed the effects of various parameters related to the DIC experimental set-up such as the light intensity, camera shutter time, speckle pattern structure, machine, temperature and vibrations

2.5 Applications of the Digital Image Correlation in 2D Measurement

The Digital Image Correlation (DIC) was first applied in experimental mechanics to measure two-dimensional deformation measurement [21-22, 47]. For example, the whole field displacement analysis of the composite cylinders was examined and the surface profile of a specimen under loading was measured by DIC [48-49]. However, for the last three decades, various applications have been reported as the DIC technique was widely acceptable. The most common applications of the two-dimensional DIC were found in fracture mechanics such as the study of plastic deformation around a notch or open hole and the fracture surfaces of a specimen under tensile loading [50-53], as well as the crack growth behaviour [54-55]. Recently, the researchers have further extended the crack propagation study to the measurement of stress intensity factor [56-57]. This approach was widely accepted as the stress intensity factors were easier to be determined if compared to the conventional method. For example, no assumptions about the boundary conditions were made and the DIC technique required no knowledge about the crack mode during the determination of stress intensity factor. In 1996, Lyons *et al.* [58] applied the DIC technique to measure the full-field surface deformations at high temperature. They claimed that the DIC technique was able to determine the surface deformation of an object at temperatures up to 650°C. Besides, Grant *et al.* [59] and Pan *et al.* [60] further extended the experiments and they claimed that the DIC technique was capable to determine the surface deformation of a specimen at temperatures even up to 1400°C and 600°C respectively (it depends on the quality of the imaging system).

The DIC technique was employed in ophthalmology study in 1987. According to Wu *et al.* [61], the strain fields in the retinal tissue under monotonic and cyclic loading were determined successfully. Hjortdal *et al.* [62] adopted the DIC technique to measure the multi-directional corneal strain, thickness and radius of curvature for human eyeballs. The measurement of strain distributions within the articular cartilage by DIC method were also reported in 2002 [63]. In 1988, the measurement of strains in a paper by DIC method was reported by Chao *et al.* [64] and the mechanical properties of wood were successfully determined using DIC technique [65]. Besides this, the DIC technique was reported to be useful in monitoring the structural integrity of the manmade structures. According to Lee *et al.* [66] and

Chen *et al.* [67], the measurements of dynamic displacement of a bridge by DIC technique were highly cost-effective and easy to be used if compared to the conventional method.

With the micro-fabrication field developing rapidly, many engineering parts are becoming smaller and smaller. Hence, the deformation characteristics of the micro-scale parts must be experimentally tested and the DIC technique was reported to be successfully adopted. In 1997, Sun *et al.* [68] claimed that the DIC technique was able to measure the in-plane surface deformations at magnifications up to 2000 pixels/mm. The DIC technique was further extended to the study of scanning tunnelling electron microscopy images [69-70]. In their report, the mechanical properties of the specimens at the micro-scale level were effectively determined. More recently, the researchers applied the DIC technique to identify the mechanical properties of a material from the displacement measurement [71-72]. According to Tung *et al.* [73], the strain values determined by the strain gauge and the DIC method were close to each other. In their report, modulus of elasticity of the steel sample obtained by strain gauge and DIC method was 201.6 GPa and 200.5 GPa respectively. Besides this, Leclerc *et al.* [74] further utilized the concept and determined the mechanical properties of a material by finite element based integrated DIC. They claimed that the newly developed technique was able to enhance the accuracy and the robustness of the identification process. Table 2.3 summarizes the applications of the DIC in two-dimensional measurements over the years.

Table 2.3 The applications of the DIC in two-dimensional measurements

Researchers	Year	Remarks for the Applications of the DIC in 2D Measurement
Sutton <i>et al.</i>	1983	<ul style="list-style-type: none"> Measured the 2D deformation in experimental mechanics
Wu <i>et al.</i>	1987	<ul style="list-style-type: none"> Determined the strain field in the retinal tissue
Chao <i>et al.</i>	1988	<ul style="list-style-type: none"> Measured of the strains in a paper
Peters <i>et al.</i>	1989	<ul style="list-style-type: none"> Measured the surface profile of the composite cylinder under loading
Lyons <i>et al.</i>	1996	<ul style="list-style-type: none"> Measured the surface deformations at high temperature
Sun <i>et al.</i>	1997	<ul style="list-style-type: none"> Measured the deformation characteristics of the micro-scale parts

Table 2.3 The applications of the DIC in two-dimensional measurements

Researchers	Year	Remarks for the Applications of the DIC in 2D Measurement
Bueno <i>et al.</i>	2002	<ul style="list-style-type: none"> • Studied the crack growth behaviour
Wang <i>et al.</i>	2002	<ul style="list-style-type: none"> • Measured the strain distributions within the articular cartilage
Diaz <i>et al.</i>	2004	<ul style="list-style-type: none"> • Studied the deformations around a notch or open hole
Stephane and Francois	2006	<ul style="list-style-type: none"> • Performed the measurement of stress intensity factor
Lee <i>et al.</i>	2006	<ul style="list-style-type: none"> • Measured the dynamics displacement of a structure
Hild and Roux	2006	<ul style="list-style-type: none"> • Identified the mechanical properties of a material from the displacement measurement

2.6 Chapter Summary

In the beginning of this chapter, the fundamental concepts or the working principle of the Digital Image Correlation (DIC) was discussed. The reasons why the random speckle patterns were used in the DIC technique were revealed. In the development of the DIC algorithms section, the proposed DIC algorithms in the last three decades were reviewed in detail. From the research papers, majority of the researchers were focused on the algorithms which determined the in-plane displacement based on the matching of the subsets' intensity pattern in the reference and the deformed images. Over the years, the DIC algorithms have been modified and improved in order to obtain the results with high degree of accuracy, as well as to shorten the computational time drastically.

However, many errors occurred for the image correlation process as the accuracy of the results was mainly relied on the intensity pattern values. Accuracy analysis of the DIC algorithms was performed by the researchers and the primary factors such as inappropriate correlation function, improper intensity interpolation and etc. that influenced the accuracy of DIC method were pointed out. However, by referring to Hovis work, the systematic errors stated above can be avoided as the proposed Centroidal Tracking algorithm managed to determine the full-field deformation

measurement by tracking the displacement of the speckles' centroid instead of correlating the intensity pattern values. Nonetheless, the presented algorithm was limited by manual method of measuring the two points and there was a great need to develop an automated measurement algorithm. Besides the reported systematic errors, the quality of the measurement devices, the working environment and the speckle patterns were studied by various researchers. The optimal experimental set-up and the characteristics of the good quality speckle patterns were revealed. Hence, attention must be given even at the beginning of the experimental works.

Lastly, the applications of the DIC in two-dimensional measurements were reviewed. From the research papers, the applications of the DIC technique were not limited to the experimental mechanics only, applications in the area such as ophthalmology and biomechanical were also reported in the literature. In general, the DIC techniques were proved to be practical in the displacement measurement regardless of the area of applications. Nevertheless, researches are needed to be done in the future to simplify further the DIC techniques, as well as to expand its capability in strain measurement.

CHAPTER 3

METHODOLOGY

3.1 Chapter Overview

In this chapter, the research methodology for the development of an optical strain measurement method is discussed. First of all, the Geometric Approach equation used in this study was validated by ANSYS simulation model with the aid of the analytical calculations in Microsoft Excel spreadsheet. The validation of the Geometric Approach equation was considered important as to prove its suitability or accuracy in the deformation measurement using Digital Image Correlation technique.

Next, the development of the strain measurement algorithm was carried out and the Image Processing Toolbox in MATLAB was used to develop the strain measurement program. The MATLAB program was then executed with a pair of images created by AutoCAD. The AutoCAD images consisted of four white dots which represent the selected speckles and the Cartesian coordinates of the white dots were extracted from the ANSYS simulation models. By doing this, the optical strain measurement method was verified by comparing its results with the ANSYS simulation models.

In order to apply the MATLAB program, tensile tests were conducted and the results determined by the optical strain measurement method were validated with the benchmark values set by the extensometer. By using the Universal Testing Machine (UTM), two types of samples made of mild steel and polypropylene materials were tested. At the same time, videos were recorded during the strain inducing event by a consumer version of high-definition video camera. The recorded videos were then processed and a series of images were extracted from the recorded videos. Next, the extracted images were analyzed and the strain values were determined by using the

optical strain measurement method. Lastly, the results obtained by the extensometer and the optical strain measurement method were verified and the deviations in terms of percentage were presented. Fig. 3.1 shows the project work flow of this study.

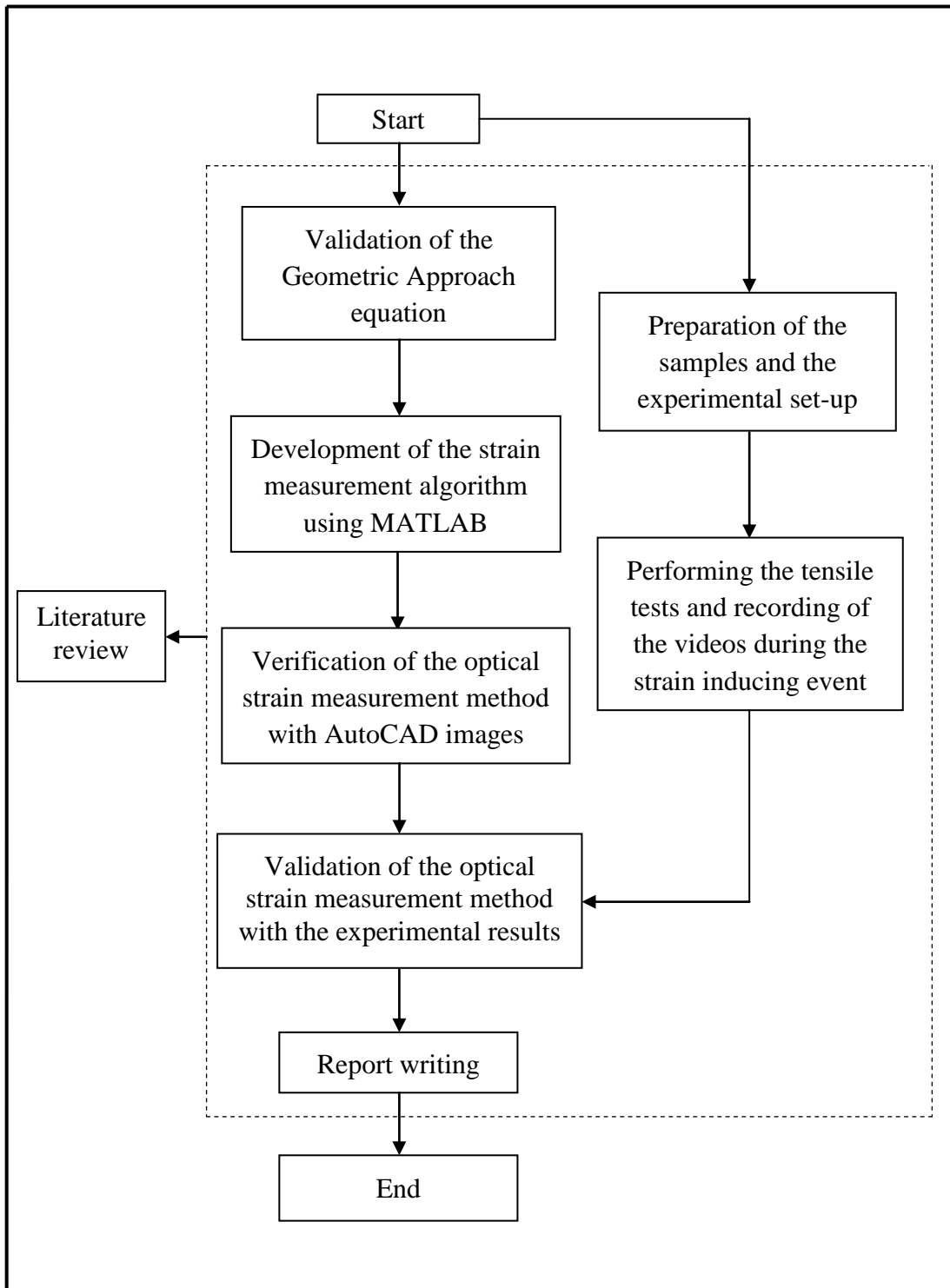


Fig. 3.1 Project work flow of this study

3.2 Validation of the Geometric Approach Equation

By referring to the theory of continuum mechanics, the Geometric Approach equation [34] was derived and used to measure the strain in a deformed body. This can be achieved by measuring the relative change in distance between two or more points within a structural component. For the three-dimensional strain measurement, the relative elongation between two points, ε can be expanded in terms of the strain components ε_{ij} and the strain components are then determined using the equation as shown below

$$\begin{aligned} \frac{1}{2} \varepsilon^2 + \varepsilon = & \varepsilon_{xx} \cos^2 \theta_x + \varepsilon_{yy} \cos^2 \theta_y + \varepsilon_{zz} \cos^2 \theta_z + 2\varepsilon_{xy} \cos \theta_x \cos \theta_y \\ & + 2\varepsilon_{xz} \cos \theta_x \cos \theta_z + 2\varepsilon_{yz} \cos \theta_y \cos \theta_z \end{aligned} \quad (3.1)$$

For the surface measurements, the Geometric Approach equation was reduced to two-dimensional form and is expressed as

$$\frac{1}{2} \varepsilon^2 + \varepsilon = \varepsilon_{xx} \cos^2 \theta_x + \varepsilon_{yy} \cos^2 \theta_y + 2\varepsilon_{xy} \cos \theta_x \cos \theta_y \quad (3.2)$$

The details of the Geometric Approach equation were discussed in section 2.2. Nevertheless, the Geometric Approach equation was seldom being applied in the measurement of strain using Digital Image Correlation (DIC) technique. However in 1989, Hovis [33] was the first researcher who applied the Geometric Approach equation to determine the two-dimensional full-field deformation measurements using DIC technique. In his doctoral dissertation, the Geometric Approach equation was embedded inside the Centroidal Tracking algorithm. This algorithm was further used to determine the two-dimensional deformation measurement by tracking the displacement of the speckles' centroid. Although Hovis was able to determine the strain values successfully, but no validation of the Geometric Approach equation was presented to show its suitability or accuracy in the deformation measurement using DIC technique. Therefore in this study, the Geometric Approach equation was validated by ANSYS simulation model with the aid of the analytical calculations in Microsoft Excel spreadsheet before the equation was being applied.

3.2.1 Numerical Analysis by ANSYS Simulation Models

For the validation of the Geometric Approach equation, a total of four bar models had been created in ANSYS. Two models represented the mild steel samples and the other two represented the polypropylene samples. These modelling consisted of two-dimensional and three-dimensional models that were subjected to the tensile test simulation. By referring to the mild steel certificate (refer to Appendix A) and the polypropylene handbook [75], the material properties were fixed to the values that were exactly the same as the real samples. For example, the Poisson's ratio for the mild steel model was fixed to 0.30 while for the polypropylene model was fixed to 0.37. In this numerical analysis, the input of the displacement values was limited within the elastic region. The allowable maximum displacement within the elastic region was determined using the theory of elasticity as shown below

$$\mathbf{Max. Strain}_{Elastic Reg.} = \frac{\mathbf{Proportional Limit}}{\mathbf{Modulus of Elasticity}} \quad (3.3)$$

$$\mathbf{Max. Disp.}_{Elastic Reg.} = \mathbf{Max. Strain}_{Elastic Reg.} \times \mathbf{Original Length} \quad (3.4)$$

By using the above equation, the allowable maximum displacement within the elastic region for all models was determined. Table 3.1 shows the parameters for the modelling of the mild steel and the polypropylene samples.

In general, the modelling processes for the mild steel and the polypropylene were identical. A total of three phases were involved during the modelling of the two-dimensional and the three-dimensional samples, i.e. Pre-Processing Phase, Solver or Processing Phase and lastly the Post-Processing Phase. All these phases, especially the Pre-Processing Phase, the bar models must be created precisely, as well as the boundary conditions must be assigned correctly in order to obtain accurate results.

Table 3.1 Parameters for the modelling of mild steel and polypropylene samples

Parameters	Mild Steel		Polypropylene	
	2D	3D	2D	3D
Width (x -axis)	6.25 mm (Real sample dim.: 12.50 mm)		5.1 mm (Real sample dim.: 10.20 mm)	
Length (y -axis)	25 mm (Real sample dim.: 50 mm)		25 mm (Real sample dim.: 50 mm)	
Thickness (z -axis)	-	3 mm (Real sample dim.: 6 mm)	-	2.125 mm (Real sample dim.: 4.25 mm)
Modulus of Elasticity	207 GPa / 30×10^6 psi		1500 MPa / 217.5×10^3 psi	
Proportional Limit	323 MPa		34 MPa	
Poisson's Ratio	0.30		0.37	
Type of Loading: Displacement	$-U_y = 0.039$ mm (applied on the bottom face of the bar models)		$-U_y = 0.56$ mm (applied on the bottom face of the bar models)	

3.2.1.1 Pre-Processing Phase

In the Pre-Processing Phase, the two-dimensional and the three-dimensional bar models were created by using ANSYS. For the two-dimensional bar models, only the length and the width were used in the modelling of the samples. While for the modelling of the three-dimensional bar models, the thickness of the samples was included. By referring to the real samples' dimensions shown in Table 3.1, 1 / 4 scale model was used to represent the real samples in two-dimension as the bar models were symmetrical in x and y directions. Meanwhile for the three-dimensional models, 1 / 8 scale model was used as the bar models were symmetrical in x , y and z directions. By doing this, the modelling procedure such as the input of the boundary conditions can be simplified further and the computational time can be reduced significantly.

After creating the bar models in ANSYS, the element types *Plane 42* and *Solid 45* were assigned to the two-dimensional and the three-dimensional models respectively. Besides, the material properties as shown in Table 3.1 were assigned to the mild steel and the polypropylene models. Meshing was then carried out for the bar models and the mesh size was set to 0.25 mm. As shown in Fig. 3.2 and Fig. 3.3, the mesh used in two-dimensional and three-dimensional bar models was extremely fine.

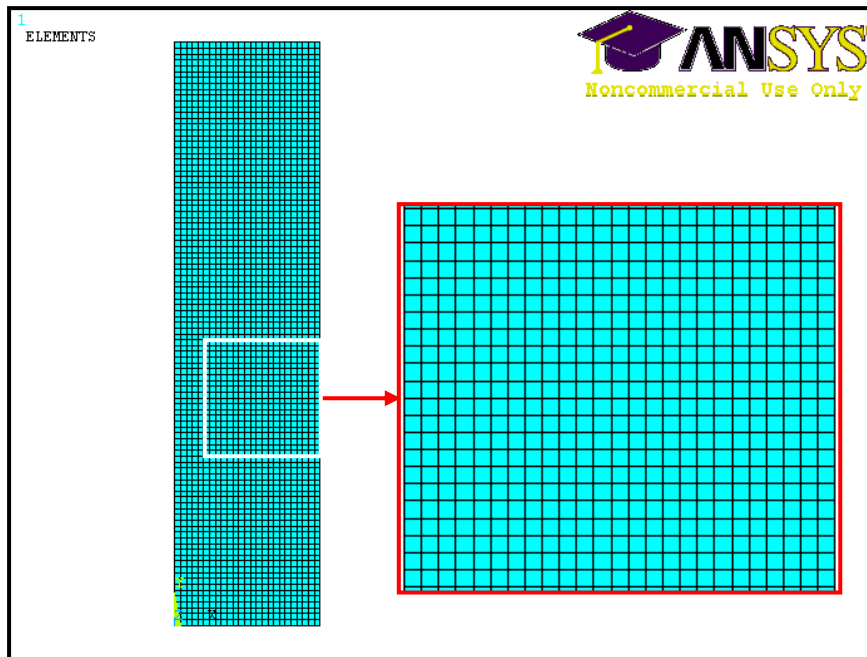


Fig. 3.2 Meshing of two-dimensional bar model

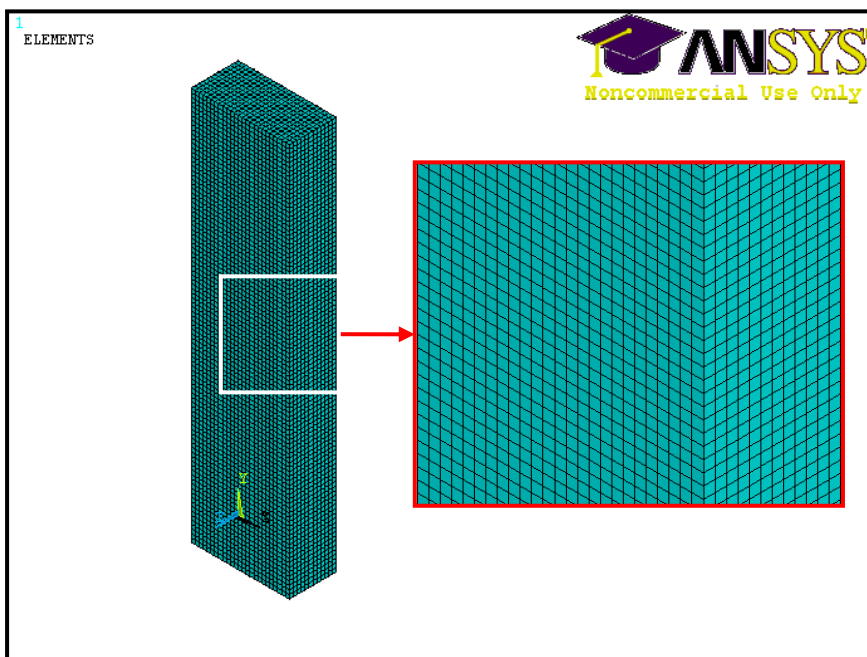


Fig. 3.3 Meshing of three-dimensional bar model

When all the tasks above were accomplished, the boundary conditions of the bar models were set accordingly as if the models were subjected to tensile test. For the two-dimensional bar models, the displacement constraints along the x and y -symmetrical plane, U_x and U_y were set to zero. While for the three-dimensional bar models, the displacement constraints were almost the same as in the two-dimensional bar models, except for the displacement of the nodes along the z -symmetrical plane, U_z which was set to zero.

After properly constraining the two-dimensional and the three-dimensional bar models, displacement was applied in y direction to model the strain inducing effect. For example, the displacement in the negative y direction was applied on the bottom face of the bar models. By referring to Table 3.1, the displacements of 0.039 mm and 0.56 mm were applied to the mild steel and the polypropylene models respectively. Fig. 3.4 and Fig. 3.5 show the boundary conditions for the two-dimensional and the three-dimensional bar models respectively.

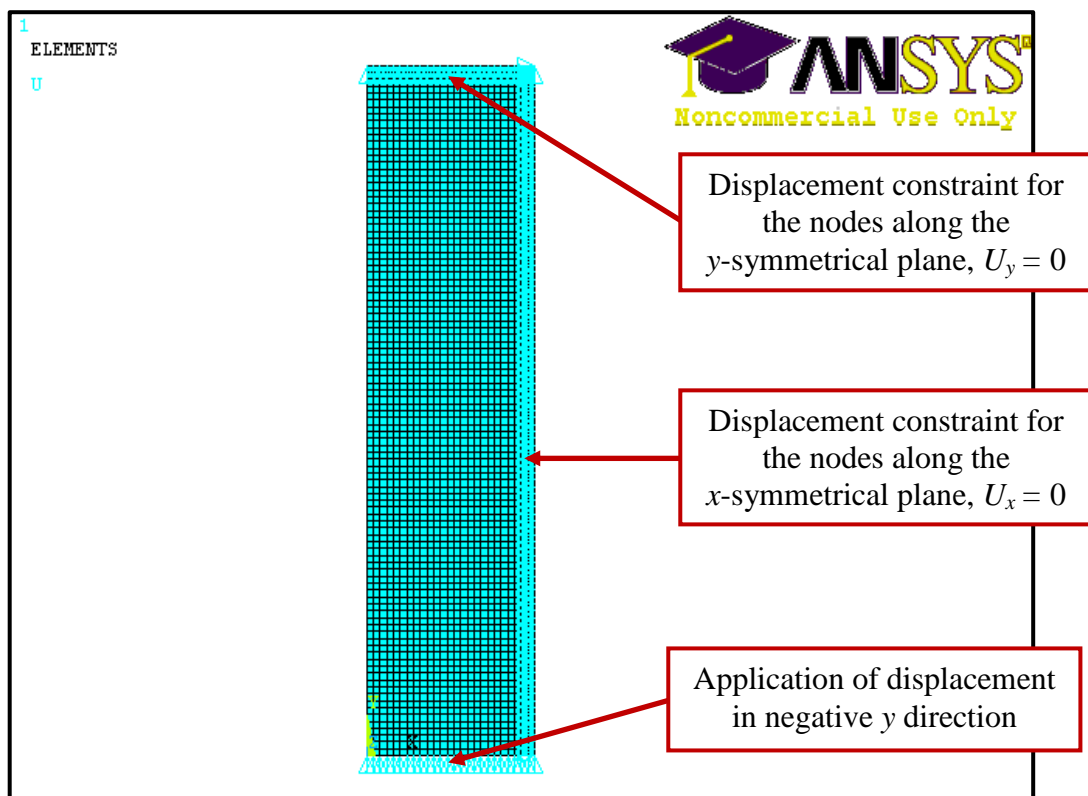


Fig. 3.4 Boundary conditions for the two-dimensional bar model

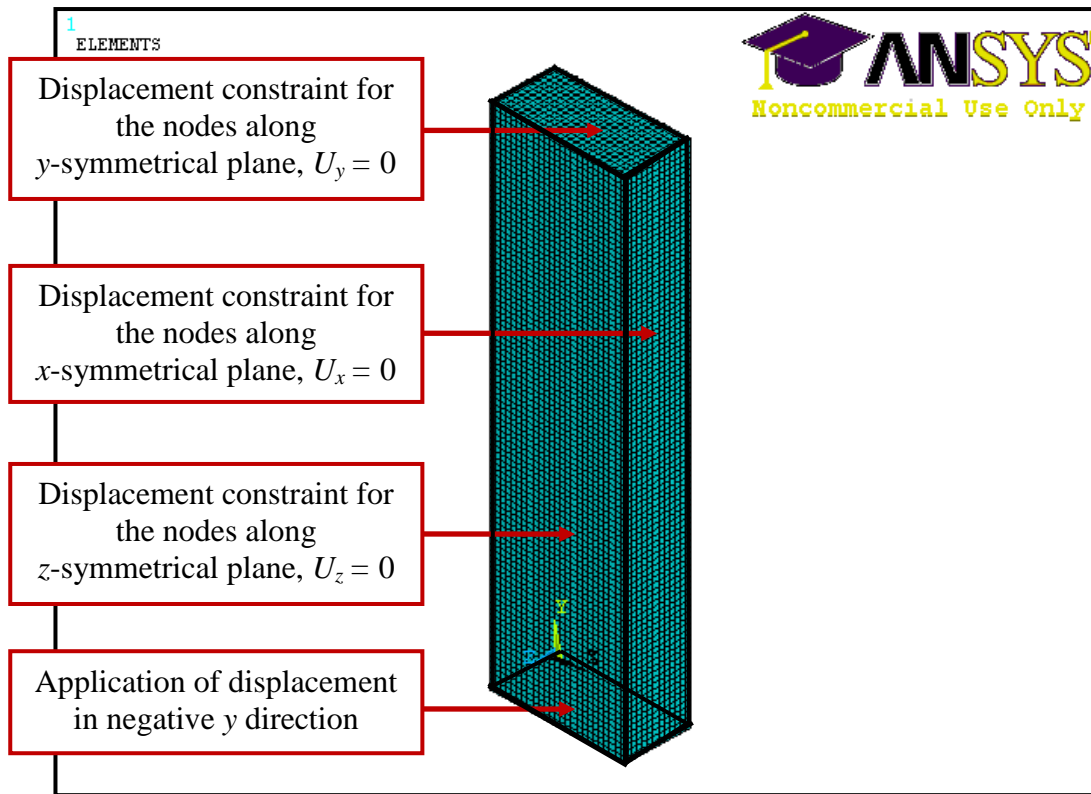


Fig. 3.5 Boundary conditions for the three-dimensional bar model

3.2.1.2 Processing Phase

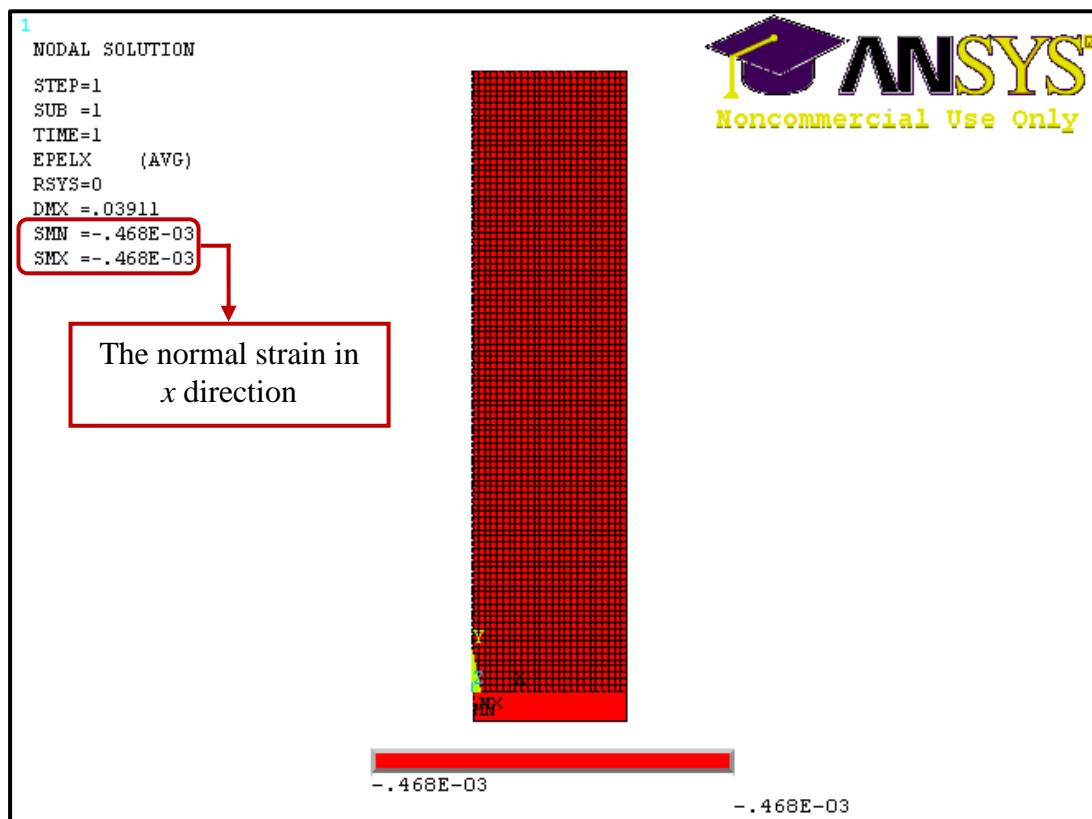
During the Processing Phase, the ANSYS applied the stress-strain relationship to determine the strain values experienced by the bar models and the equation is expressed in the form

$$\sigma = D \times \varepsilon^{el} \quad (3.3)$$

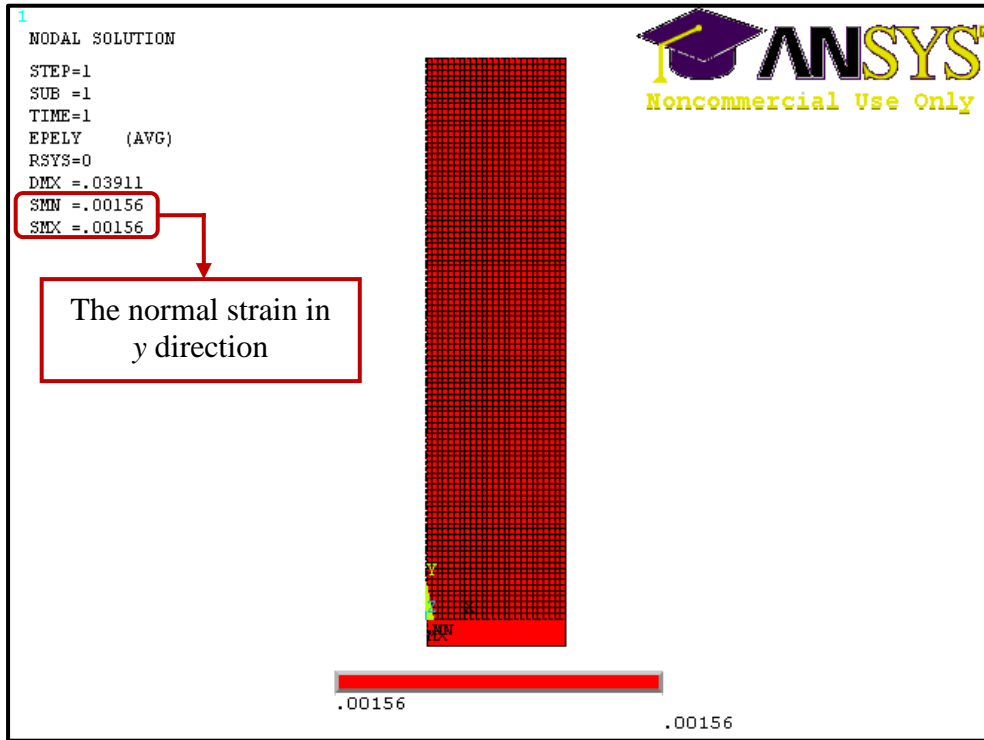
where σ is stress vector, D is the elastic stiffness matrix and ε^{el} is the elastic strain vector [76]. Meanwhile for the computational time, it is directly proportional to the number of nodes and elements in a model, i.e. the fine mesh which provided a large number of nodes and elements will increase the computational time while the coarse mesh which resulted in a small number of nodes and elements will decrease the computational time. In this numerical analysis, the required computational time was longer as the fine mesh was applied in the modelling of the bar models. For example, the two-dimensional bar models contained 2626 nodes and 2222 nodes for the mild steel and the polypropylene samples respectively. While for the three-dimensional bar models, the mild steel and the polypropylene samples contained 34138 nodes and 22220 nodes respectively.

3.2.1.3 Post-Processing Phase

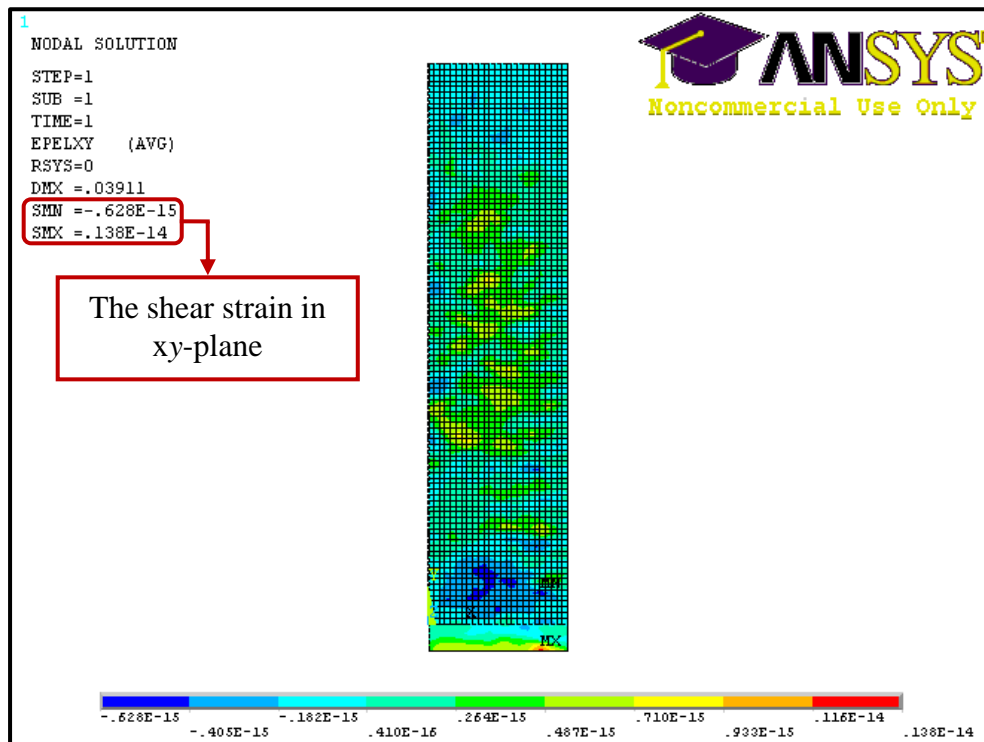
In the Post-Processing Phase, the result interpretation was carried out to determine the strain experienced by the bar models. By using the ANSYS, the normal strain and the shear strain within the elastic limit were obtained. The obtained results were further validated with the simple hand calculations in order to check the correctness of the modelling. For example, the normal strain experienced by the deformed bar model in y direction was manually calculated by dividing the total displacement in y direction with the total length. The manually calculated results should be the same as the results obtained by ANSYS if the modelling were accurate. Fig. 3.6a and Fig. 3.6b show the normal strains obtained by ANSYS in x and y directions respectively for the two-dimensional mild steel models, whereas Fig. 3.6c shows the shear strain obtained by ANSYS in xy -plane. By referring to Fig. 3.6c, the obtained shear strain value was extremely small and therefore treated as zero if compared with the normal strains values.



(a)



(b)



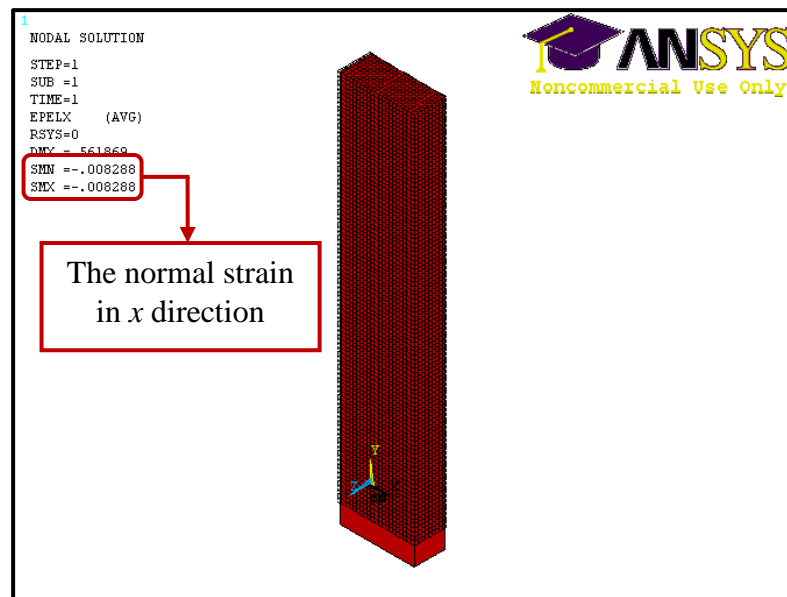
(c)

Fig. 3.6 Results obtained by ANSYS for two-dimensional mild steel models

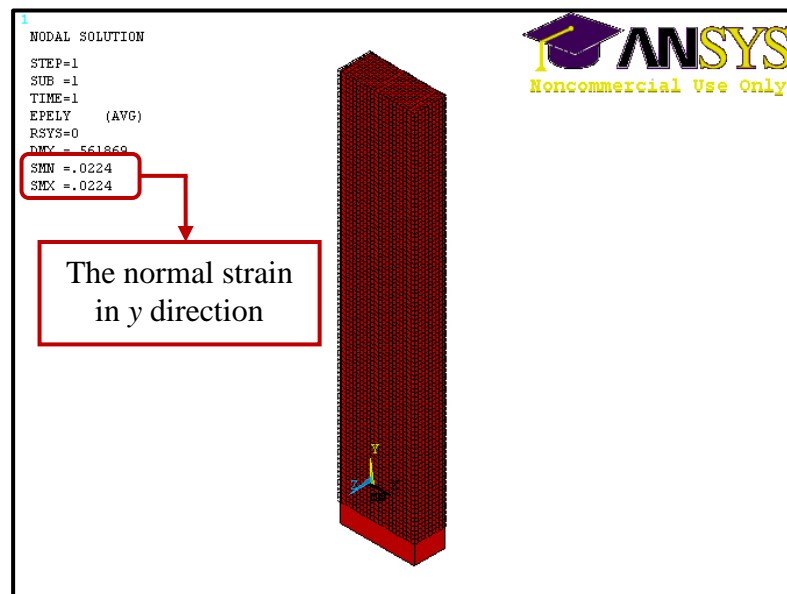
(a) Normal strain in x direction (b) Normal strain in y direction

(c) Shear strain in xy-plane

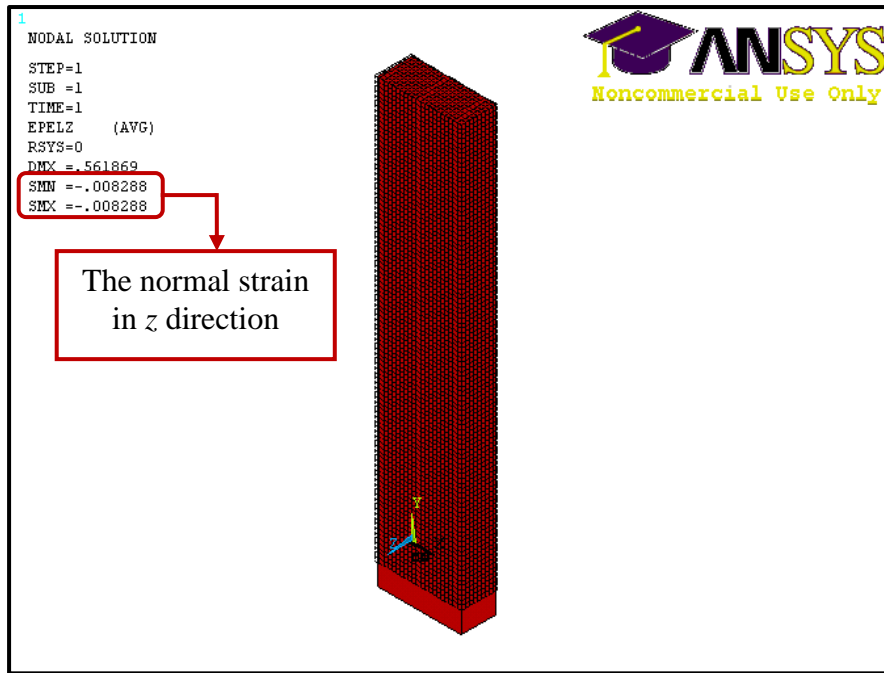
For the determination of the normal strains and the shear strains in the three-dimensional models, the procedure is the same as described above. In order to explain the procedure in detail, either the mild steel or the polypropylene samples can be used here. However, the polypropylene models were selected as the mild steel models were presented earlier in the two-dimensional models. Fig. 3.7 shows the normal strains obtained by ANSYS in x , y and z directions respectively. The shear strains in xy , xz and yz -plane were not discussed here as the values found were negligible if compared to the normal strain values.



(a)



(b)



(c)

Fig. 3.7 Results obtained by ANSYS for three-dimensional polypropylene models

(a) Normal strain in x direction (b) Normal strain in y direction

(c) Normal strain in z direction

By using the ANSYS, the normal strains and the shear strains were determined successfully. There is another reason why the modelling of the bar models are needed in the validation of the Geometric Approach equation, that is to determine the Cartesian coordinates of the respective nodes. The nodes' Cartesian coordinates are important as to validate the Geometric Approach Equation in the Microsoft Excel spreadsheet. From the ANSYS simulation models, the Cartesian coordinates of the respective nodes were extracted twice, once before deformation and the other one after deformation. By using the *list nodes Cartesian coordinates* command, the Cartesian coordinates for all the nodes in x , y and z -axis were determined. Fig. 3.8 shows the Cartesian coordinate of the nodes within the bar models before the strain inducing event took place. After that, the displacements of the respective nodes in x , y and z directions were obtained using the *list nodal solution* command. Fig. 3.9 shows the displacements of the respective nodes in x direction after the deformation occurred. Hence, the nodes' Cartesian coordinates in the deformed models were determined by adding the displaced values to the original nodes' Cartesian coordinates in the undeformed state.

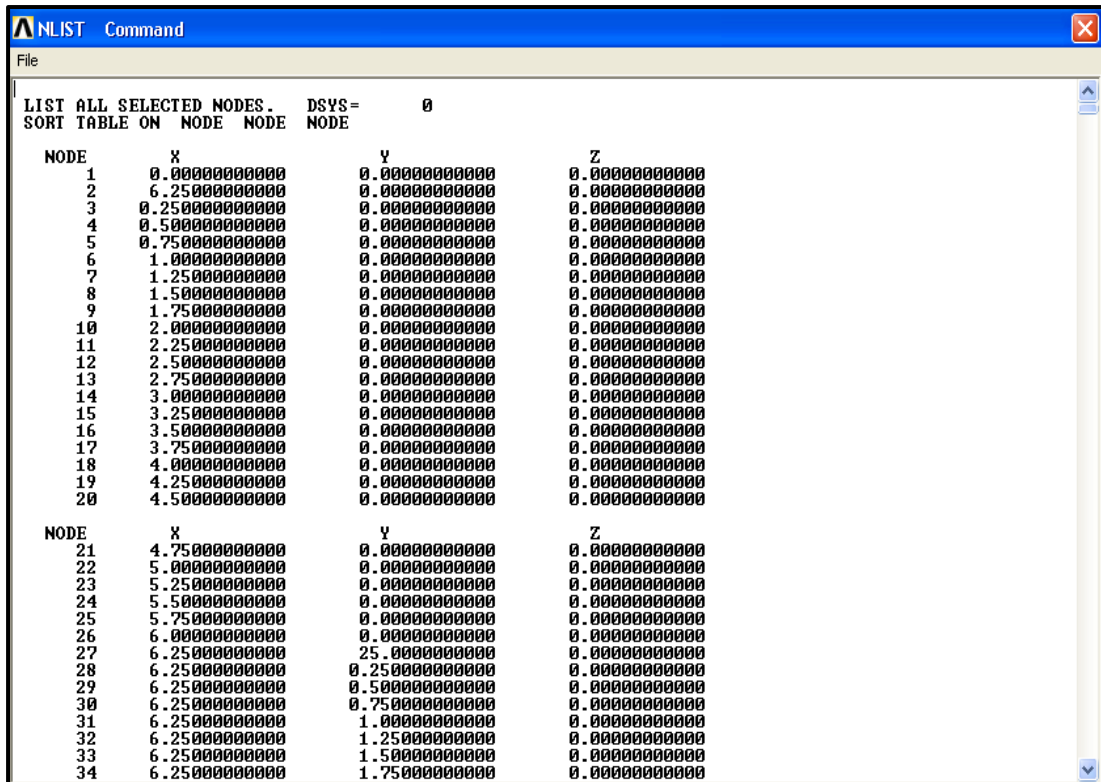


Fig. 3.8 Cartesian coordinates of the nodes in the undeformed model

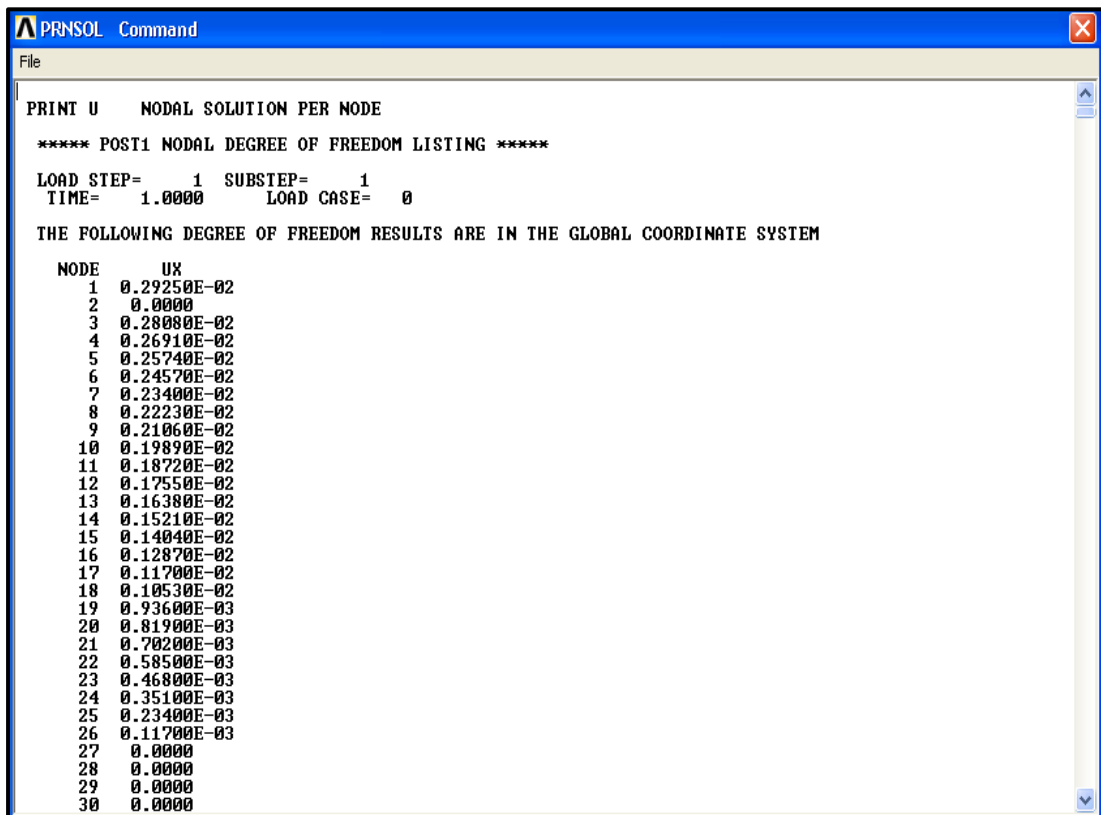


Fig. 3.9 Displacements of the respective nodes in x direction after deformation

3.2.2 Analytical Analysis by Microsoft Excel Spreadsheet

In order to validate the Geometric Approach equation, a total of four calculations were performed manually in the Microsoft Excel spreadsheet where the Geometric Approach equation was embedded. For the analytical analysis, two calculations were performed for the mild steel models and the other two calculations were performed for the polypropylene models in two-dimension and three-dimension respectively. By using the nodes' Cartesian coordinates extracted from the ANSYS models above, the strain values of the bar models were determined using the Microsoft Excel spreadsheet. For the two-dimensional models, the Cartesian coordinates of four nodes were required to solve eq. 3.2 as the Geometric Approach equation has three unknown parameters. While for the three-dimensional models, a total of seven nodes' Cartesian coordinates were required to solve eq. 3.1 as the Geometric Approach equation has six unknown parameters. Fig. 3.10 shows the nodes' Cartesian coordinates that were selected in the middle of the bar models and were further entered in the Microsoft Excel spreadsheets. The left hand side represents the undeformed models while the right hand side represents the deformed models.

Before Deformation					After Deformation		
Node Number	Cartesian Coordinate				Node Number	Cartesian Coordinate	
	x (mm)	y (mm)				x (mm)	y (mm)
591	1	11		*	591	1.002457	10.97816
603	1	14			603	1.002457	13.98284
2274	5.25	11			2274	5.250468	10.97816
2286	5.25	14			2286	5.250468	13.98284

(a)

Before Deformation						After Deformation			
Node number	Cartesian Coordinate				Node number	Cartesian Coordinate			
	x (mm)	y (mm)	z (mm)			x (mm)	y (mm)	z (mm)	
1106	0.971429	11	0		*	1106	1.005647	10.6864	0.017612
1119	4.128571	11	0			1119	4.136622	10.6864	0.017612
1346	0.971429	14	0			1346	1.005647	13.7536	0.017612
1359	4.128571	14	0			1359	4.136622	13.7536	0.017612
2805	0.971429	11	2.125			2805	1.005647	10.6864	2.125
2817	0.971429	14	2.125			2817	1.005647	13.7536	2.125
4092	4.128571	11	2.125			4092	4.136622	10.6864	2.125

(b)

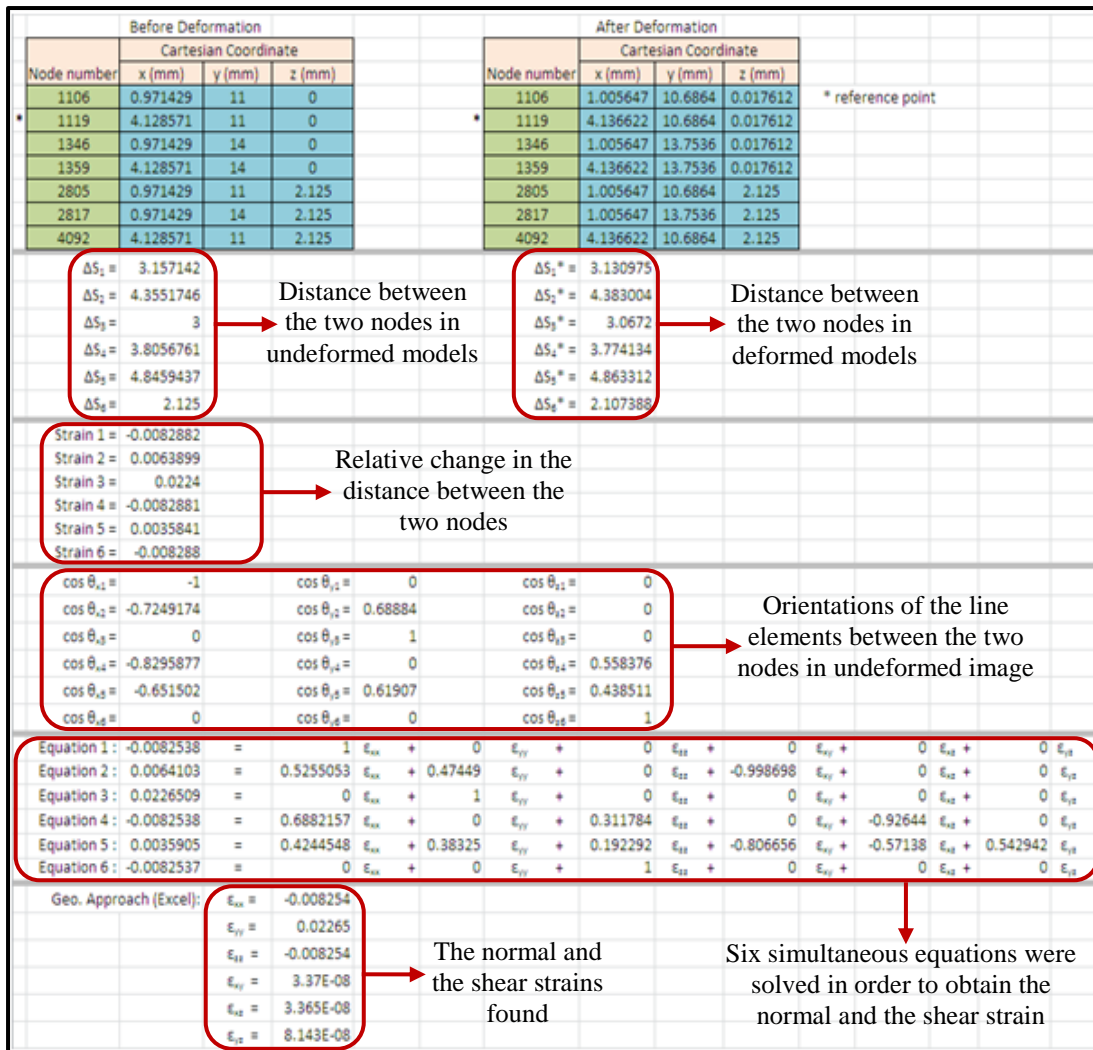
Fig. 3.10 Nodes' Cartesian coordinates entered in the Microsoft Excel spreadsheets

(a) Two-dimensional model (b) Three-dimensional model

The nodes' Cartesian coordinates of the undeformed and the deformed models were entered separately as shown in Fig. 3.10. After this, the distance between the two nodes in the undeformed and the deformed model was then calculated respectively. Hence, the relative change in distance between the nodes was determined using eq. 2.18, as well as the orientations of the line element between the two nodes in the undeformed image were calculated using eq. 2.20 till eq. 2.22. Fig. 3.11 shows the Geometric Approach equation embedded in the Microsoft Excel spreadsheet. For the two-dimensional models, three simultaneous equations were solved in order to obtain the normal strains, ϵ_{xx} and ϵ_{yy} and the shear strain, ϵ_{xy} . While for the three-dimensional models, six simultaneous equations were solved in order to obtain the normal strains, ϵ_{xx} , ϵ_{yy} and ϵ_{zz} and the shear strains, ϵ_{xy} , ϵ_{xz} and ϵ_{yz} .

Before Deformation			After Deformation			
Node Number	Cartesian Coordinate		Node Number	Cartesian Coordinate		
	x (mm)	y (mm)		x (mm)	y (mm)	
* 591	1	11	* 591	1.002457	10.97816	*reference point
603	1	14	603	1.002457	13.98284	
2274	5.25	11	2274	5.250468	10.97816	
2286	5.25	14	2286	5.250468	13.98284	
$\Delta S_1 = 3$ $\Delta S_2 = 4.25$ $\Delta S_3 = 5.20216301$		Distance between the two nodes in undeformed models	$\Delta S_1^* = 3.00468$ $\Delta S_2^* = 4.248011$ $\Delta S_3^* = 5.20323931$		Distance between the two nodes in deformed models	
Strain 1 = 0.00156 Strain 2 = -0.000468 Strain 3 = 0.0002069		Relative change in the distance between the two nodes				
$\cos \theta_{x1} = 0$ $\cos \theta_{x2} = 1$ $\cos \theta_{x3} = 0.81696786$		Orientations of the line elements between the two nodes in undeformed image	$\cos \theta_{y1} = 1$ $\cos \theta_{y2} = 0$ $\cos \theta_{y3} = 0.57668$			
Equation 1: $0.00156122 = 0 \epsilon_{xx} + 1 \epsilon_{yy} + 0 \epsilon_{xy}$ Equation 2: $-0.00046789 = 1 \epsilon_{xx} + 0 \epsilon_{yy} + 0 \epsilon_{xy}$ Equation 3: $0.00020692 = 0.66743649 \epsilon_{xx} + 0.33256351 \epsilon_{yy} + 0.94226328 \epsilon_{xy}$						
Geo. Approach (Excel):		$\epsilon_{xx} = -0.0004679$ $\epsilon_{yy} = 0.00156122$ $\epsilon_{xy} = 9.2656E-09$	The normal and the shear strains found	Three simultaneous equations were solved in order to obtain the normal and the shear strains		

(a)



(b)

Fig. 3.11 The embedded Geometric Approach equation in the Microsoft Excel spreadsheets (a) Two-dimensional model (b) Three-dimensional model

Based on Fig. 3.11, the normal strains and the shear strains were successfully determined by Microsoft Excel spreadsheet where the Geometric Approach equation was embedded. In order to validate the Geometric Approach equation, the obtained results were further compared with the results determined by ANSYS. The results determined by Microsoft Excel spreadsheet and ANSYS should be the same as the two methods were using the same nodes' Cartesian coordinates.

3.3 Development of the Strain Measurement Algorithm

In this section, the strain measurement algorithm was developed. Basically, the strain measurement algorithm is important as it was referred during the development of the MATLAB program. Therefore, the details of the development of the strain measurement algorithm are presented here. In this study, the top-down design [77] was adopted and the development works began with the large tasks, followed by breaking it down into the smaller desirable tasks (subtasks). Besides, all the necessary inputs and the desirable outputs in a subtask were clearly defined. This concept is vital as the subtasks can be coded and tested separately. As a result, each of the subtasks can be verified before combining the subtasks into a complete program.

At the beginning of the development of the strain measurement algorithm, all the desirable tasks were defined clearly. For example, the captured images were processed and the strains experienced by the samples were determined. Next, the subtasks were properly divided as to make sure that the algorithms can be developed separately. Fig. 3.12 shows the work flow for the development of the strain measurement algorithm. In general, the development of the strain measurement algorithm was divided into eight main steps. Firstly, the two images that are acquired at two different states, one before deformation and the other one after deformation are entered into the program, as well as the dimensions of the images in x and y directions are entered in the unit of pixel/mm. Next, the RGB (red, green and blue) images captured earlier are converted into the binary format and the images' features are enhanced according to the light intensity. By selecting the four speckles within the two images respectively, the program will automatically extract the speckles from the random speckle pattern. After that, the centroids of the speckles in term of x and y pixel-coordinate are obtained and the selected speckles are labelled according to the number in sequence. The pixel-coordinate is further converted into the unit of millimeter. Lastly, the embedded Geometric Approach equation in the program will perform the calculation and display the strain values in the MATLAB command windows. Since the surface deformation was studied in this research, only the normal strains, ε_{xx} and ε_{yy} and the shear strain, ε_{xy} were calculated by the optical strain measurement method.

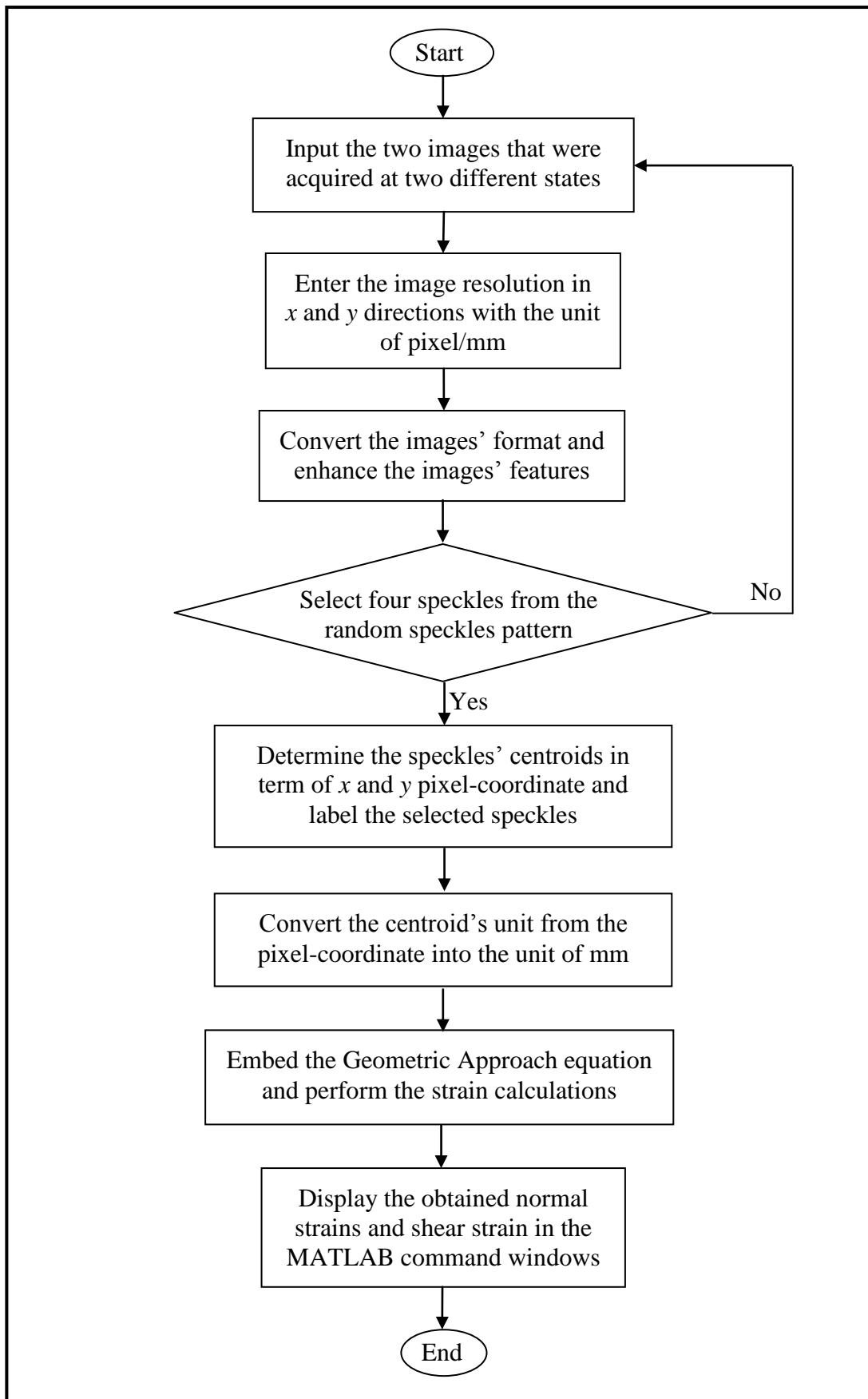


Fig. 3.12 Work flow for the development of the strain measurement algorithm

3.4 Development of the MATLAB Program

When all the subtasks for the development of the strain measurement algorithm were properly divided, the Image Processing Toolbox in MATLAB was used to convert the algorithms into the MATLAB program. By referring to Fig. 3.12, each of the MATLAB statements were coded and tested separately. As a result, the errors in the MATLAB program were easily recognized and the optical strain measurement method can be executed smoothly. The details of the developed MATLAB program are discussed in the following section.

3.4.1 Input the Two Images that were Acquired at Two Different States

At the beginning of the MATLAB program, the two images that were acquired at two different states, one before deformation and the other one after deformation were entered into the program. This can be achieved by using the *imread* function to read the images from different types of file formats, i.e. BMP, GIF, JPEG and PNG into the MATLAB workspace.

3.4.2 Enter the Image Resolution

After the images were entered into the MATLAB workspace, it was necessary to key in the image resolution of the captured images in x and y directions. This can be achieved by using the *input* function in the MATLAB statements. Normally the resolutions of the images are represented by the unit of pixel. However in the Digital Image Correlation technique, the unit of the image resolution was then converted into pixel/mm. By doing this, the displacements of the speckles in the unit of millimetre can be determined.

Fig. 3.13 shows the two images that were used to determine the image resolutions of the captured images in this study. Since the two images have the pixel resolutions of 1920 (vertical axis) \times 1080 (horizontal axis), the unit of the images was converted into pixel/mm. By referring to Fig. 3.13, the total lengths of the mild

steel and the polypropylene images captured by the video camera were 29.5 mm and 30.5 mm respectively. Therefore, the image resolutions for the mild steel and the polypropylene samples in y direction were 65.1 pixels/mm and 63.0 pixels/mm respectively. While for the image resolutions in x direction, the determined values were 68.8 pixels/mm and 66.7 pixels/mm for the mild steel and the polypropylene samples respectively as shown in Fig. 3.14.

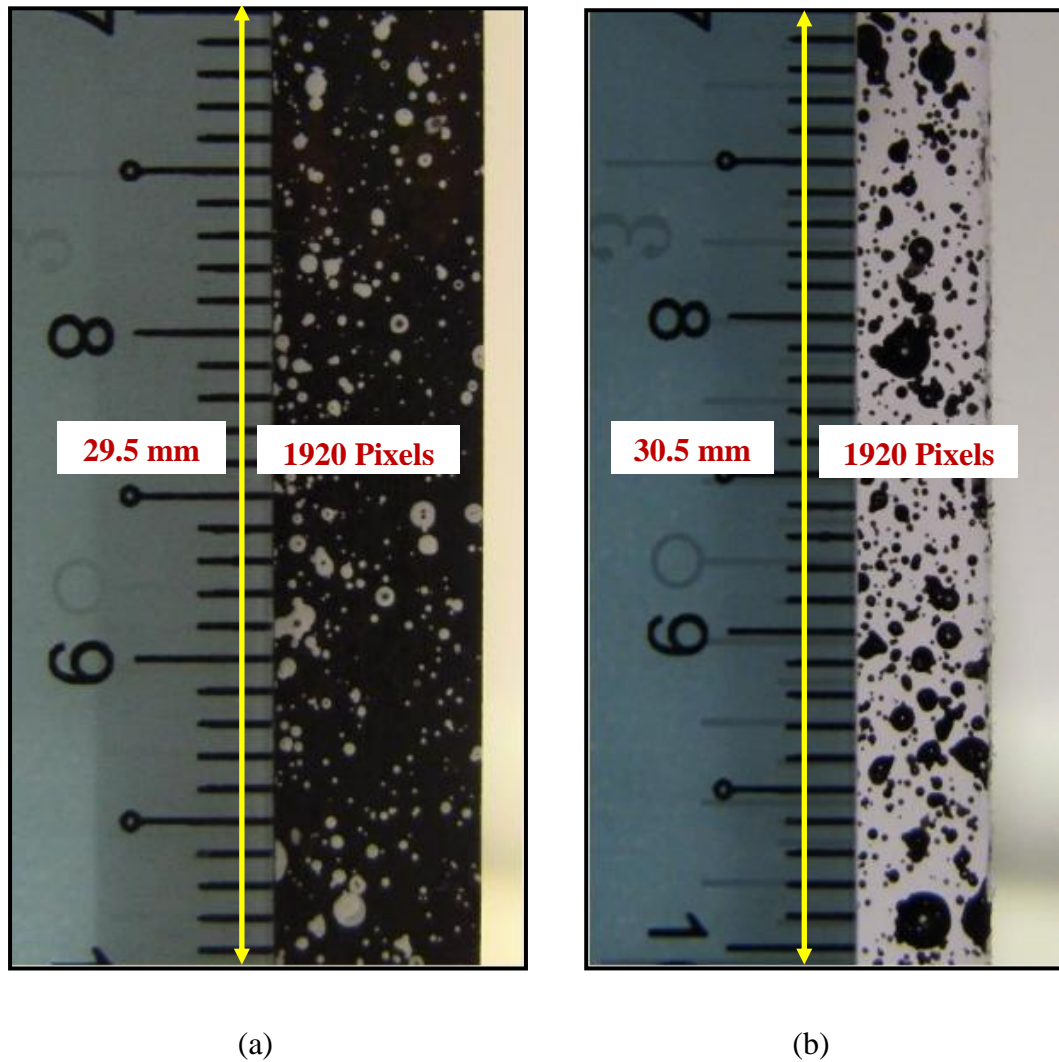


Fig. 3.13 The image resolutions of the images in y direction
(a) Mild steel sample (b) Polypropylene sample

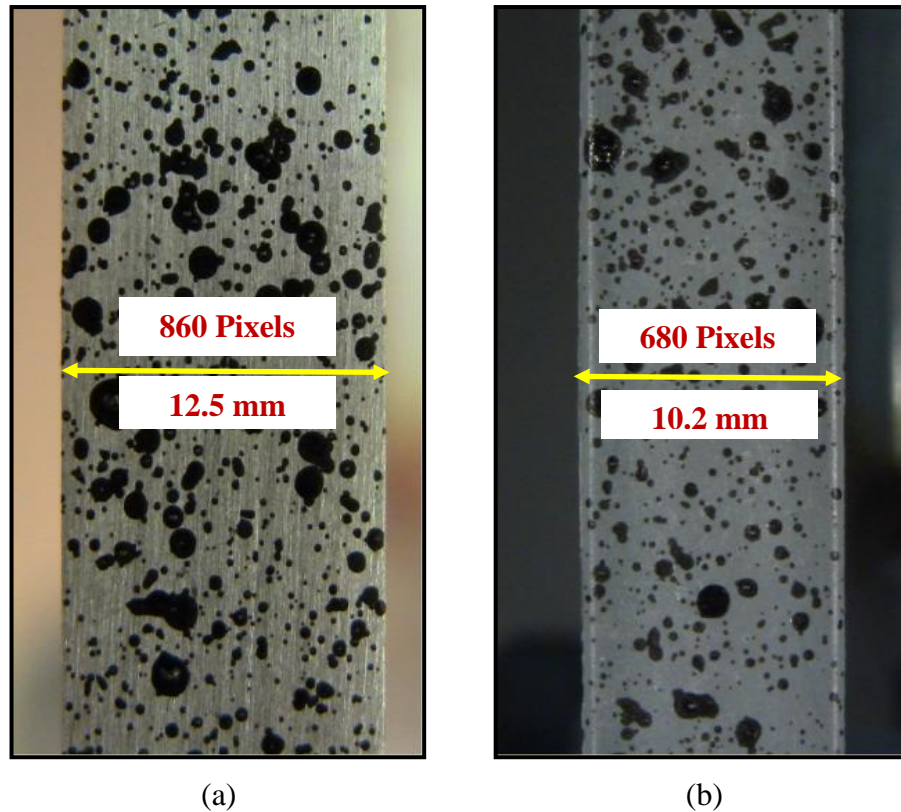


Fig. 3.14 The image resolutions of the images in x direction
 (a) Mild steel sample (b) Polypropylene sample

3.4.3 Conversion of the Images' Format and the Enhancement of the Images' Features

The binary format is preferred in the Digital Image Correlation technique as the binary images only contained black and white colours. As a result, the edges of the speckles are easily differentiated from the surface of the specimen. However in this study, the format of the images captured using a consumer version of high-definition video camera was Joint Photographic Experts Group (JPEG). Therefore, the *im2bw* function was used to convert the JPEG format images to the binary format. Besides, the threshold value in the range of zero (black) to one (white) was specified according to the image's intensity value. By referring to the original images, the threshold values were specified to 0.28 and 0.30 for the mild steel and the polypropylene images respectively. These values were decided as the converted images (binary format) were perfectly representing the original images in terms of the speckles size and the speckles intensity.

3.4.4 Selection of the Four Speckles from the Random Speckles Pattern

In order to determine the surface deformations of the mild steel or the polypropylene samples, a total of four speckles were selected from the random speckles pattern. However, there is a rule for the selection of the four speckles from the random speckles pattern. The same four speckles must be selected in the undeformed and the deformed images as shown in Fig. 3.15. By understanding the above condition, the MATLAB function, *bwselect* was applied to select the objects in a binary image.

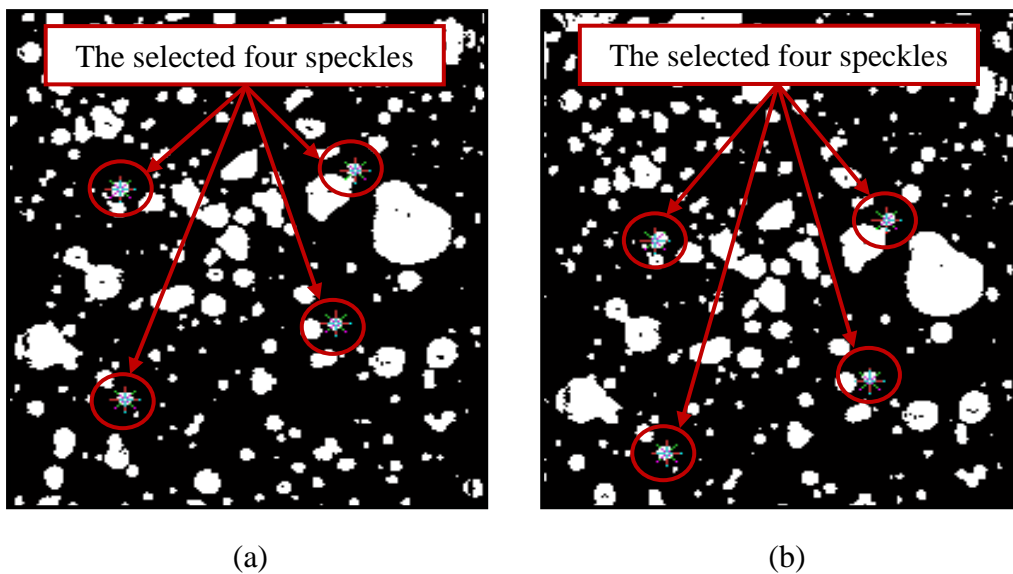


Fig. 3.15 Selection of the four speckles from the random speckles pattern
(a) Undeformed image (b) Deformed image

3.4.5 Determination of the Speckles' Centroid

In this study, the deformation measurement was performed by correlating the displacement of the speckles' centroid in the undeformed and the deformed images. Therefore, the determination of the speckles' centroid in this section is very important. A series of MATLAB functions were applied in order to determine the centroids of the selected speckles (refer to Appendix B). Besides, the MATLAB function, *bwlabel* was applied to label the selected speckles and the *plot* function was used to plot the numbers onto the centre of the selected speckles. As a result, the centroids of the selected speckles can be easily recognized by referring to the assigned number as shown in Fig. 3.16.

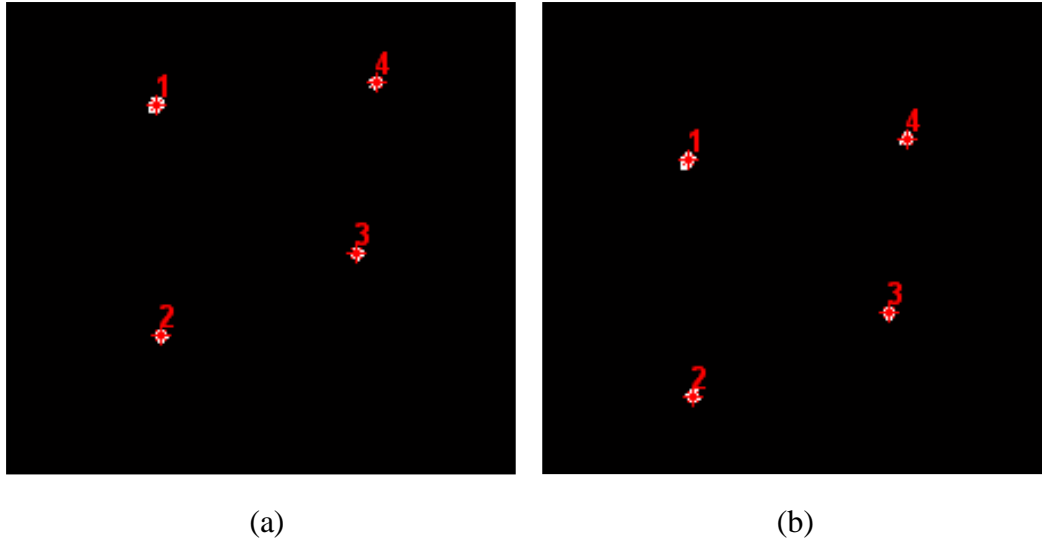


Fig. 3.16 Labelling of the selected speckles according to the number in sequence
(a) Undeformed image (b) Deformed image

3.4.6 Conversion of the Centroid's Unit

By referring to section 3.4.5, the determined centroids' values are stored in the MATLAB workspace accordingly. In general for an image, the unit for the obtained centroids' values is in pixel instead of the commonly used Cartesian coordinate. Therefore, the conversion of the centroid's unit from pixel to millimetre has to be carried out in order to perform the displacement measurement.

3.4.7 Embed the Geometric Approach Equation and Perform the Calculations

In this section, the Geometric Approach equation was embedded inside the MATLAB program in order to calculate the two-dimensional deformation measurement. By having the centroids' values determined in section 3.4.5 and section 3.4.6, the first two parts of the embedded equation (refer to Appendix B) were used to calculate the distance between the two speckles in the undeformed and deformed images, followed by the third equation which was used to calculate the relative change in the distance between the two speckles. Next, the orientations of the line elements between the two speckles in the undeformed image were calculated. Lastly, the Geometric Approach equation in the matrix form was

embedded inside the program and was used to solve the three simultaneous equations.

3.4.8 Displaying the Obtained Results in the MATLAB Command Windows

Normally, the determined strain values are stored inside the MATLAB workspace and the extraction of the obtained strain values is considered inconvenient. Therefore, the MATLAB function, *disp* was used to display the obtained strain values in the MATLAB command windows. Fig. 3.17 shows the obtained normal strains, ϵ_{xx} and ϵ_{yy} and the shear strain, ϵ_{xy} displayed in the MATLAB command windows.

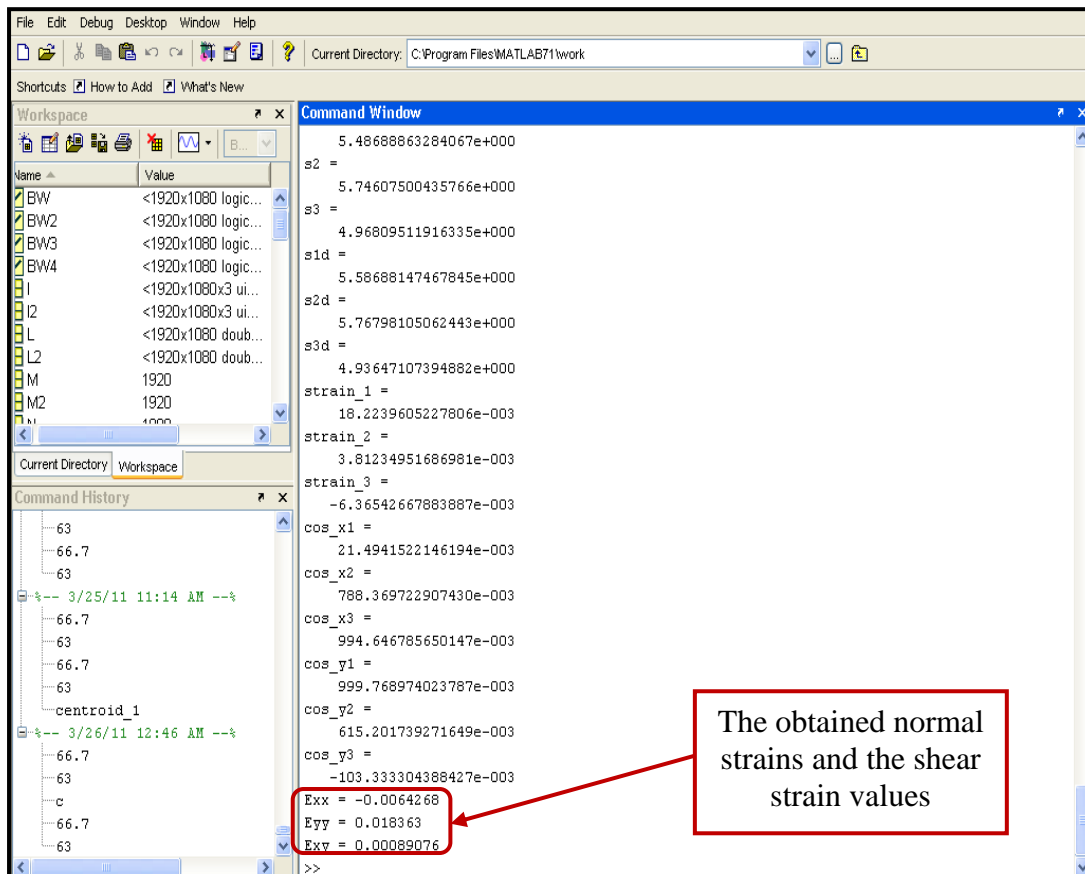


Fig. 3.17 The obtained strain values in the MATLAB command windows

3.5 Verification of the Optical Strain Measurement Method with AutoCAD Images

By combining all the eight subtasks' of programming codes shown in section 3.4, a two-dimensional strain measurement MATLAB program was developed (refer to Appendix B). Before the MATLAB program is used to analyze the images that are captured during the strain inducing event, it is necessary to verify the optical strain measurement method with the AutoCAD images. Basically, the AutoCAD images as shown in Fig. 3.18 consist of four white dots which represented the selected speckles in the undeformed and the deformed images respectively. Since the Cartesian coordinate of the white dots were extracted from the ANSYS simulation models previously (refer to section 3.2.1), it is reasonable to assume that the results determined by the optical strain measurement method are the same as the results of ANSYS simulation models. The optical strain measurement method was verified to be accurate as the deviations of the results determined by the two methods mentioned above were found to be very small.

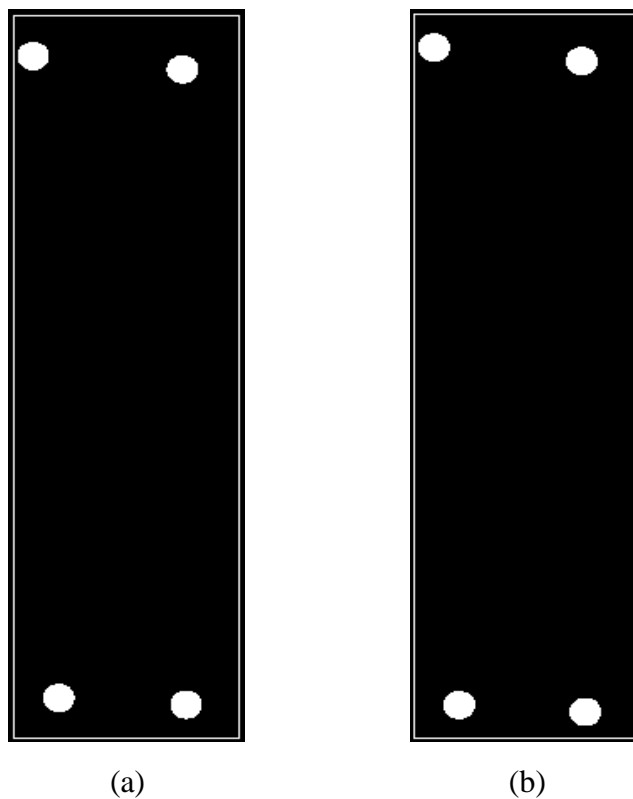


Fig. 3.18 Images with white dots created by AutoCAD software
(a) Undeformed image (b) Deformed image

3.6 Preparation of the Samples and the Experimental Set-Up

In order to apply the optical strain measurement method, tensile tests were conducted by using the Universal Testing Machine and a series of images were captured simultaneously during the strain inducing event. For the experiment, two types of samples made of mild steel and polypropylene were tested. Mild steel was selected as the material for the metallic samples since it is easily available in the market. While for the polypropylene samples, they were fabricated in-house using the injection moulding machine. The material properties of the mild steel and the polypropylene samples are as shown in Table 3.1. Basically, all the samples that were used for the tensile tests were deposited with black paint to create the random speckles pattern effect. Therefore in the following section, the details about the preparation of the testing samples were discussed and the set-up for the tensile tests was presented.

3.6.1 Mild Steel Samples

In this study, the tensile tests for the metal samples were conducted in accordance to the ASTM E8M (Standard Test Methods for Tension Testing of Metallic Materials). By referring to the ASTM standard, the purchased mild steel flat bars were cut by the Electrical-Discharge Machining (EDM) machine according to the shape as shown in Fig. 3.19. Table 3.2 shows the dimensions of the dog-bone shape specimen used in the tensile test.

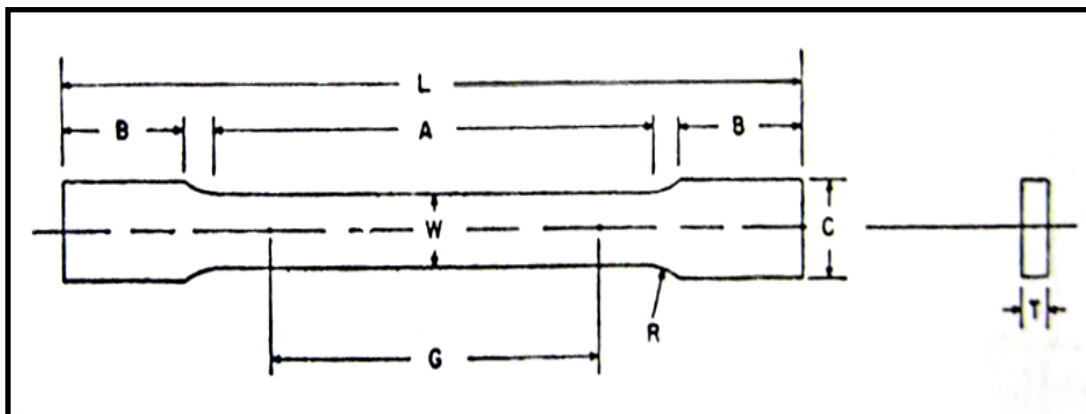


Fig. 3.19 The shape of the mild steel specimen

Table 3.2 Dimensions of the mild steel specimen

Parameters	Dimensions
G - Gauge Length	50 mm
W - Width	12.5 mm
T - Thickness	6 mm
R - Radius of fillet	65 mm
L - Overall Length	200 mm
A - Length of reduced section	57 mm
B - Length of grip section	50 mm
C - Width of grip section	20 mm

After the mild steel specimens were cut according to the dimensions as shown in Table 3.2, a number of preparation works had been carried out to deposit the random speckles pattern on the surface of the specimen. Firstly, sandpapers were used to remove the oxidized layer on the surface of the mild steel specimens. Next, a piece of cloth was used to clean the smoothed surface as to ensure the paint to be properly adhered on the surface of the specimens. After that, black paint was sprayed evenly on top of the toothbrush bristles, followed by the use of fingers to rub against the toothbrush bristles as to create the random speckles pattern. Finally, the mild steel specimen with black random speckles pattern as shown in Fig. 3.20 was prepared.

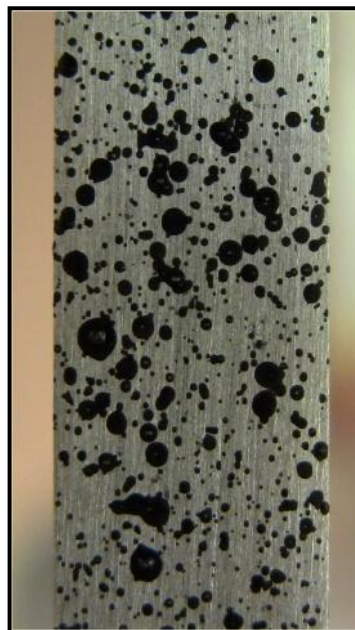


Fig. 3.20 Mild steel specimen with black random speckles pattern

3.6.2 Polypropylene Samples

For the polypropylene samples, they were fabricated in-house using the injection moulding machine which is available in Universiti Teknologi PETRONAS (UTP). Since the injection moulding machine in UTP adopted the ISO standard, the tensile tests for the plastic samples were conducted in accordance to the ISO 527-1 (Standard test method for tensile properties of plastics) instead of the ASTM D638-03 standard (both standards are technically equivalent). Fig. 3.21 shows the shape of the polypropylene samples fabricated using the injection moulding machine and Table 3.3 shows the dimensions of the dog-bone shape specimen used in the tensile test.

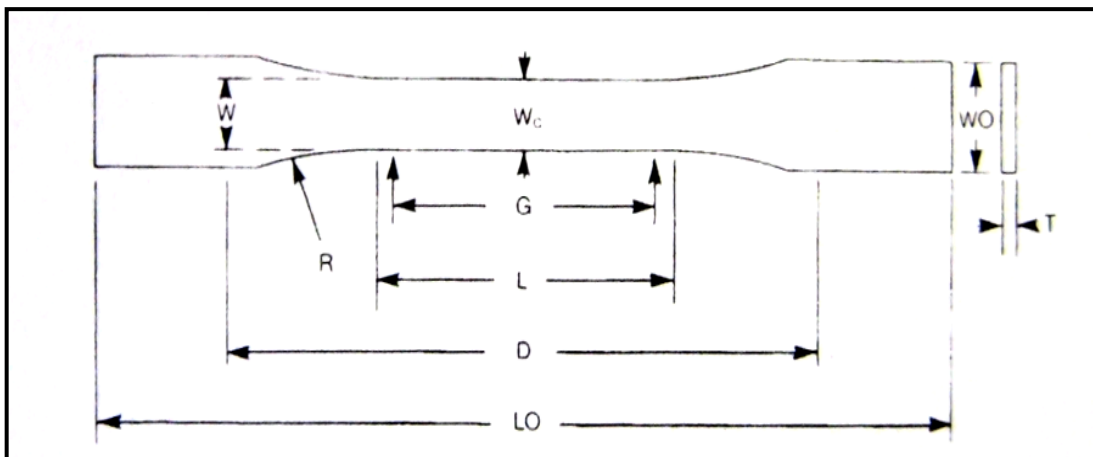


Fig. 3.21 The shape of the polypropylene specimen

Table 3.3 Dimensions of the polypropylene specimen

Parameters	Dimensions
G - Gauge Length	50 mm
W - Width of narrow section	10.2 mm
L - Length of narrow section	57 mm
WO - Overall Width	19.8 mm
LO – Overall Length	212 mm
T - Thickness	4.25 mm
R - Radius of fillet	76 mm
D - Distance between grips	115 mm

After the polypropylene specimens were fabricated by the injection moulding machine, a number of preparations works needed to be carried out in order to deposit the random speckles pattern on the surface of the specimens. Firstly, the extra channels which allowed the molten plastic to flow into the mould (runners) were cut properly. As to ensure the paint can be properly adhered on the surface of the specimens, a piece of cloth was used to clean the dust or powder on the surface of the specimens. After that, black paint was sprayed evenly on top of the toothbrush bristles, followed by the use of fingers to rub against the toothbrush bristles as to create the random speckles pattern. Finally, the polypropylene specimen with black random speckles pattern as shown in Fig. 3.22 was well prepared.

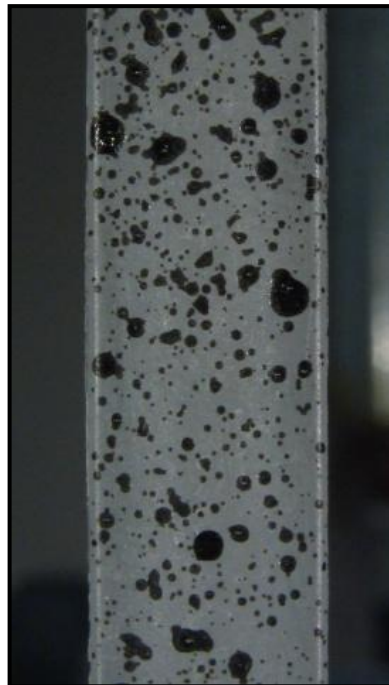


Fig. 3.22 Polypropylene specimen with black random speckles pattern

3.6.3 Experimental Set-Up

For the tensile tests in this study, the Universal Testing Machine (UTM) was used to apply the tensile load onto the specimen. At the same time, a consumer version of high-definition video camera was used to record the videos and the light sources were used to illuminate the specimen during the entire strain inducing event. Therefore, the entire experimental set-up such as the position of the video camera,

light sources and the specimens were carefully arranged before the experiment was conducted as to ensure the results with high degree of accuracy.

At the beginning of the experimental set-up, the tripod for the video camera was adjusted to the height of 140 cm from the floor. This value was selected as to compensate with the height of the grippers in the UTM, as well as the movement during the strain inducing event. After this, another two tripods for the light sources were adjusted to the height of 140 cm from the floor, which was exactly the same level as the video camera's tripod. Besides, the position of the video camera and the two light sources were fixed accordingly, so that the distance between the specimen, the video camera and the light sources remained unchanged during the entire strain inducing event. Fig. 3.23 shows the schematic diagram of the experimental set-up for the video camera, the light sources and the specimen.

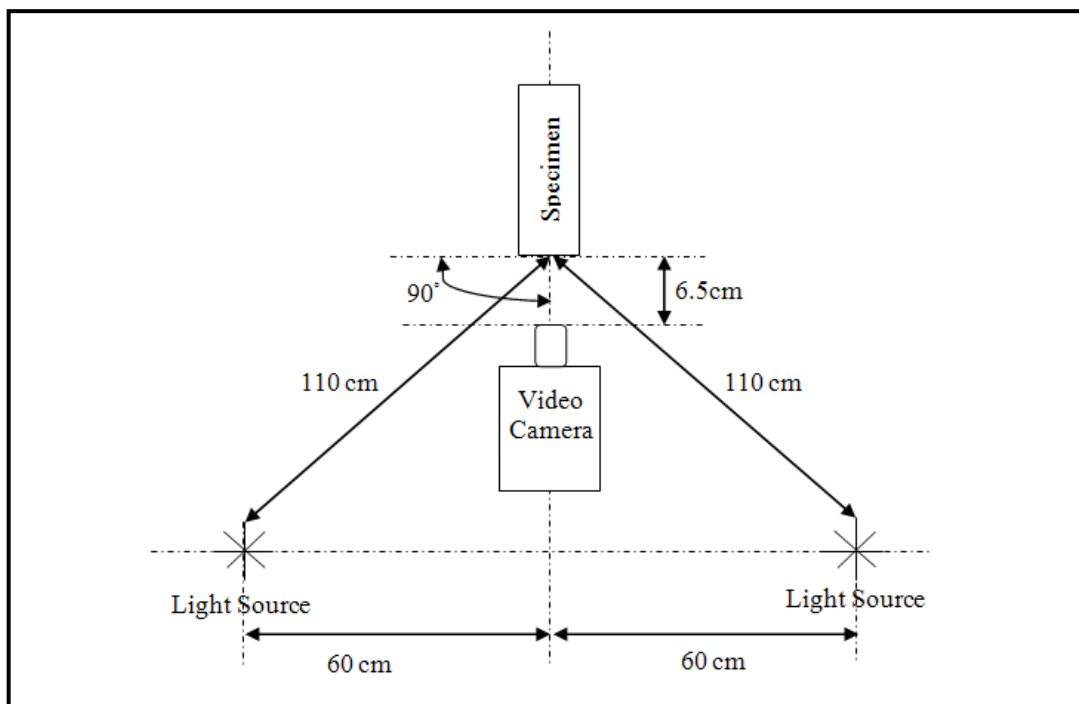


Fig. 3.23 Schematic diagram of the experimental set-up

Before the tensile test was started, it was necessary to make sure that the video camera was properly installed on top of the tripod. Since the tripod can be rotated in yaw, pitch and roll-axis, a series of alignments checking were carried out to ensure that the video camera was installed correctly. Firstly, the spirit level was placed on the body of the video camera and the alignments were adjusted to be flat in the axis of pitch and roll. At the same time, the right angle between the video camera and the

specimen as shown in Fig. 3.23 was checked by installing a mirror in the middle of the UTM grippers. By referring to the reflected image captured by the video camera as shown in Fig. 3.24, the right angle between the video camera and the specimen was achieved if the centre of the video camera's lens coincided with the cross mark generated in the video camera screen. Surprisingly, this method was found to be extremely sensitive in detecting the out-of-plane displacement. Besides this, the specimen was vertically aligned too during the installation of the specimen into the middle of the UTM grippers. A spirit level was placed alongside the dog-bone shape specimen and the alignment of the specimen in the vertical axis was verified.



Fig. 3.24 Mirror image used to prevent out-of-plane displacement

After the alignments checking were done in the experimental set-up, all the equipment such as the UTM grippers, the tripod, the video camera and the light sources were kept unchanged for the entire tensile test. Furthermore, the experimental set-up discussed above is suitable to be applied for the mild steel and the polypropylene specimens respectively.

3.7 Performing the Tensile Test and Recording of the Videos during the Strain Inducing Event

According to ASTM E8M and ISO 527-1, at least five specimens each for mild steel and polypropylene were tested using the Universal Testing Machine. At the beginning of the tensile test, the respective specimens were carefully installed into the Universal Testing Machine (UTM) grippers. Next, the extensometer was gently mounted on the specimen and the results obtained served as a benchmark for values determined from the optical strain measurement method. After this, the UTM was switched on and the cross-head speed was set to the rate of 0.02 mm/s [78]. Meanwhile, the video camera and the light sources were adjusted according to the types of the testing specimens as shown in Table 3.4. For example, the light sources were turned off during the tensile tests for the mild steel specimens as the metallic surfaces reflected the light and caused over exposure to the recorded videos. As a result, the aperture of the video camera was set to F2.0 for the mild steel specimens as the light sources were turned off during the experiment. While for the polypropylene samples, the aperture was set to F8.0 as the light sources were turned on and hence less amount of light was allowed to enter into the imaging sensor.

Table 3.4 Settings for the video camera and the light sources

Settings	Mild Steel	Polypropylene
Aperture	F2.0	F8.0
Light Sources	Off	On
Frame Rate	25 fps	25 fps
Image Resolution	1920 × 1080	1920 × 1080

The tensile test was conducted once the specimen and the extensometer were properly installed. Simultaneously, the videos were recorded using a consumer version of high-definition video camera at the rate of 25 fps. The videos recording were stopped once the necking occurred in the specimens or when the elongation is about to exceed the extensometer's measuring range. As a result, the average duration of the recorded videos was 14 minutes for the mild steel specimen and 12 minutes for the polypropylene specimen. Fig. 3.25 shows all the equipment used

in the tensile test such as the specimen, the extensometer, video camera, light sources and so on.

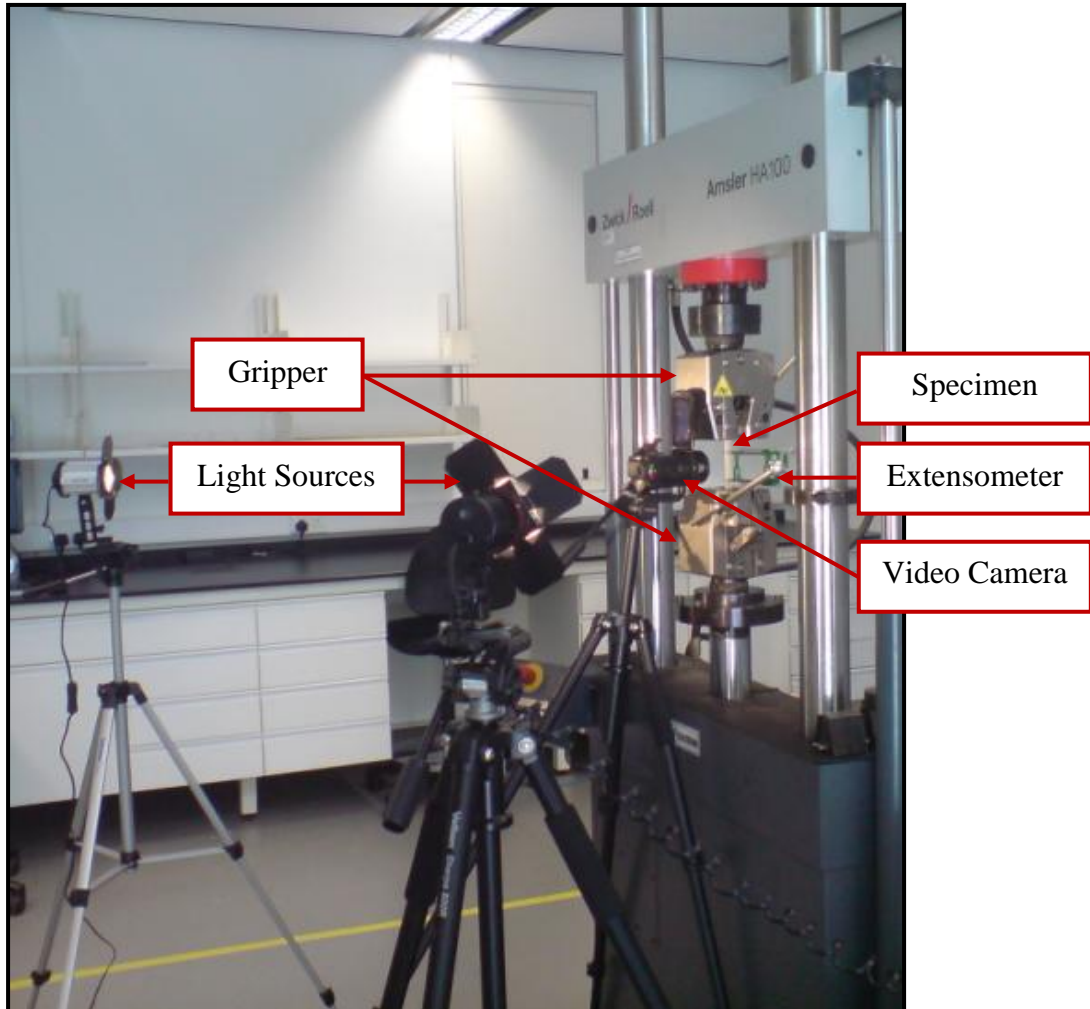


Fig. 3.25 The equipment used in the tensile test

3.8 Validation of the Optical Strain Measurement Method with the Experimental Results

First, the elongation values determined by the extensometer were extracted from the data logger of the Universal Testing Machine (UTM). By using the elongation values shown in Fig. 3.26, the strain values were then calculated and the obtained results served as a benchmark for values determined by the optical strain measurement method. Based on the data shown in Fig. 3.26, the stresses experienced by the specimen during the tensile test were determined and the modulus of elasticity of the specimen was then obtained by utilizing the stress-strain relationship.

	A	B	C	D	E	F	G
1	Logged Data File						
2	-----						
3							
4	Date	Time	Load (kN)	Stroke (mm)	Ext. (mm)		
5	07.10.2010	16:05:14	0.013	0.023	0.002		
6	07.10.2010	16:05:15	0.02	0.045	0.003		
7	07.10.2010	16:05:16	0.027	0.067	0.004		
8	07.10.2010	16:05:17	0.034	0.087	0.005		
9	07.10.2010	16:05:18	0.04	0.108	0.006		
10	07.10.2010	16:05:19	0.047	0.129	0.006		
11	07.10.2010	16:05:20	0.053	0.151	0.007		
12	07.10.2010	16:05:21	0.059	0.171	0.008		
13	07.10.2010	16:05:22	0.064	0.192	0.009		
14	07.10.2010	16:05:23	0.071	0.213	0.01		
15	07.10.2010	16:05:24	0.076	0.235	0.011		
16	07.10.2010	16:05:25	0.082	0.256	0.012		
17	07.10.2010	16:05:26	0.088	0.278	0.013		
18	07.10.2010	16:05:27	0.094	0.3	0.013		
19	07.10.2010	16:05:29	0.099	0.321	0.014		
20	07.10.2010	16:05:30	0.105	0.341	0.015		
21	07.10.2010	16:05:31	0.111	0.364	0.016		
22	07.10.2010	16:05:32	0.117	0.385	0.017		
23	07.10.2010	16:05:33	0.123	0.405	0.018		
24	07.10.2010	16:05:34	0.129	0.427	0.019		
25	07.10.2010	16:05:35	0.136	0.449	0.02		
26	07.10.2010	16:05:36	0.142	0.472	0.021		
27	07.10.2010	16:05:37	0.148	0.494	0.022		
28	07.10.2010	16:05:38	0.155	0.516	0.023		
29	07.10.2010	16:05:39	0.161	0.538	0.024		
30	07.10.2010	16:05:41	0.168	0.561	0.025		
31	07.10.2010	16:05:42	0.175	0.582	0.026		

Fig. 3.26 Elongation values extracted from the data logger

While for the experimental results, the recorded videos were first processed using the video camera before it was transferred to the computer. Since the MATLAB program was designed to execute the two images that are acquired at two different states, one before deformation and the other one after deformation, a series of images were extracted from the recorded videos. By using the built-in function in the video camera, *Capturing Photos from Video*, a series of images with the image resolution of 1920×1080 pixels were captured from the recorded videos. For example, the undeformed images were extracted at the beginning of the recorded video when time, T is equal to zero, followed by the rest of the deformed images with the time interval of 12 seconds. As a result, around 70 images were extracted from the mild steel experimental video. While for the tensile tests of the polypropylene specimen, around 60 images were extracted from the 12 minutes recorded video.

By using the consumer version of high-definition video camera, more than 650 pairs of images that were acquired at the undeformed and the deformed states were extracted from the recorded videos. These extracted images were then executed by using MATLAB program and the two-dimensional deformation measurement such as the normal strains, ϵ_{xx} and ϵ_{yy} and the shear strain, ϵ_{xy} were determined. From the determined results, only the normal strain, ϵ_{yy} was selected and compared with the benchmark values as the extensometer only provides the normal strain values in y direction, ϵ_{yy} .

In order to validate the optical strain measurement method with the experimental results, the typical stress-strain curves were plotted for the mild steel and the polypropylene samples. From the stress-strain curves, the results obtained by the optical strain measurement method and the extensometer were compared and the deviations observed from the two methods were discussed in detail. Besides, the modulus of elasticity of the mild steel and the polypropylene samples were determined by further analyzing the stress-strain curves within the elastic region. Since the elastic limit of the samples only occupied a small region in a stress-strain curve, another set of images were captured from the videos with the time interval of 4 seconds instead of 12 seconds which was applied earlier. As a result, around 25 pairs of images were extracted within the elastic region and the modulus of elasticity of the samples was successfully determined. Lastly, the modulus of elasticity of the samples determined by the optical strain measurement method and the extensometer were compared and the deviation in terms of percentage was presented.

3.9 Chapter Summary

In this chapter, the research methodology for this study was discussed in detail. At the beginning of this study, the Geometric Approach equation was validated by ANSYS simulation models as to prove its suitability or accuracy in the deformation measurement using Digital Image Correlation technique. A total of four structural components had been created in ANSYS and these models were subjected to the

tensile test simulation. During the post-processing phase in ANSYS, the strain values within the elastic limit were obtained and the Cartesian coordinates of the respective nodes in the deformed and the undeformed models were extracted. Next, the extracted nodes' Cartesian coordinates were entered in the Microsoft Excel spreadsheet where the Geometric Approach equation was embedded and the strains values were determined successfully. By comparing the results determined by the ANSYS and the Microsoft Excel spreadsheet, the Geometric Approach equation was validated as the deviations between the two methods were found to be very small.

Next, the development of the strain measurement algorithms was revealed. Firstly, all the desirable tasks were divided into eight main parts as to make sure that the algorithms can be developed separately. By using the Image Processing Toolbox in MATLAB, the respective algorithms were turned into the MATLAB program separately. Before the MATLAB program is used to analyze the images that are acquired during the strain inducing event, it is necessary to verify the optical strain measurement method with the AutoCAD images. Basically, the AutoCAD images were created using the nodes' Cartesian coordinates extracted from the ANSYS simulation model done previously. If the MATLAB program was developed correctly, it is reasonable to assume that the results determined by the optical strain measurement method are the same as the results of ANSYS simulation models.

In order to apply the MATLAB program, tensile tests were conducted and the results determined by the optical strain measurement method were validated with the benchmark values set by the extensometer. Before the tensile tests were conducted, the preparation of the mild steel and the polypropylene samples were carried out in order to deposit the black paint on the surface of the specimens. Besides, the experimental set-up such as the video camera, the light sources and the specimens were carefully arranged in order to ensure the results with high degree of accuracy. After that, the tensile test was conducted once the specimen and the extensometer were properly installed. Simultaneously, the videos were recorded using a consumer version of high-definition video camera at the rate of 25 fps and the light sources were used to illuminate the specimen during the entire strain inducing event. By referring to ASTM E8M and ISO 527-1, at least five specimens each for mild steel and polypropylene were tested during the tensile test.

Before the validation of the optical strain measurement method with the experimental results was carried out, the elongation values determined by the extensometer were extracted from the UTM's data logger. By using the elongation values found, the strain values were then calculated and the obtained results served as a benchmark values. At the same time, the stresses experienced by the specimen during the tensile tests were determined and the modulus of elasticity of the specimen was then obtained by utilizing the stress-strain relationship. While for the experimental results, the recorded videos were firstly processed using the video camera before it was transferred to the computer. Since the MATLAB program was designed to analyze the two images that are acquired at two different states, a series of images were extracted from the recorded videos. These extracted images were then analyzed by using the optical strain measurement method and the two-dimensional deformation measurement such as the normal strains, ϵ_{xx} and ϵ_{yy} and the shear strain, ϵ_{xy} were determined.

In order to validate the optical strain measurement method with the experimental results, the typical stress-strain curves were plotted for the mild steel and the polypropylene samples. From the stress-strain curves, the results obtained by the optical strain measurement method and the extensometer were compared and the deviations observed from the two methods were discussed in detail. Besides, the modulus of elasticity of the mild steel and the polypropylene samples were determined by further analyzing the stress-strain curves within the elastic region. Lastly, the modulus of elasticity of the samples determined by the optical strain measurement method and the extensometer were compared and the deviation in terms of percentage was presented.

CHAPTER 4

RESULTS AND DISCUSSIONS

4.1 Chapter Overview

In this chapter, a series of validation works have been carried out in order to verify the Geometric Approach equation and the optical strain measurement method used in this study. Results determined by the ANSYS simulation models and the analytical calculations in Microsoft Excel spreadsheet, the benchmark values of the extensometer and the optical strain measurement method were presented. Besides, the deviations observed during the validation of the Geometric Approach equation and the optical strain measurement method was discussed in detail. For example, the deviations in terms of percentage for the validation of the Geometric Approach equation were presented in the table form. While for the validation of the optical strain measurement method, the results determined by the MATLAB program and the extensometer were compared to each other. In addition, the typical stress-strain curves were plotted in order to show the agreement of the results determined by the two methods mentioned above.

4.2 Validation of the Geometric Approach Equation

In order to validate the Geometric Approach equation, a total of four bar models had been created in ANSYS. Two models represented the mild steel samples and the other two represented the polypropylene samples. The tensile test simulations have been carried out on these two-dimensional and three-dimensional models. Using the Post-Processing command in ANSYS, *Contour Plot*, the normal strains and the shear strains of the mild steel and the polypropylene models within the elastic limit were determined successfully.

At the same time, a total of four calculations were performed in the Microsoft Excel spreadsheet where the Geometric Approach equation was embedded. Two calculations each for the mild steel and the polypropylene models in two-dimension and three-dimension were performed. By using the Cartesian coordinates of the nodes extracted from the ANSYS models above, the strain values of the bar models were calculated using the Microsoft Excel spreadsheet. Table 4.1 and Table 4.2 show the comparison of the normal strains values for the two-dimensional and the three-dimensional models respectively. The shear strains in xy , xz and yz -plane will not be discussed here as the values found are negligible if compared to the normal strain values.

Table 4.1 Comparison of the strain values for two-dimensional models

Materials	Type of Loading: Displacement	Strain	ANSYS Simulation Models	Geometric Approach Equation	Deviation (%)
Mild Steel	$-U_y = 0.039$ mm (applied on the bottom face of the bar models)	ϵ_{xx}	-0.0004680	-0.0004679	0.02
		ϵ_{yy}	0.0015600	0.0015612	0.08
Polypropylene	$-U_y = 0.56$ mm (applied on the bottom face of the bar models)	ϵ_{xx}	-0.0082880	-0.0082540	0.41
		ϵ_{yy}	0.0224000	0.0226500	1.12

Table 4.2 Comparison of the strain values for three-dimensional models

Materials	Type of Loading: Displacement	Strain	ANSYS Simulation Models	Geometric Approach Equation	Deviation (%)
Mild Steel	$-U_y = 0.039$ mm (applied on the bottom face of the bar models)	ϵ_{xx}	-0.0004680	-0.0004679	0.02
		ϵ_{yy}	0.0015600	0.0015612	0.08
		ϵ_{zz}	-0.0004680	-0.0004679	0.02
Polypropylene	$-U_y = 0.56$ mm (applied on the bottom face of the bar models)	ϵ_{xx}	-0.0082880	-0.0082540	0.41
		ϵ_{yy}	0.0224000	0.0226500	1.12
		ϵ_{zz}	-0.0082880	-0.0082540	0.41

For the validation of the Geometric Approach equation, the results determined by the ANSYS were set as the benchmark for the values calculated by Microsoft Excel spreadsheet where the Geometric Approach equation was embedded. By referring to Table 4.1 and Table 4.2, the deviations of the Geometric Approach equation were found to be less than 0.10% for mild steel models. For example, the deviations of the two-dimensional model were 0.02% and 0.08% for ε_{xx} and ε_{yy} respectively. While for the three-dimensional model, the deviations were 0.02% for ε_{xx} , 0.08% for ε_{yy} and 0.02% for ε_{zz} . However, for the polypropylene models, the deviations of the two-dimensional model were 0.41% and 1.12% for ε_{xx} and ε_{yy} respectively. While for the three-dimensional model, the deviations were 0.41% for ε_{xx} , 1.12% for ε_{yy} and 0.41% for ε_{zz} .

By analyzing further the results determined by the analytical calculations, the term on the left hand side of eq. 3.1 was found to be the sole factor that contributes to the small deviations during the validation of the Geometric Approach equation. This can be explained by using an example where the orientations of the line element, $\theta_y = \theta_z = \frac{\pi}{2}$ and $\theta_x = 0$. Eq. 3.1 was then reduced to

$$\frac{1}{2}\varepsilon^2 + \varepsilon = \varepsilon_{xx} \quad (4.1)$$

where ε is the relative change in distance between the two nodes and ε_{xx} is the normal strain of the line element parallel to the x -axis. Based on eq. 4.1, if the relative change in distance between the two nodes, ε is relatively small, the normal strain, ε_{xx} is the same as the relative change in distance between the two nodes, ε . This is because the term $\frac{\varepsilon^2}{2}$ becomes negligible if compared to the relative change in distance between the two nodes, ε [79]. However, the term $\frac{\varepsilon^2}{2}$ still contributes a small value to the left hand side of eq. 4.1. For example, by referring to Fig. 4.1 shown below, the relative change in distance between the second and the fourth selected nodes was equal to 0.0224. Since the orientations of the line element between the first and the second nodes were $\cos \theta_x = 0$, $\cos \theta_y = 1$, $\cos \theta_z = 0$ (line

element is parallel to the y-axis), the normal strain, ϵ_{yy} should be 0.0224 instead of 0.02265 which was determined by the Geometric Approach equation. This variation was because the term $\frac{\epsilon^2}{2}$ contributes a small value, 0.00025 to the left hand side of eq. 4.1 which resulted the deviation of 1.12% for the normal strain, ϵ_{yy} .

Basically, all the deviations as shown in Table 4.1 and Table 4.2 occurred as the term $\frac{\epsilon^2}{2}$ contributes a small value even though it was treated as negligible when the relative change in distance between the two nodes, ϵ was small. Nevertheless, by referring to the percentage of deviations as shown above, the strain values determined by the ANSYS and the analytical calculations were still extremely close to each other. As a result, it can be concluded that the Geometric Approach equation was accurate enough for this study.

Before Deformation				After Deformation			
Node number	Cartesian Coordinate			Node number	Cartesian Coordinate		
	x (mm)	y (mm)	z (mm)		x (mm)	y (mm)	z (mm)
1106	0.971429	11	0	1106	1.005647	10.6864	0.017612
1119	4.128571	11	0	1119	4.136622	10.6864	0.017612
1346	0.971429	14	0	1346	1.005647	13.7536	0.017612
1359	4.128571	14	0	1359	4.136622	13.7536	0.017612
2805	0.971429	11	2.125	2805	1.005647	10.6864	2.125
2817	0.971429	14	2.125	2817	1.005647	13.7536	2.125
4092	4.128571	11	2.125	4092	4.136622	10.6864	2.125

$\Delta S_1 =$	3.157142	$\Delta S_1^* =$	3.130975
$\Delta S_2 =$	4.3551746	$\Delta S_2^* =$	4.383004
$\Delta S_3 =$	3	$\Delta S_3^* =$	3.0672
$\Delta S_4 =$	3.8056761	$\Delta S_4^* =$	3.774134
$\Delta S_5 =$	4.8459437	$\Delta S_5^* =$	4.863312
$\Delta S_6 =$	2.125	$\Delta S_6^* =$	2.107388

Strain 1 =	-0.0082882
Strain 2 =	0.0063899
Strain 3 =	0.0224
Strain 4 =	-0.0082881
Strain 5 =	0.0035841
Strain 6 =	-0.008288

Relative change in distance between the second and fourth selected nodes, strain₂₄ = 0.0224

$\cos \theta_{1,2} =$	-1	$\cos \theta_{1,2} =$	0	$\cos \theta_{1,2} =$	0
$\cos \theta_{1,3} =$	0	$\cos \theta_{1,3} =$	1	$\cos \theta_{1,3} =$	0
$\cos \theta_{1,4} =$	-0.8295877	$\cos \theta_{1,4} =$	0	$\cos \theta_{1,4} =$	0.558376
$\cos \theta_{1,5} =$	-0.651502	$\cos \theta_{1,5} =$	0.61907	$\cos \theta_{1,5} =$	0.438511
$\cos \theta_{1,6} =$	0	$\cos \theta_{1,6} =$	0	$\cos \theta_{1,6} =$	1

Orientations of the line element between the 2nd and 4th nodes in the undeformed image, $\cos \theta_x = 0$, $\cos \theta_y = 1$, $\cos \theta_z = 0$

Equation 1 :	-0.0082538	=	1	ϵ_{xx}	+	0	ϵ_{yy}	+	0	ϵ_{zz}	+	0	ϵ_{xy}	+	0	ϵ_{yz}	+	0	ϵ_{xz}
Equation 2 :	0.0064103	=	0.5255053	ϵ_{xx}	+	0.47449	ϵ_{yy}	+	0	ϵ_{zz}	+	-0.998698	ϵ_{xy}	+	0	ϵ_{yz}	+	0	ϵ_{xz}
Equation 3 :	0.0226509	=	0	ϵ_{xx}	+	1	ϵ_{yy}	+	0	ϵ_{zz}	+	0	ϵ_{xy}	+	0	ϵ_{yz}	+	0	ϵ_{xz}
Equation 4 :	-0.0082538	=	0.6882157	ϵ_{xx}	+	0	ϵ_{yy}	+	0.311784	ϵ_{zz}	+	0	ϵ_{xy}	+	-0.92644	ϵ_{yz}	+	0	ϵ_{xz}
Equation 5 :	0.0035905	=	0.4244548	ϵ_{xx}	+	0.38325	ϵ_{yy}	+	0.192292	ϵ_{zz}	+	-0.806656	ϵ_{xy}	+	-0.57138	ϵ_{yz}	+	0.542942	ϵ_{xz}
Equation 6 :	-0.0082537	=	0	ϵ_{xx}	+	0	ϵ_{yy}	+	1	ϵ_{zz}	+	0	ϵ_{xy}	+	0	ϵ_{yz}	+	0	ϵ_{xz}

From the equation 3, 0.02265 = ϵ_{yy}

Geo. Approach (Excel):	$\epsilon_{xx} =$	-0.008254
	$\epsilon_{yy} =$	0.02265
	$\epsilon_{zz} =$	-0.008254
	$\epsilon_{xy} =$	3.37E-08
	$\epsilon_{yz} =$	3.365E-08
	$\epsilon_{xz} =$	8.143E-08

Fig. 4.1 The embedded Geometric Approach equation in the Microsoft Excel spreadsheet

4.3 Verification of the Optical Strain Measurement Method with AutoCAD Images

By using the nodes' Cartesian coordinates extracted from the ANSYS simulation models previously, two sets of images with white dots (to represent the speckles) were created in AutoCAD software. These images were created under two different states, one before deformation and the other one after deformation. In order to verify the optical strain measurement method, the AutoCAD images were read and analyzed by using the MATLAB program. Since the Cartesian coordinates of the respective nodes were extracted from the ANSYS simulation models, it was reasonable to assume that the results determined using the optical strain measurement method should be the same as the ANSYS simulation models.

Table 4.3 Verification of the optical strain measurement method

Materials	Strain	ANSYS Simulation Models	Optical Strain Measurement Method	Deviation (%)
Mild Steel	ϵ_{xx}	-0.0004680	-0.0004903	4.76
	ϵ_{yy}	0.0015600	0.0016151	3.53
Polypropylene	ϵ_{xx}	-0.0082880	-0.0084106	1.48
	ϵ_{yy}	0.0224000	0.0226510	1.12

In the verification of the optical strain measurement method, the results determined by ANSYS served as the benchmark values. By referring to Table 4.3, the deviations for the results determined by optical strain measurement method were less than 5%. For example, the deviations of the mild steel models were found to be 4.76% and 3.53% for ϵ_{xx} and ϵ_{yy} respectively. While for the polypropylene models, the deviations between the results determined by ANSYS and optical strain measurement method were found to be 1.48% for ϵ_{xx} and 1.12% for ϵ_{yy} .

Based on the deviations shown above, it proved that the optical strain measurement method was able to analyze the two images that were created under two different states smoothly and was also able to determine the strain values successfully. However, the deviations that occurred during the comparison between the results determined by the ANSYS and the optical strain measurement method

were mainly due to the image resolution of the AutoCAD images. Since all of these images were created and exported from the AutoCAD software, the output images were low in terms of the image resolution. For example, all the output images from the AutoCAD software in this study were around 9 pixels/mm (depending on the size of the object created).

Basically, these deviations can be further reduced by increasing the image resolution of the output images. However, the results will not be presented here as the main concern for the verification of the optical strain measurement method was to prove its capability in the determination of the deformation measurement. Lastly according to the results shown in Table 4.3, the optical strain measurement method was precise enough to determine the displacement of the speckles and hence compute the strain values accurately.

4.4 Validation of the Optical Strain Measurement Method with the Experimental Results

In order to apply the MATLAB program, tensile tests were conducted and the results determined by the optical strain measurement method were validated with the benchmark values set by the extensometer. By using the Universal Testing Machine (UTM), two types of samples made of mild steel and polypropylene materials were tested. At the same time, videos were recorded at the beginning of the strain-inducing event using the high-definition video camera. These videos were captured continuously and stopped when necking occurred in the specimens or when the elongation is about to exceed the extensometer's measuring range.

By extracting the elongation values from the UTM's data logger (refer to Fig. 3.26), a series of calculations were performed in the Microsoft Excel spreadsheet. At the same time, the extracted images from the recorded videos were then analyzed using the MATLAB program and the two-dimensional deformation measurement were determined. All the necessary information of the tensile tests were recorded and used for the calculation of important properties as shown in the Microsoft Excel spreadsheet as in Fig.4.2. For example, the duration of the tensile

tests was recorded, the stress and the strain experienced by the specimen at the specific time interval were calculated and the modulus of elasticity for each of the specimens was determined. In addition, the results determined by the extensometer and the optical strain measurement method were compared to each other and the deviations between the two methods were obtained.

	A	B	C	D	E	F	G	H	I	J	K	L	M	N	O	P
1	Logged Data File															
2	Stress=F/A															
3	A= 0.04335															
4	Date	Time	Ori Time	Load (kN)	Stroke (mm)	Ext. (mm)	Ext.*4.932	Duration	Stress (MPa)	Strain	Strain (Mat.)	Dev. (%)	MOE (GPa)	ϵ_{xx}	ϵ_{yy}	Poisson's Rat.
74	08.10.2010	15:09:30	15:08:18	0.412	1.415	0.06	0.29592	0:01:12	9.5040369	0.0059184	0.0067236	13.60503	1.605845652	-0.002095	-0.000529	0.31161878
75	08.10.2010	15:09:32	15:08:18	0.419	1.437	0.061	0.30085	0:01:14	9.6655133	0.00601704			1.606356824			
76	08.10.2010	15:09:33	15:08:18	0.425	1.458	0.062	0.30578	0:01:15	9.8039216	0.00611568			1.603079554			
77	08.10.2010	15:09:34	15:08:18	0.433	1.478	0.064	0.31565	0:01:16	9.988466	0.00631296	0.0068456	8.437247	1.582215945	-0.002277	-0.001443	-0.33257859
78	08.10.2010	15:09:35	15:08:18	0.44	1.499	0.065	0.32058	0:01:17	10.149942	0.0064116			1.583059194			
79	08.10.2010	15:09:36	15:08:18	0.448	1.52	0.066	0.32551	0:01:18	10.334487	0.00651024			1.587420239			
80	08.10.2010	15:09:37	15:08:18	0.455	1.542	0.068	0.33538	0:01:19	10.495963	0.00670752			1.564805337			
81	08.10.2010	15:09:38	15:08:18	0.462	1.563	0.069	0.34031	0:01:20	10.657439	0.00680616	0.0077291	13.56036	1.565852029	-0.002106	-0.000594	-0.2725285
82	08.10.2010	15:09:39	15:08:18	0.469	1.584	0.07	0.34524	0:01:21	10.818916	0.0069048			1.566868816			
83	08.10.2010	15:09:40	15:08:18	0.476	1.605	0.071	0.35017	0:01:22	10.980392	0.00700344			1.567856961			
84	08.10.2010	15:09:41	15:08:18	0.483	1.627	0.073	0.36004	0:01:23	11.141869	0.00720072			1.547327005			
85	08.10.2010	15:09:42	15:08:18	0.491	1.648	0.074	0.36497	0:01:24	11.326413	0.00729936	0.0073716	0.989676	1.551699453	-0.00289	9.80E-06	0.39197732
86	08.10.2010	15:09:43	15:08:18	0.497	1.669	0.076	0.37483	0:01:25	11.464821	0.00749664			1.529327969			
87	08.10.2010	15:09:44	15:08:18	0.504	1.69	0.077	0.37976	0:01:26	11.626298	0.00759528			1.530726659			
88	08.10.2010	15:09:45	15:08:18	0.511	1.71	0.078	0.3847	0:01:27	11.787774	0.00769392			1.532089485			
89	08.10.2010	15:09:46	15:08:18	0.517	1.732	0.08	0.39456	0:01:28	11.926182	0.0078912	0.0080242	1.685422	1.511326825	-0.002268	-0.000236	-0.28266992
90	08.10.2010	15:09:47	15:08:18	0.525	1.754	0.081	0.39949	0:01:29	12.110727	0.00798984			1.515765853			
91	08.10.2010	15:09:48	15:08:18	0.532	1.775	0.082	0.40442	0:01:30	12.272203	0.00808848			1.517244649			
92	08.10.2010	15:09:49	15:08:18	0.539	1.795	0.084	0.41429	0:01:31	12.433679	0.00828576			1.500608195			
93	08.10.2010	15:09:50	15:08:18	0.542	1.805	0.084	0.41429	0:01:32	12.502884	0.00828576	0.0082341	0.623479	1.508960374	-0.002937	-0.000113	-0.35671172
94	08.10.2010	15:09:51	15:08:18	0.546	1.816	0.085	0.41922	0:01:33	12.595156	0.0083844			1.502213123			
95	08.10.2010	15:09:52	15:08:18	0.553	1.838	0.087	0.42908	0:01:34	12.756632	0.00858168			1.486495892			
96	08.10.2010	15:09:53	15:08:18	0.559	1.859	0.088	0.43402	0:01:35	12.89504	0.00868032			1.485548962			
97	08.10.2010	15:09:54	15:08:18	0.566	1.88	0.09	0.44388	0:01:36	13.056517	0.0088776	0.008559	3.588808	1.470725993	-0.002689	-0.000471	0.31419558
98	08.10.2010	15:09:55	15:08:18	0.572	1.9	0.091	0.44881	0:01:37	13.194925	0.00897624			1.469983538			
99	08.10.2010	15:09:56	15:08:18	0.581	1.929	0.093	0.45868	0:01:38	13.402537	0.00917352			1.4610027			
100	08.10.2010	15:09:57	15:08:18	0.589	1.952	0.094	0.46361	0:01:39	13.587082	0.00927216			1.465363183			
101	08.10.2010	15:09:58	15:08:18	0.596	1.973	0.096	0.47347	0:01:40	13.748558	0.00946944	0.0098595	4.119145	1.451887149	-0.003457	-0.000981	-0.35064658
102	08.10.2010	15:09:59	15:08:18	0.602	1.995	0.097	0.4784	0:01:41	13.886967	0.00956808			1.45138487			

Fig. 4.2 Calculation of the important properties from the tensile test data in Microsoft Excel spreadsheet

By using the strain values determined by the extensometer, the stress-strain curves were plotted for the mild steel and the polypropylene specimens respectively. At the same time, the strain-strain curves of the optical strain measurement method were plotted and compared with the benchmark values set by the extensometer. The details about the deviations between the results determined by the two methods were discussed in the following section. In general, the shape of the plotted stress-strain curves was found to be exactly the same as the shape of the load-elongation curves generated by UTM's data logger. This was because the stress and the strain of a specimen were determined by dividing the load and the elongation with the constant factors, i.e. the original cross sectional area and the original length of the specimens [80-81].

4.4.1 Mild Steel Specimens

In order to validate the optical strain measurement method, a stress-strain curve for the first mild steel specimen was plotted as in Fig. 4.3. Since a total of five specimens were tested during the tensile test, the remaining four stress-strain curves of the mild steel specimens were included in Appendix C. Based on Fig. 4.3, the strain values determined from the extensometer readings (solid line) served as the benchmark for the strain values determined by the optical strain measurement method (dotted points). The results for the strain values determined by the extensometer were only up to 0.18 mm/mm. This was because the extensometer was uninstalled from the specimen as the elongation is about to exceed the extensometer's measuring range.

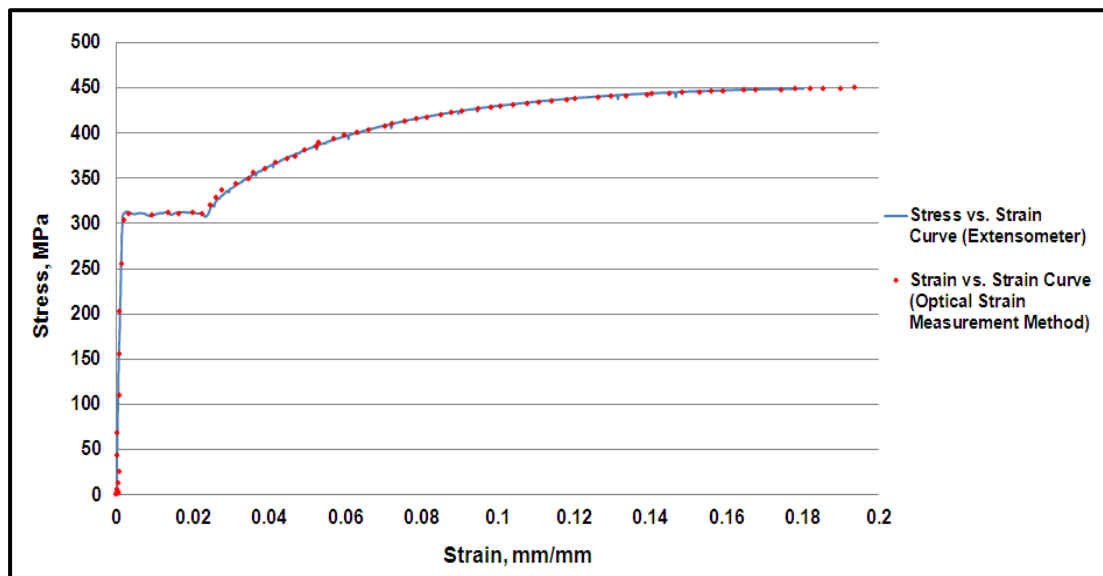


Fig. 4.3 Stress-strain curve for the mild steel specimen

By referring to Fig. 4.3, the strain values determined by the extensometer and the optical strain measurement method were close to each other. Besides, the trends for the stress-strain curves determined from the extensometer readings and the optical strain measurement method were similar and fitted together perfectly. However, some deviations were still observed at the beginning of the elastic region in the stress-strain curve. By analyzing the results determined by the optical strain measurement method, the positions of the selected speckles in the first few pairs of the captured images were barely displaced. Even though the images have the image

resolution of 68.8 pixels/mm and 65.1 pixels/mm in the x and y directions respectively, the captured images were unable to record the small displacement accurately. Besides, the results were found to be slightly fluctuating around the benchmark values when the strain values were below 0.008 mm/mm. Nevertheless, the deviations were reduced as the strain values increased.

Beyond the elastic limit, the yield point phenomenon was observed in the transition from the elastic to the plastic deformation. As shown in Fig. 4.4, the stress increased linearly in the elastic region, followed by a sudden drop at the upper yield point. Next, the stress fluctuated around a constant value (lower yield point) and then rose when the strain was approaching 0.024 mm/mm. Basically, this phenomenon occurred due to the dislocation motion in the low-carbon steel such as the one used in this study. As the small interstitial atoms in the material interfered with the dislocation slip plane, the stress was increased to the upper yield point. Once the dislocations plane started to slip, the stress was lowered to the lower yield point [82]. Besides, the Luders Bands were observed throughout the yield point elongation and these bands were approximately 45° to the tensile axis [83]. In this study, the complete yield point phenomenon was recorded by the video camera and the Luders Bands observed were shown in Fig. 4.5. In general, the stress value started to increase once the Luders Bands have propagated over the entire gauged section.

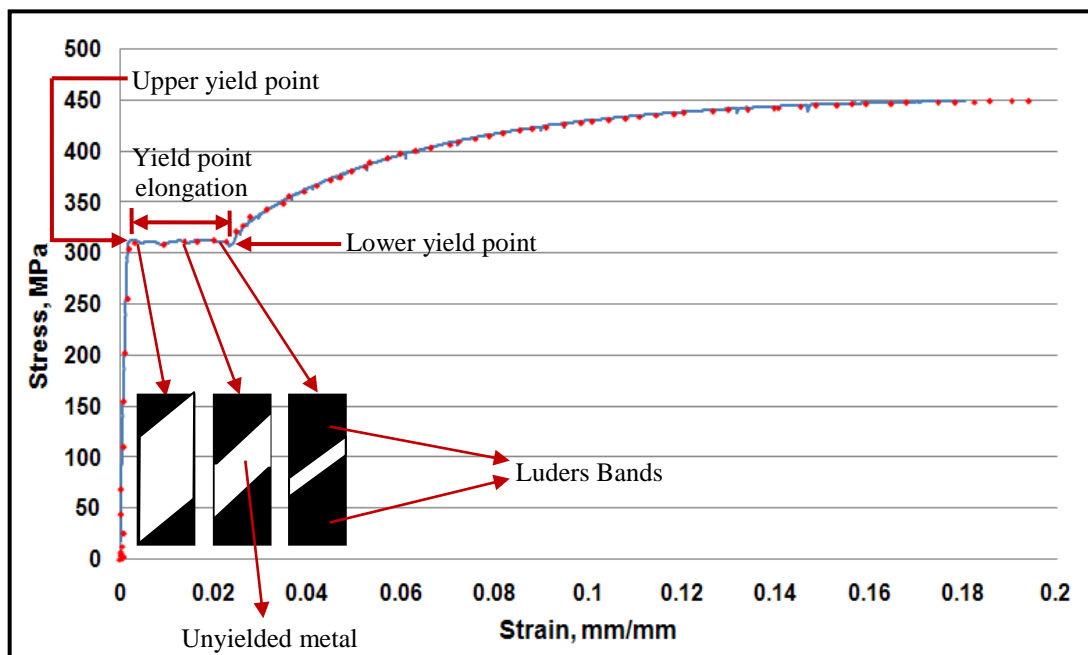


Fig. 4.4 Yield point phenomenon of the mild steel specimen

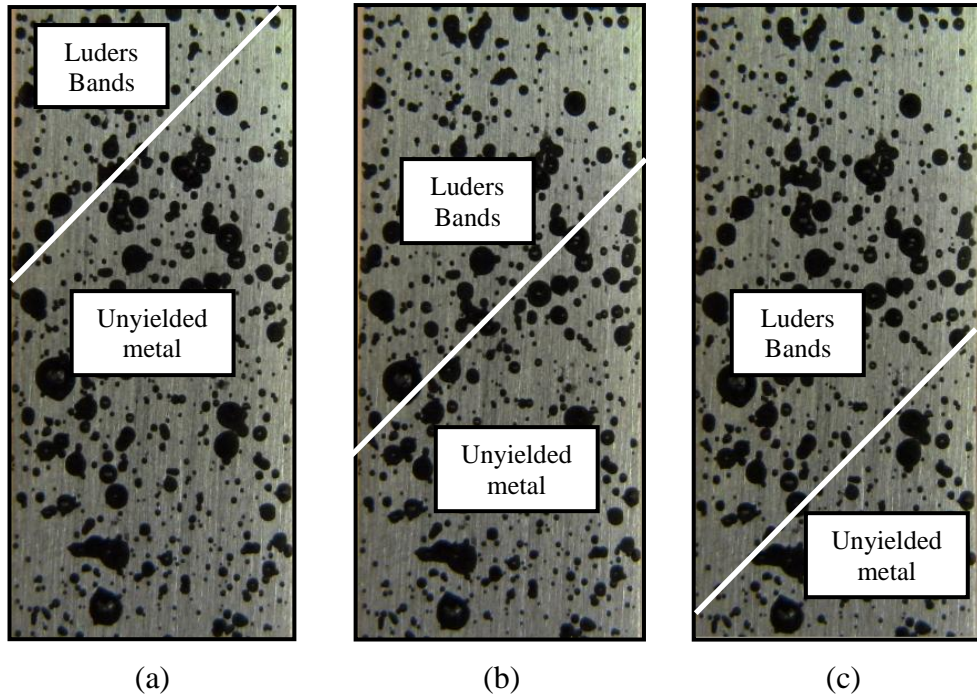


Fig. 4.5 Luders Bands observed in the captured images

- (a) Image captured when $t = 3\text{min } 36\text{s}$ (b) Image captured when $t = 3\text{min } 48\text{s}$
(c) Image captured when $t = 4\text{min } 00\text{s}$

Since the deformations that occurred throughout the yield point elongation were reported to be heterogeneous or irregular [84], the selection of the speckles during the execution of the MATLAB program was different than before. The four speckles have to be selected within the Luders Bands rather than from the random speckles pattern. This was because no deformations occurred within the unyielded metal section. Despite of the yield point phenomenon that was observed during the transition from the elastic to the plastic deformation, the optical strain measurement method was still able to determine the deformations that occurred in the specimen. Based on the results determined by the optical strain measurement method, the deviations were found to be in the range of minimum 4.80% to the maximum of 10.83% off the benchmark values.

When the strain value was about to exceed the lower yield point or to be exactly 0.024 mm/mm, the deviations between the results determined by the extensometer and the optical strain measurement method were found to be very small. For example, when the strain values determined by the extensometer were in between 0.03 mm/mm and 0.07 mm/mm, the results determined by the optical strain

measurement method were in the range of minimum 0.23% to the maximum of 2.83% off the benchmark values. Besides, the deviations of the results determined by the optical strain measurement method were less than 5% off the benchmarks values when the strain values determined by the extensometer were below 0.12 mm/mm. However, the deviations for the results determined by the extensometer and the optical strain measurement method were found to be increasing when the strain values were further increased. Based on Fig. 4.3, the results determined by the optical strain measurement method were in the range of minimum 5% to the maximum of 7.87% off the benchmark values when the strain values determined by the extensometer were in between 0.12 mm/mm and 0.18 mm/mm.

In fact, the deviations were expected as the Geometric Approach equation embedded in the MATLAB program contributed to the deviations. As described earlier in section 4.2, the Geometric Approach equation alone will contribute the deviation of 9% when the strain value is approaching 0.18 mm/mm. From the comparison of the results determined by the extensometer and the optical strain measurement method, the small deviations proved that the optical strain measurement method is capable to determine the strain values correctly. Besides, a good agreement was achieved upon comparison with the benchmark values especially when the strain values were above 0.024 mm/mm.

4.4.2 Polypropylene Specimens

In order to validate the optical strain measurement method, a total of five polypropylene specimens were also tested during the tensile test. Fig. 4.6 shows the stress-strain curve for the first polypropylene specimen. The stress-strain curves for the remaining four specimens were plotted in Appendix D. Based on Fig. 4.6, the strain values determined from the extensometer readings (solid line) served as the benchmark for the strain values determined by the optical strain measurement method (dotted points). The results for the strain values determined by the extensometer were only up to 0.16 mm/mm. This was because the necking occurred in the specimen and the extensometer was uninstalled from the specimen.

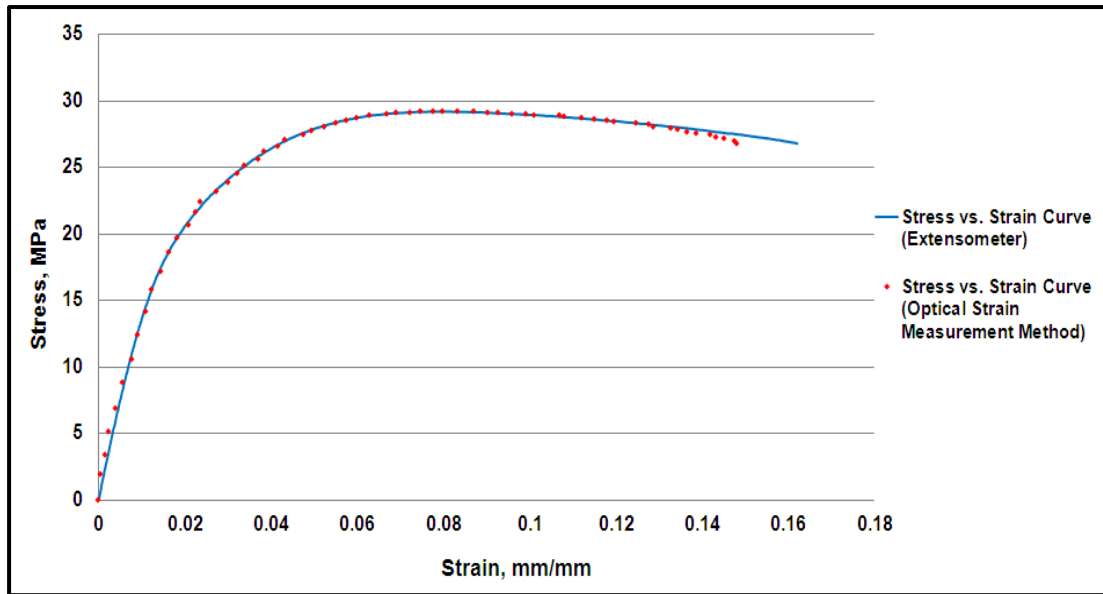


Fig. 4.6 Stress-strain curve for the polypropylene specimen

By referring to Fig. 4.6, the strain values determined by the extensometer and the optical strain measurement method were extremely close to each other. At the same time, the trends for the stress-strain curves determined from the extensometer readings and the optical strain measurement method were found to be similar. However, some deviations were observed at the beginning of the elastic region in the stress-strain curve. The deviations were small if compared to the deviations that occurred in the mild steel specimen. This was because the polypropylene material has a smaller modulus of elasticity, 1500 MPa if compared to the mild steel material, 207 GPa. The polypropylene specimens tend to elongate or deform when a smaller load was applied to the specimens. As a result, the position change of the selected speckles in the images captured within the elastic region was noticeable and the MATLAB program was able to record the displacement accurately. On the other hand, the results were found to be slightly fluctuating around the benchmark values when the strain values were below 0.008 mm/mm. Nevertheless, the deviations were reduced as the strain values increased.

When the strain values were in between 0.016 mm/mm (the elastic limit) and 0.075 mm/mm (the ultimate tensile strength point), the deviations between the results determined by the extensometer and the optical strain measurement method were found to be small. For example, the results determined by the optical strain measurement method were in the range of minimum 0.22% to the maximum of

3.63% off the benchmark values. Besides, the deviations of the results determined by the optical strain measurement method were found to be less than 5% off the benchmark values when the strain values determined by the extensometer were below 0.14 mm/mm. However, the deviations of the results determined by the two methods mentioned above were higher when the strain values were increased. By referring to Fig. 4.6, the results determined by the optical strain measurement method were in the range of minimum 5% to the maximum of 8.59% off the benchmark values when the strain values were in between 0.14 mm/mm and 0.16 mm/mm.

As described earlier in section 4.4.1, the deviation of 8% off the benchmark value was expected to occur when the strain value was approaching 0.16 mm/mm. However, by referring to Fig. 4.6 once again, the deviations that occurred were different if compared with the stress-strain curves for the mild steel specimen as shown in Fig. 4.3. As shown in Fig. 4.3, the results determined by the optical strain measurement method deviated as much as 8% more than the benchmarks values. But according to Fig. 4.6, the results determined by the optical strain measurement method were found to be 8.59% less than the benchmark values. Actually, the deviations that occurred in the polypropylene specimens were different as necking was found to be the factor which contributed to the errors. By referring to Fig. 4.7, the necking occurred in the mounting points between the extensometer and the specimen. Besides, the same necking issue was observed for the other four polypropylene specimens during the tensile tests.

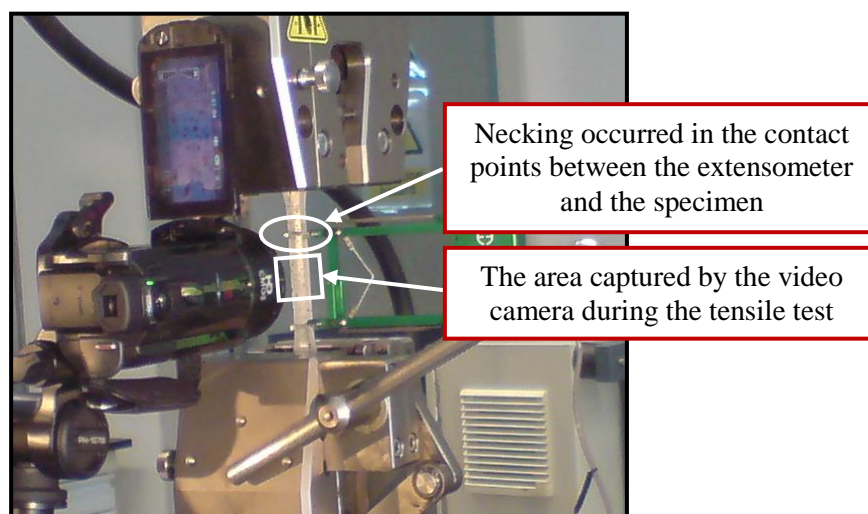


Fig. 4.7 Necking observed during the tensile test

Throughout the tensile tests for the five polypropylene specimens, the necking was observed at the same position as shown in Fig. 4.7 when the strain value determined by the extensometer was approaching 0.14 mm/mm. From this observation, it proved that the extensometer has introduced the stress concentrations on the mounting points and created premature necking to the specimens. Since the necking occurred in one of the extensometer's clips, the extensometer was still able to measure the elongation and hence compute the strain values successfully. However by referring to the stress-strain curves plotted for the five polypropylene specimens as shown in Fig. 4.6 and Appendix D, the strain values determined by the optical strain measurement method started to decrease when the benchmark value was approaching 0.14 mm/mm. This was because the video camera was set to capture the middle of the gauged section of the specimen during the tensile test. Since the elongation occurred mostly in the stress concentration area (the extensometer mounting point) and not in the middle of the gauged section, the captured images were unable to record the elongation correctly. As a result, the strain values determined by the optical strain measurement method were smaller and 8.59% off the benchmark values when the strain value was approaching 0.16 mm/mm.

From the comparison of the results determined by the extensometer and the optical strain measurement method, the small deviations proved that the optical strain measurement method was capable to determine the strain values correctly. Besides, a good agreement was achieved upon comparison with the benchmark values especially when the strain values were above 0.008 mm/mm. Although some deviations were still observed during the comparison of the results determined by the two methods mentioned above, they were within the acceptable limit. Through the comparison between the results determined by the extensometer and the optical strain measurement method, the deviations will start to increase once the necking was found to occur in the specimens.

4.4.3 Comparison of the Specimens' Material Properties

For the comparison of the specimens' material properties, the modulus of elasticity of the mild steel and the polypropylene specimens were determined by further analyzing the stress-strain curves within the elastic region. By using the results determined by the extensometer and the optical strain measurement method, the gradient of the stress-strain curves for the respective material within the elastic region were plotted. As a result, the modulus of elasticity of the respective specimens was successfully determined. The modulus of elasticity of the respective specimens determined by the two methods mentioned above was compared and the deviations in terms of percentage were shown in the following section.

4.4.3.1 Mild Steel Specimens

In order to find the modulus of elasticity of the mild steel specimens, the gradient of the stress-strain curve for the first specimen was plotted as in Fig. 4.8. Since a total of five specimens were tested during the tensile test, the remaining four gradients which represented the modulus of elasticity of the respective mild steel specimens were included in Appendix E. By referring to Fig. 4.8, the strain values determined from the extensometer readings (triangle dotted points) served as the benchmark for the strain values determined by the optical strain measurement method (diamond dotted points). Meanwhile, two straight lines which best fitted the dotted points were plotted. As a result, the modulus of elasticity of the mild steel specimen was successfully determined by the two methods mentioned above.

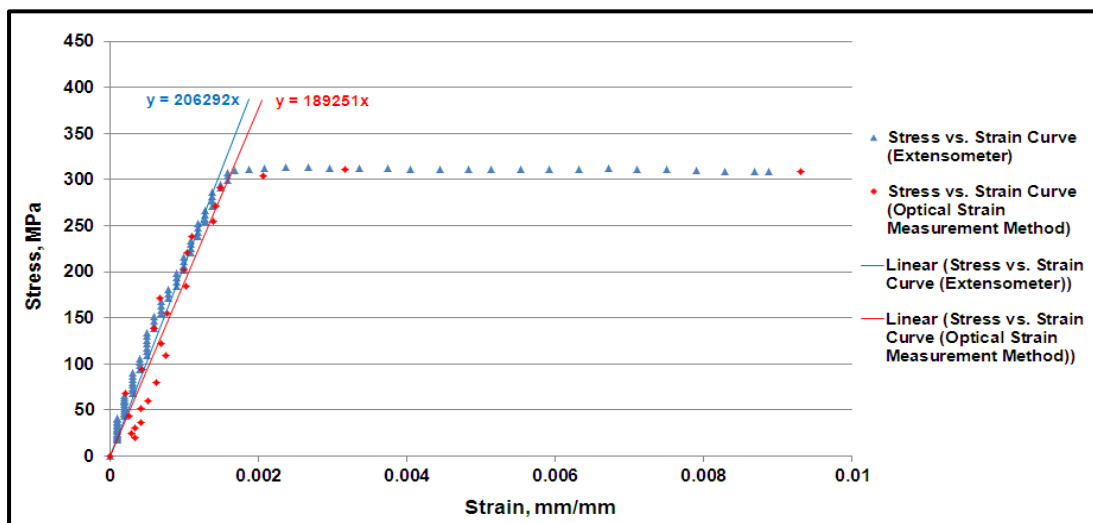


Fig. 4.8 Determination of the modulus of elasticity for the mild steel specimen

By referring to Fig 4.8, the modulus of elasticity for the first mild steel specimen determined by the extensometer and the optical strain measurement method were found to be 206 GPa and 189 GPa respectively. Based on these results, the first mild steel specimen was 8.25% off the benchmark value. Meanwhile, Table 4.4 shows the comparison of the modulus of elasticity determined by the extensometer and the optical strain measurement method for all five specimens that have been tested in the tensile test. Based on Table 4.4, the average value of the modulus of elasticity determined by the extensometer was 204 GPa. While for the average value of the modulus of elasticity determined by the optical strain measurement method was found to be 193 GPa. As a result, the average deviation was found to be 5.14% off the benchmark value. Through the comparison of the modulus of elasticity determined by the two methods mentioned above, the optical strain measurement method had been verified and a good agreement was achieved as the deviations were found to be around 5% off the benchmark value.

Table 4.4 Comparison of the modulus of elasticity determined by the extensometer and the optical strain measurement method

Specimens	Extensometer	Optical Strain Measurement Method	Deviation (%)
1	206 GPa	189 GPa	8.25
2	218 GPa	201 GPa	7.80
3	211 GPa	207 GPa	1.90
4	190 GPa	185 GPa	2.63
5	195 GPa	185 GPa	5.13

4.4.3.2 Polypropylene Specimens

In order to find the modulus of elasticity of the polypropylene specimens, the gradient of the stress-strain curve for the first specimen was plotted as in Fig. 4.9. Since a total of five specimens were tested during the tensile test, the remaining four gradients which represented the modulus of elasticity of the respective polypropylene specimens were included in Appendix F. Based on Fig. 4.9, the strain values determined from the extensometer readings (triangle dotted points) served as

the benchmark for the strain values determined by the optical strain measurement method (diamond dotted points). Meanwhile, all the dotted points were best fitted with the straight lines. As a result, the modulus of elasticity of the polypropylene specimen was successfully determined by the two methods mentioned above.

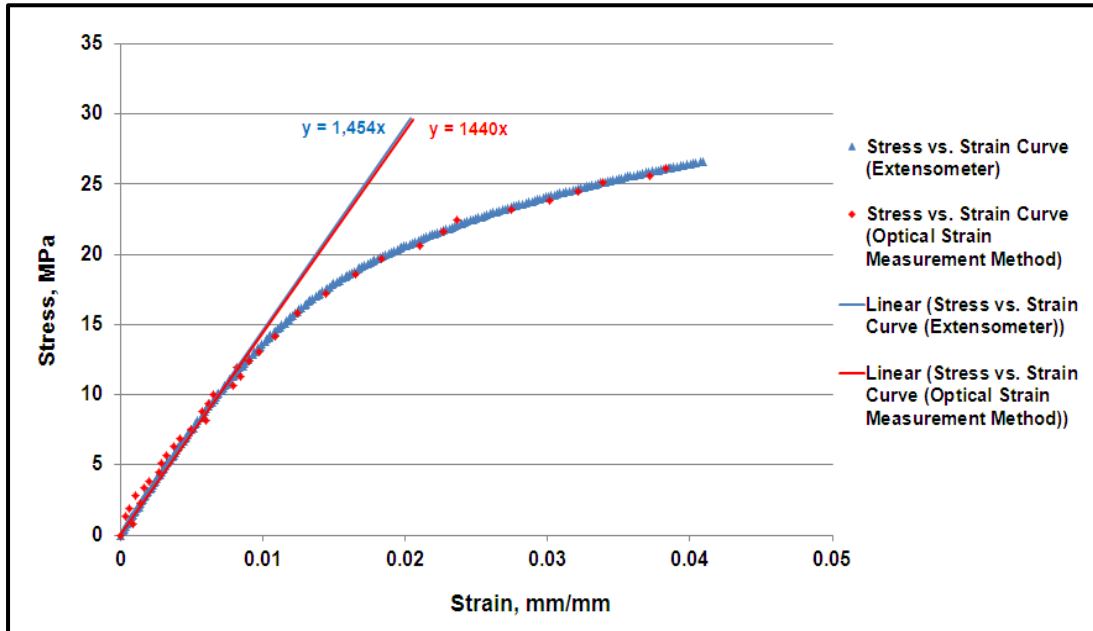


Fig. 4.9 Determination of the modulus of elasticity for the polypropylene specimen

By referring to Fig. 4.9, the modulus of elasticity for the first polypropylene specimen determined by the extensometer and the optical strain measurement method were found to be 1454 MPa and 1440 MPa respectively. Based on these results, the first polypropylene specimen was 0.96% off the benchmark values. Meanwhile, Table 4.5 shows the comparison of the modulus of elasticity determined by the extensometer and the optical strain measurement method for all five specimens that have been tested in the tensile test. Based on Table 4.5, the average value of the modulus of elasticity determined by the extensometer was 1533 MPa. While the average value of the modulus of elasticity determined by the optical strain measurement method was found to be 1497 MPa. As a result, the average deviation was found to be 2.35% off the benchmark value. Besides, the straight lines plotted nicely fitted the results determined by the optical strain measurement method (diamond dotted points). By referring to the comparison of the modulus of elasticity determined by the two methods mentioned above, the optical strain measurement method had been verified and a good agreement was achieved as the deviations were found to be 2.35% off the benchmark value.

Table 4.5 Comparison of the modulus of elasticity determined by the extensometer and the optical strain measurement method

Specimens	Extensometer	Optical Strain Measurement Method	Deviation (%)
1	1454 MPa	1440 MPa	0.96
2	1628 MPa	1509 MPa	7.31
3	1561 MPa	1488 MPa	4.68
4	1544 MPa	1542 MPa	0.13
5	1476 MPa	1504 MPa	1.90

4.5 Chapter Summary

In the beginning of this chapter, the validation of the Geometric Approach equation had been presented. The results determined by the ANSYS served as the benchmark for the values calculated by the Geometric Approach equation. For the two-dimensional and the three-dimensional mild steel models, the deviations were in the range of minimum 0.02% to the maximum of 0.08% off the benchmark values. While for two-dimensional and the three-dimensional polypropylene models, the deviations were in the range of minimum 0.41% to the maximum of 1.12% off the benchmark values. Basically, the deviations occurred as the term $\frac{\varepsilon^2}{2}$ in the Geometric Approach equation was found to be contributing a small value even though it was treated as negligible when the relative change in distance between the two nodes, ε is small. Nevertheless, the strain values determined by the ANSYS and the analytical calculations were still extremely close to each other. It shows that the Geometric Approach equation is accurate enough for this study.

Next, the optical strain measurement method was verified with the AutoCAD images before the MATLAB program can be used to analyze the images that were acquired during the strain inducing event. During the verification of the optical strain measurement method, the results determined by ANSYS served as the benchmark values. For the comparison of the results determined by the two methods mentioned above, the deviations were found to be less than 5% off the benchmark values. These

deviations occurred as the output images from the AutoCAD software were low in terms of image resolution. The deviations can be further reduced by increasing the image resolution of the output images. Based on these results, the optical strain measurement method was precise enough to determine the displacement of the speckles and hence compute the strain values accurately.

In the validation of the optical strain measurement method with the experimental results, tensile tests were conducted using the Universal Testing Machine. By using the strain values determined by the extensometer, the stress-strain curves were plotted and served as a benchmark for values determined by the optical strain measurement method. For the mild steel specimens, the strain values determined by the extensometer and the optical strain measurement method were close to each other. However, some deviations were observed at the beginning of the elastic region of the stress-strain curve. The results were found to be slightly fluctuating around the benchmark values when the strain values were below 0.008 mm/mm. Beyond the elastic limit, the yield point phenomenon was observed in the transition from the elastic to the plastic deformation and the Luders Bands were formed throughout the yield point elongation. Although the deformations occurred within the yield point elongation were reported to be heterogeneous or irregular, the results determined by the optical strain measurement method were found to be in the range of minimum 4.80% to the maximum of 10.83% off the benchmark values. When the strain values determined by the extensometer were in between the lower yield point and 0.12 mm/mm, the deviations were reported to be less than 5% off the benchmark values. Meanwhile, the results determined by the optical strain measurement method were in the range of minimum 5% to the maximum of 7.87% off the benchmark values when the strain values determined by the extensometer were in between 0.12 mm/mm and 0.18 mm/mm. Basically, these deviations were expected to occur as the Geometric Approach equation embedded in the MATLAB program contributes to these deviations. Throughout the comparison of the results determined by the two methods mentioned above, the small deviations proved that the optical strain measurement method was capable to determine the strain correctly. A good agreement was achieved upon comparison with the benchmark values especially when the strain values were above 0.024 mm/mm.

A total of five polypropylene specimens were also tested during the tensile test. The strain values determined by the extensometer and the optical strain measurement method were found to be extremely close to each other. At the same time, the deviations observed within the elastic region were small if compared to the deviations that occurred in the mild steel specimen. This happened as the polypropylene material has a smaller modulus of elasticity if compared to the mild steel material. However, the results were found to be slightly fluctuating around the benchmark values when the strain values were below 0.008 mm/mm. Nevertheless, the deviations were reduced as the strain values increased. When the strain values were in between 0.016 mm/mm (the elastic limit) and 0.075 mm/mm (the ultimate tensile strength point), the deviations were in the range of minimum 0.22% to the maximum of 3.63% off the benchmark values. In addition, the deviations were found to be less than 5% off the benchmark values when the strain values determined by the extensometer were below 0.14 mm/mm. Moreover, the results determined by the optical strain measurement method were in the range of minimum 5% to the maximum of 8.59% off the benchmark values when the strain values were in between 0.14 mm/mm to 0.16 mm/mm. Basically, these deviations occurred in the polypropylene specimens as necking took place in one of the extensometer's clips. Even though the extensometer still managed to compute the strain values but on the other hand, the captured images were unable to record the elongation correctly. This was because the video camera was set to capture the middle of the gauged section of the specimen during the tensile test. As a result, the strain values determined by the optical strain measurement method were smaller and 8.59% off the benchmark values when the strain value was approaching 0.16 mm/mm. From the comparison of the results determined by the two methods mentioned above, the small deviations proved that the optical strain measurement method was capable to determine the strain values correctly. A good agreement was achieved upon comparison with the benchmark values especially when the strain values were above 0.008 mm/mm.

Lastly, the modulus of elasticity of the mild steel and the polypropylene specimens were determined in order to verify the specimens' material properties. This can be achieved by further analyzing the gradient of the stress-strain curves within the elastic region. For the mild steel specimens, the average value of the modulus of elasticity determined by the extensometer was 204 GPa. While the

average value of the modulus of elasticity determined by the optical strain measurement method was found to be 193 GPa. As a result, the average deviation was found to be 5.14% off the benchmark value. Meanwhile for the polypropylene specimens, the average value of the modulus of elasticity determined by the extensometer and the optical strain measurement method were found to be 1533 MPa and 1497 MPa respectively. As a result, the average deviation was found to be 2.35% off the benchmark value. By referring to the comparison of the modulus of elasticity determined by the two methods mentioned above, the optical strain measurement method had been verified. A good agreement was achieved as the deviations for the mild steel and the polypropylene specimens were found to be 5.14% and 2.35% off the benchmark values respectively.

CHAPTER 5

CONCLUSIONS AND FUTURE WORK

5.1 Conclusions

The knowledge of strain is vital to the engineers as it plays an important role in most of the engineering designs and experimental works. As a result, the strain measurement becomes ultimately important in many engineering applications since the manmade structures and machines are getting more complex than before. A precise strain measurement method is always desirable as a misleading result might cause a catastrophic incident and also put human lives in jeopardy. In this study, various strain measurement methods have been studied and reviewed but each method was found to have its own disadvantages. There is a great need to develop a precise and yet simple strain measurement method in mechanical testing. Therefore in this study, the objective was to develop a two-dimensional strain measurement algorithm that calculates the strain for a loaded structural component by using Digital Image Correlation (DIC) technique.

In the beginning of this study, the DIC technique introduced by Peters and Ranson was studied and the Geometric Approach equation was analyzed in great detail. For example, the Geometric Approach equation had been validated with the two-dimensional and three-dimensional ANSYS simulation models. The results determined by the ANSYS served as the benchmark for the values calculated by the analytical equation. For the two-dimensional and the three-dimensional mild steel models, the deviations were in the range of minimum 0.02% to the maximum of 0.08% off the benchmark values. While for two-dimensional and the three-dimensional polypropylene models, the deviations were in the range of minimum 0.41% to the maximum of 1.12% off the benchmark values. Basically, the

deviations occurred as the term $\frac{\varepsilon^2}{2}$ in the Geometric Approach equation was found to be contributing a small value even though it was treated as negligible when the relative change in distance between the two nodes, ε is small. Nevertheless, the strain values determined by the ANSYS and the analytical calculations were still extremely close to each other. As a result, the Geometric Approach equation was found to be accurate enough for this study.

In the second part of this study, a strain measurement algorithm was developed. Basically, the development of the strain measurement algorithm was divided into eight main parts, so that each part can be coded and tested separately. By using the MATLAB's Image Processing Toolbox, the strain measurement algorithm was turned into MATLAB program successfully. Meanwhile, the Geometric Approach equation was embedded in the MATLAB program and was used to calculate the strain in a loaded structural component. Before the MATLAB program was used to analyze the images that were acquired during the strain inducing event, this optical strain measurement method was verified with the AutoCAD images. From the comparison of the results determined by the ANSYS simulation models and the optical strain measurement method, the deviations were found to be less than 5% off the benchmarks values. Based on these deviations, the optical strain measurement method proved to be capable to analyze the two images that were created under two different states smoothly, as well as to determine the strain accurately.

A series of tensile tests were also conducted using the Universal Testing Machine. Before the experiments were conducted, the surface of the specimens had been deposited with the black paint to create the random speckles pattern effect. By adopting the ASTM E8M and ISO 527-1, a total of five specimens made of mild steel and polypropylene materials respectively were tested. During the strain inducing event, the extensometer was used for strain measurement which served as a benchmark for the values determined from the optical strain measurement method. Simultaneously, videos were recorded using a consumer version of high-definition video camera. Then, the extracted images from the recorded videos were analyzed by the MATLAB program and the two-dimensional deformation measurement was successfully determined.

In the validation of the optical strain measurement method with the experimental results, the results determined by the extensometer and the optical strain measurement method were compared to each other. By using the strain values determined by the extensometer, the stress-strain curves were plotted and they served as benchmarks for values determined by the optical strain measurement method. For the mild steel specimens, the strain values determined by the two methods mentioned above were close to each other. Although some deviations were still observed during the comparison of the results determined by the extensometer and the optical strain measurement method, the deviations were reasonably small. While for the polypropylene specimens, the deviations observed were even smaller if compared to the deviations that occurred in the mild steel specimens. As a result, the optical strain measurement method was found to be capable to determine the strain correctly. A good agreement was achieved upon comparison with the benchmark values especially when the strain value was above 0.008 mm/mm.

In the last part of this study, the modulus of elasticity of the mild steel and the polypropylene specimens were determined successfully using the optical strain measurement method. For the mild steel specimens, the modulus of elasticity was found to be 193 GPa and 5.14% off the benchmark value. Meanwhile for the polypropylene samples, the modulus of elasticity was found to be 1497 MPa and 2.35% off the benchmark values. By referring to the comparison of the modulus of elasticity determined by the two methods mentioned above, the optical strain measurement method had been verified and a good agreement was achieved as the deviations were found to be very small.

By comparing the results determined by the extensometer and the optical strain measurement method, the deviations in terms of percentage had been found to be relatively small. In conclusion, the two-dimensional measurement algorithm that calculates the strain in a loaded structural component had been developed successfully in the study. In addition, the consumer version of high-definition video camera has been proven to be capable to capture the deformed images impeccably especially when the strain was above 0.008 mm/mm.

5.2 Future Work

After completing this study, there are several pieces of work which merit further study and the recommendations are given below:

1. Development of an automated two-dimensional strain measurement algorithm

The two-dimensional measurement algorithm can be automated by introducing the *looping* function into the programming codes. By having the automated strain measurement algorithm, the selection of the speckles in the subsequent images will be automated and the procedure for the strain determination can be simplified further.

2. The effect of light intensity during the tensile test

Since the effect of light intensity in the recorded videos (captured images) is crucial, the light condition inside the lab has to be controlled. This is necessary as the captured images at two different states must have the same light intensity throughout the strain inducing event. As a result, all the glass windows inside the lab have to be blocked, so that the sunlight will not be able to enter the lab and affect the light intensity of the captured images. Besides, the input of the light sources has to be converted from DC to AC power. This is because the light sources are proven to be unable to provide a constant light intensity throughout the strain inducing event. It tends to get dim after just 10 minutes of usage.

3. Installation of the hydraulic gripper in the Universal Testing Machine

Based on the obtained data in this study, a maximum load of 33 kN was recorded during the tensile tests for the mild steel specimens. Most of the time, the manual operating gripper was found to be unable to hold the specimen properly and hence the slip problem occurred. In order to overcome this problem, the manual operating gripper in the Universal Testing Machine has to be replaced with a hydraulic gripper.

REFERENCES

- [1] W. C. Young and R. G. Budynas, "Stress and strain: Important relationships," in *Roark's Formulas for Stress and Strain*, 7th ed. New York: McGraw-Hill, 2002, pp. 13.
- [2] D. R. Askeland and P. P. Phule, "Mechanical properties and behaviour," in *The Science and Engineering of Materials*, 4th ed. California: Thomson Learning, 2003, pp. 234.
- [3] A. S. Khan and X. W. Wang, "Stress, strain, and stress-strain relationship," in *Strain Measurements and Stress Analysis*, New Jersey: Prentice Hall, 2001, pp. 18.
- [4] J. M. Gere and S. P. Timoshenko, "Tension, compression, and shear," in *Mechanics of Materials*, 2nd ed. New Delhi, India: CBS, 2004, pp. 26-27.
- [5] R. C. Hibbeler, "Strain," in *Mechanics of Materials*, 6th ed. Jurong, Singapore: Prentice Hall, 2005, pp. 73.
- [6] A. S. Khan and X. W. Wang, "Metal-foil resistance strain gages," in *Strain Measurements and Stress Analysis*, New Jersey: Prentice Hall, 2001, pp. 30.
- [7] W. D. Pilkey, "Stress and strain," in *Formulas for Stress, Strain and Structural Matrices*, 2nd ed. New Jersey: Wiley, 2005, pp. 113.
- [8] T. L. Haglage and H. A. Wood, "Scratch strain gage evaluation," Air Force Flight Dynamics Lab., Wright-Patterson Air Force Base, Ohio, Tech. Rep. AFFDL-TR-69-25, July 1969.
- [9] W. C. Young and R. G. Budynas, "Experimental methods," in *Roark's Formulas for Stress and Strain*, 7th ed. New York: McGraw-Hill, 2002, pp. 83.
- [10] A. S. Khan and X. W. Wang, "Metal-foil resistance strain gages," in *Strain Measurements and Stress Analysis*, New Jersey: Prentice Hall, 2001, pp. 33.
- [11] *Model 3542 Axial Extensometers*, Epsilon Tech. Co., Wyoming, USA, 2010.
- [12] *Principles of Stresscoat, Brittle Coating for Experimental Stress Analysis*, Oconomowoc, WI, USA, 2010.
- [13] A. S. Khan and X. W. Wang, "Photoelasticity," in *Strain Measurements and Stress Analysis*, New Jersey: Prentice Hall, 2001, pp. 99.
- [14] A. S. Khan and X. W. Wang, "Photoelastic-coating method," in *Strain Measurements and Stress Analysis*, New Jersey: Prentice Hall, 2001, pp. 150.

- [15] “Good practice guide to geometric moiré for in plane displacement or strain analysis,” SPOTS Standard Part III (1), G6RD-CT-2002-00856, Dec 2005.
- [16] A. S. Khan and X. W. Wang, “Holographic interferometry,” in *Strain Measurements and Stress Analysis*, New Jersey: Prentice Hall, 2001, pp. 211.
- [17] H. Fein, “Holographic Interferometry: Non-destructive tool,” *The Industrial Physicist*, American Institute of Physics, Sept 1997.
- [18] M. A. Sutton *et al.*, “Digital image correlation,” in *Image Correlation for Shape, Motion and Deformation Measurements: Basic Concepts, Theory and Applications*, Springer Science, 2009, pp. 81.
- [19] M. A. Sutton, “Digital image correlation for shape and deformation measurements,” in *Handbook of Experimental Solid Mechanics*, Springer, 2008, pp. 566.
- [20] P. K. Rastogi, “Interferometric optical testing,” in *Optical Measurement Techniques and Applications*, Boston: Artech House, 1997, pp. 87.
- [21] Y. H. Huang, “Development of digital image correlation method for displacement and shape measurement,” M.S. thesis, Mech. Dept., NUS, Singapore, 2004.
- [22] W. H. Peters and W. F. Ranson, “Digital imaging techniques in experimental stress analysis,” *Opt. Eng.*, vol. 21, pp. 427, 1982.
- [23] M. A. Sutton, W. J. Wolters, W. H. Peters, W. F. Ranson and S. R. McNeill, “Determination of displacements using an improved digital image correlation method,” *Image Vis. Comp.*, vol. 1, pp. 133-139, 1983.
- [24] T. C. Chu, W. F. Ranson, M. A. Sutton and W. H. Peters, “Applications of digital image correlation techniques to experimental mechanics,” *Exp. Mech.*, vol. 25, pp. 232-244, 1985.
- [25] M. A. Sutton, M. Q. Cheng, W. H. Peters, Y. J. Chao and S. R. McNeill, “Application of an optimized digital correlation method to planar deformation analysis,” *Image Vis. Computer*, vol. 4, pp. 143-150, 1986.
- [26] H. A. Bruck, S. R. McNeill, M. A. Sutton and W. H. Peters, “Digital image correlation using Newton-Raphson method of Partial Differential Correction,” *Exp. Mech.*, vol. 29, pp. 261-267, 1989.

- [27] G. Vendroux and W. G. Knauss, "Submicron deformation field measurements: Part 2. Improved digital image correlation," *Exp. Mech.*, vol. 38, pp. 86-92, 1998.
- [28] H. Lu and P. D. Cary, "Deformation measurements by digital image correlation: Implementation of a second-order displacement gradient," *Exp. Mech.*, vol. 40, pp. 393-400, 2000.
- [29] P. Cheng, M. A. Sutton, H. W. Schreier and S. R. McNeill, "Full-field speckle pattern image correlation with B-Spline deformation function," *Exp. Mech.*, vol. 42, pp. 344-352, 2002.
- [30] P. C. Hung and A. S. Voloshin, "In-plane strain measurement by digital image correlation," *Journal of the Brazilian Soc. Of Mech. Sci. And Eng.*, vol. 25, pp. 215-221, 2003.
- [31] L. B. Meng, G. C. Jin and X. F. Yao, "Application of iteration and finite element smoothing technique for displacement and strain measurement of digital speckle correlation," *Journal of Optics and Lasers in Eng.*, vol. 45, pp. 57-63, 2007.
- [32] C. Cofaru, W. Philips and W. V. Paepegem, "Improved Newton-Raphson digital image correlation method for full-field displacement and strain calculation," *Journal of Applied Optics*, vol. 49, pp. 6472-6484, 2010.
- [33] G. L. Hovis, "Centroidal tracking algorithm for deformation measurements using gray scale digital images," Ph.D. dissertation, University of South Carolina, May 1989.
- [34] C. Glover and H. Jones, "Stress, strain and deformation in solids," in *Conservation Principles of Continuous Media*, Texas: McGraw-Hill, 1994, pp. 215.
- [35] G. L. Hovis, W. F. Ranson, H. J. Reed and C. T. Etheredge, "Vision system for remote strain or deformation measurement," Savannah River Technology Center, USA, 1999.
- [36] D. J. Chen, F. P. Chiang, Y. S. Tan and H. S. Don, "Digital speckle-displacement measurement using a complex spectrum method," *Journal of Applied Optics*, vol. 32, pp.1839-1849, 1993.

- [37] D. Amodio, G. B. Broggiato, F. Campana and G. M. Newaz, "Digital speckle correlation for strain measurement by image analysis," *Exp. Mech.*, vol. 43, pp. 396-402, 2003.
- [38] M. A. Sutton, S. R. McNeill, J. Jang and M. Babai, "Effects of subpixel image restoration on digital image correlation error estimates," *Ops. Eng.*, vol. 27, pp. 870-877, 1988.
- [39] B. Wattrisse, A. Chrysochoos, J. M. Muracciole and M. N. Gaillard, "Analysis of strain localization during tensile tests by digital image correlation," *Exp. Mech.*, vol. 41, pp. 29-39, 2000.
- [40] H. W. Schreier, J. R. Braasch and M. A. Sutton, "Systematic errors in digital image correlation caused by intensity interpolation," *Opt. Eng.*, vol. 39, pp. 2915-2921, 2000.
- [41] H. W. Schreier and M. A. Sutton, "Systematic errors in digital image correlation due to undermatched subset shape functions," *Exp. Mech.*, vol. 42, pp. 303-310, 2002.
- [42] J. Zhang, G. C. Jin, S. P. Ma and L. B. Meng, "Application of an improved subpixel registration algorithm on digital speckle correlation measurement," *Opt. and Laser Tech.*, vol. 35, pp. 533-542, 2003.
- [43] D. Lecompte, A. Smits, S. Bossuyt, H. Sol, J. Vantomme, D. Van Hemelrijck and A. M. Habraken, "Quality assessment of speckle patterns for digital image correlation," *Opt. and Lasers in Eng.*, vol. 44, pp. 1132-1145, 2006.
- [44] Y. F. Sun and H. L. Pang, "Study of optimal subset size in digital image correlation of speckle pattern images," *Opt. and Lasers in Eng.*, vol. 45, pp. 967-974, 2007.
- [45] H. Haddadi and S. Belhabib, "Use of rigid-body motion for the investigation and estimation of the measurement errors related to digital image correlation technique," *Opt. and Lasers in Eng.*, vol. 46, pp. 185-196, 2008.
- [46] M. Jerabek, Z. Major and R. W. Lang, "Strain determination of polymeric materials using digital image correlation," *Polymer Testing*, vol. 29, pp. 407-416, 2010.
- [47] Y. Wang and A. M. Cuitino, "Full-field measurements of heterogeneous deformation patterns on polymeric foams using digital image correlation," *Int. Journal of Solids and Structures*, vol. 39, pp. 3777-3796, 2002.

- [48] W. H. Peters, M. A. Sutton, W. F. Ranson, W. P. Poplin and D. M. Walker, "Whole-field experimental displacement analysis of composite cylinders," *Exp. Mech.*, 1989.
- [49] S. R. McNeill, M. A. Sutton, Z. Miao and J. Ma, "Measurement of surface profile using digital image correlation," *Exp. Mech.*, vol. 37, pp. 13-20, 1997.
- [50] F. V. Diaz, A. F. Armas, G. H. Kaufmann and G. E. Galizzi, "Fatigue damage accumulation around a notch using a digital image measurement system," *Exp. Mech.*, vol. 44, pp. 241-246, 2004.
- [51] Z. Y. Wang, H. Q. Li, J. W. Tong, M. Shen, F. Aymerich and P. Priolo, "Dual magnification digital image correlation based strain measurement in CFRP Laminates with open hole," *Composites Sci. and Tech.*, vol. 68, pp. 1975-1980, 2008.
- [52] V. Savic, L. G. Hector and J. R. Fekete, "Digital image correlation study of plastic deformation and fracture in fully martensitic steels," *Exp. Mech.*, 2008.
- [53] W. V. Paepegem, A. A. Shulev, I. R. Roussev, S. D. Pauw, J. Degrieck and V. C. Sainov, "Study of the deformation characteristics of window security film by digital image correlation techniques," *Optics and Lasers in Eng.*, vol. 47, pp. 390-397, 2009.
- [54] J. A. Bueno and J. Lambros, "Investigation of crack growth in functionally graded materials using digital image correlation," *Eng. Fracture Mech.*, vol. 69, pp. 1695-1711, 2002.
- [55] S. Vanlanduit, J. Vanherzeele, R. Longo and P. Guillaume, "A digital image correlation method for fatigue test experiments," *Optics and Lasers in Eng.*, vol. 47, pp. 371-378, 2009.
- [56] R. Stephane and H. Francois, "Stress intensity factor measurements from digital image correlation: post-processing and integrated approaches," *Int. Journal of Fracture*, vol. 140, pp. 141-157, 2006.
- [57] P. L. Crespo, A. Shterenlikht, E. A. Patterson, J. R. Yates and P. J. Withers, "The stress intensity of mixed mode cracks determined by digital image correlation," *Journal of Strain Analysis*, vol. 43, pp. 769-780, 2008.
- [58] J. S. Lyons, J. Liu and M. A. Sutton, "High-temperature deformation measurements using digital image correlation," *Exp. Mech.*, vol. 36, pp. 64-70, 1996.

- [59] B. M. B. Grant, H. J. Stone, P. J. Withers and M. Preuss, "High-temperature strain field measurement using digital image correlation," *Journal of Strain Analysis*, vol. 44, pp. 263-271, 2009.
- [60] B. Pan, D. F. Wu and Y. Xia, "High-temperature deformation field measurement by combining transient aerodynamic heating simulation system and reliability-guided digital image correlation," *Opt. and Lasers in Eng.*, vol. 48, pp. 841-848, 2010.
- [61] W. Wu, W. H. Peters and M. Hammer, "Basic mechanical properties of retina in simple tension," *Journal of Biomechanical Eng.*, vol. 109, pp. 1, 1987.
- [62] J. Hjortdal and P. K. Jensen, "In vitro measurement of corneal strain, thickness, and curvature using digital image correlation," *Acta Oph.Scandinavica*, vol. 73.1, pp. 5-11, 1995.
- [63] C. B. Wang, J. M. Deng, G. A. Ateshian and T. Hung, "An automated approach for direct measurement of two dimensional strain distributions within articular cartilage under unconfined compression," *Journal of Biomechanical Eng.*, vol. 124, pp. 557-567, 2002.
- [64] Y. J. Chao and M. A. Sutton, "Measurement of strains in paper tensile specimen using computer vision and digital image correlation," *Journal of Tappi*, vol. 70, pp. 153-156, 1988.
- [65] D. Choi, J. L. Thorpe and R. B. Hanna, "Image analysis to measure strain in wood and paper," *Wood Sci. Tech.*, vol. 25, pp. 251, 1991.
- [66] J. J. Lee and M. Shinozuka, "Real time displacement measurement of a flexible bridge using digital image processing techniques," *Exp. Mech.*, vol. 46, pp. 105-114, 2006.
- [67] J. D. Chen, G. C. Jin and L. B. Meng, "Applications of digital image correlation method to structure inspection," *Tsinghua Sci. and Tech.*, vol. 12, pp. 237-243, 2007.
- [68] Z. L. Sun, J. S. Lyons and S. R. McNeill, "Measuring microscopic deformations with digital image correlation," *Optics and Lasers in Eng.*, vol. 27, pp. 409-428, 1997.
- [69] G. Vendroux, N. Schmidt and W. G. Knauss, "Submicron deformation field measurements: Part III, Demonstration of deformation determination," *Exp. Mech.*, vol. 38, pp. 154-160, 1998.

- [70] H. Jin, W. Y. Lu and J. Korellis, "Micro-scale deformation measurement using the digital image correlation technique and scanning electron microscope imaging," *Journal of Strain Analysis*, vol. 43, pp. 719-728, 2008.
- [71] F. Hild and S. Roux, "Digital image correlation: From displacement measurement to identification of elastic properties," Submitted to *Journal of Strain Analysis*, 2005.
- [72] F. M. Sanchez-Arevalo, T. Garcia-Fernandez, G. Pulos and M. Villagran-Muniz, "Use of digital speckle pattern correlation for strain measurements in a CuAlBe shape memory alloy," *Mat. Characterization*, vol. 60, pp.775-782, 2009.
- [73] S. H. Tung, M. H. Shih and J. C. Kuo, "Application of digital image correlation for anisotropic plastic deformation during tension testing," *Optics and Lasers in Eng.*, vol. 48, pp. 636-641, 2010.
- [74] H. Leclerc, J. N. Perie, S. Roux and F. Hild, "Integrated digital image correlation for the identification of mechanical properties," *Springer-Verlag Berlin Heidelberg*, pp. 161-171, 2009.
- [75] N. Pasquini, "Product mix and properties," in *Polypropylene Handbook*, 2nd ed. Munich, Germany: Carl Hanser Verlag, 2005, pp. 328-329.
- [76] "Structural Fundamentals," in *Release 11.0 Documentation for ANSYS*, ANSYS, Pennsylvania, USA, 2007.
- [77] S. J. Chapman, "Branching statements and program design," in *Essentials of MATLAB Programming*, Toronto, Canada: Thomson, 2006, pp. 86.
- [78] V. Savic, L. G. Hector and J. R. Fekete, "Digital image correlation study of plastic deformation and fracture in fully martensitic steel," *Exp. Mech.*, accepted on 22 Sept. 2008.
- [79] C. Glover and H. Jones, "Stress, strain and deformation in solids," in *Conservation Principles of Continuous Media*, Texas: McGraw-Hill, 1994, pp. 216.
- [80] C. A. Parker and P. J. Sikorsky, "Representation of stress-strain behavior," in *Atlas of Stress-Strain Curves*, 2nd ed. Ohio: ASM International, 2002, pp. 1.
- [81] J. R. Davis, "Mechanical behaviour of materials under tensile loads," in *Tensile Testing*, 2nd ed. Ohio: ASM International, 2004, pp. 13.

- [82] D. R. Askeland and P. P. Phule, "Mechanical properties and behaviour," in *The Science and Engineering of Materials*, 4th ed. California: Thomson Learning, 2003, pp. 245.
- [83] J. R. Davis, "Mechanical behaviour of materials under tensile loads," in *Tensile Testing*, 2nd ed. Ohio: ASM International, 2004, pp. 15-16.
- [84] C. A. Parker and P. J. Sikorsky, "Representation of stress-strain behavior," in *Atlas of Stress-Strain Curves*, 2nd ed. Ohio: ASM International, 2002, pp. 3-4.

PUBLICATIONS

1. S. W. Khoo and S. Karuppanan, "Stress intensity factor for cracks emanating from a shaft," *Journal of Applied Sciences*, in press.
2. S. W. Khoo, S. Karuppanan and M. R. B. Abdul Latif, "Development of an optical strain measurement method", accepted by *IEEE Xplore*, Dec. 2010.
3. S. W. Khoo, S. Karuppanan and M. R. B. Abdul Latif, "Development of an optical strain measurement method using digital image correlation," accepted by *International Conference on Imaging Systems and Techniques*, March 2011.

APPENDIX A

MILD STEEL CERTIFICATE

Ahp:Ms New

AMSTEEL MILLS SDN BHD (63077-A)

Member of the UOH Group
MILL TEST CERTIFICATE

Customer: **TRIO BEE HARDWARE SDN BHD (TP)**

Commodity: **MILD STEEL FLAT BAR**

Certificate No: **34920/09**

Address: **42-44 JALAN SENDAHARA
31450 EPON
PERAK**

Specification: **JIS # S101 50400**

DCO No: **801860**

Contract No:

Date of Issue: **4/12/09**

Size (mm)	Heat No	ECSA (mm ²)	Rolling Mass (Kgrm)	No of Bundles / Coil	Mechanical Properties				Chemical Composition (%)							
					Yield (N/mm ²)	Tensile (N/mm ²)	Stress Ratio	EL %	Bend Test (180°)	Rebend Test	C x 100	Si x 100	Mn	P x 1000	S x 1000	
04.5E25	167036			2	348	468		28	PASSED			14	14	48	1.5	27
04.5E25	167038			2	354	479		30	PASSED			15	14	49	1.4	20
04.5E25	167046			1	372	482		31	PASSED			15	14	52	1.2	26
04.5E25	167049			2	314	487		29	PASSED			14	13	49	1.3	26
04.5E25	167050			1	347	467		28	PASSED			15	14	48	1.6	22
04.5E25	167052			1	347	475		31	PASSED			14	15	48	1.6	30
05.0E25	167097			2	338	464		27	PASSED			16	14	48	1.3	42
06.0E25	167004			4	323	442		25	PASSED			16	14	47	2.2	40

ITEM(S) = 3 ONLY

Remarks: ECSA = Effective Cross Section Area
CE = Carbon Equivalent
LICENSE NO. PA011107

DELIVER TO: **TRIO BEE HARDWARE SDN BHD
WISMA SOON TEIK 8/8
JALAN SENDAHARA
EPON PERAK**

We hereby certify that the material described herein has been made and tested in accordance with the above specification.



YEE SEN TAT

Authorized Signature

XX = Denote Nominal Size Of Deformed Bar

MILL TEST CERTIFICATE IN A CUSTOMER REQUESTED COPY AND NO SIGNATURE REQUIRED

Office: Lot 1, Jalan Waqa, Bukit Paga Industrial Estate, 47050 Klang, Selangor Darul Ehsan, Malaysia.
M/s (Klang) Antara: Lot 2, Kuala Merau, Bukit Paga Industrial Estate, 47050 Klang, Selangor Darul Ehsan, Malaysia.

FROM: TRIO BEE HARDWARE SDN BHD FAX NO: 052415111 Jul. 14 2010 12:24PM P:

APPENDIX B

TWO-DIMENSIONAL STRAIN MEASUREMENT MATLAB PROGRAM

Script file: Two-Dimensional Strain Measurement MATLAB Program.m

Purpose:

This program is used to determine the two-dimensional measurement of a loaded structural component. This can be achieved by executing the two images that are acquired at two different states, one before deformation (undeformed image) and the other one after deformation (deformed images). Besides, this program is able to extract 4 speckles from the random speckles pattern from each of the input images, as well as to determine the centroids of the selected speckles. Finally, the embedded Geometric Approach equation in the MATLAB program is able to calculate the displacement of the speckles and lastly, determine the normal strains in xx , yy and the shear strain in xy direction.

Record of revisions:

Date	Programmer	Description of change
====	=====	=====
22/4/2010	S.W. Khoo	Original code

Define variables:

I -- First image (undeformed image) that is input into the program
I2 -- Second image (deformed images) that is input into the program
M -- Height/Vertical of the undeformed image in the unit of pixel resolution
N -- Width/Horizontal of the undeformed image in the unit of pixel resolution
M2 -- Height/Vertical of the deformed images in the unit of pixel resolution
N2 -- Width/Horizontal of the deformed images in the unit of pixel resolution
image_res_x -- Image resolution of the input images in x-axis (unit: pixels/mm)
image_res_y -- Image resolution of the input images in y-axis (unit: pixels/mm)
BW -- Binary image that is converted from the undeformed image
BW2 -- Binary images that are converted from the deformed images
BW3 -- Binary image that contains 4 extracted speckles from the undeformed image
BW4 -- Binary image that contains 4 extracted speckles from the deformed images
L -- Matrix L, the same size as BW3, containing label for the connected objects in BW3
L2 -- Matrix L, the same size as BW4, containing label for the connected objects in BW4
K -- Number of elements in array/subscripted array expression
S -- Structure array that stored the speckles' centroid in the undeformed image
s2 -- Structure array that stored the speckles' centroid in the deformed images

```

t      -- Structure array used to store the speckles' number
centroid_1 -- Centroid of the first selected speckle in the undeformed image
centroid_2 -- Centroid of the second selected speckle in the undeformed image
centroid_3 -- Centroid of the third selected speckle in the undeformed image
centroid_4 -- Centroid of the fourth selected speckle in the undeformed image
centroid_1d -- Centroid of the first selected speckle in the deformed images
centroid_2d -- Centroid of the second selected speckle in the deformed images
centroid_3d -- Centroid of the third selected speckle in the deformed images
centroid_4d -- Centroid of the fourth selected speckle in the deformed images
centroid_1_x -- Centroid of the first selected speckle in x-axis (undeformed image)
centroid_1_y -- Centroid of the first selected speckle in y-axis (undeformed image)
centroid_2_x -- Centroid of the second selected speckle in x-axis (undeformed image)
centroid_2_y -- Centroid of the second selected speckle in y-axis (undeformed image)
centroid_3_x -- Centroid of the third selected speckle in x-axis (undeformed image)
centroid_3_y -- Centroid of the third selected speckle in y-axis (undeformed image)
centroid_4_x -- Centroid of the fourth selected speckle in x-axis (undeformed image)
centroid_4_y -- Centroid of the fourth selected speckle in y-axis (undeformed image)
centroid_1d_x -- Centroid of the first selected speckle in x-axis (deformed images)
centroid_1d_y -- Centroid of the first selected speckle in y-axis (deformed images)
centroid_2d_x -- Centroid of the second selected speckle in x-axis (deformed images)
centroid_2d_y -- Centroid of the second selected speckle in y-axis (deformed images)
centroid_3d_x -- Centroid of the third selected speckle in x-axis (deformed images)
centroid_3d_y -- Centroid of the third selected speckle in y-axis (deformed images)
centroid_4d_x -- Centroid of the fourth selected speckle in x-axis (deformed images)
centroid_4d_y -- Centroid of the fourth selected speckle in y-axis (deformed images)
s1      -- Length between the first and the second speckles in the undeformed image
s2      -- Length between the first and the third speckles in the undeformed image
s3      -- Length between the first and the fourth speckles in the undeformed image
s1d     -- Length between the first and the second speckles in the deformed images
s2d     -- Length between the first and the third speckles in the deformed images
s3d     -- Length between the first and the fourth speckles in the deformed images
strain_1 -- Relative change in distance between the first and the second speckle
strain_2 -- Relative change in distance between the first and the third speckle
strain_3 -- Relative change in distance between the first and the fourth speckle
cos_x1  -- Orientation of the line element in the angle of theta_x between the first and the
          second speckle (undeformed image)
cos_x2  -- Orientation of the line element in the angle of theta_x between the first and the
          third speckle (undeformed image)
cos_x3  -- Orientation of the line element in the angle of theta_x between the first and the
          fourth speckle (undeformed image)

```

cos_y1 -- Orientation of the line element in the angle of theta_y between the first and the second speckles (undeformed image)
 cos_y2 -- Orientation of the line element in the angle of theta_y between the first and the third speckle (undeformed image)
 cos_y3 -- Orientation of the line element in the angle of theta_y between the first and the fourth speckle (undeformed image)
 a -- Matrix a stored the product of the angle of theta in 3x3 matrix form (The embedded Geometric Approach Equation is applied to solve the three simultaneous equations)
 b -- Matrix b stored the product of the relative change in distance between the speckles in 3x1 matrix form
 c -- Matrix c stored the normal strain in xx, yy, xy directions
 Exx -- Normal strain in xx direction
 Eyy -- Normal strain in yy direction
 Exy -- Normal strain in xy direction

Input the first and second image into MATLAB.

```

I = imread ('C:\The directory of the reference or undeformed image.jpg');
I2 = imread ('C:\The directory of the deformed images.jpg');
  
```

Used to determine the size of the first image, I and the second image, I2

```

[M, N] = size (I);
[M2, N2] = size (I2);
  
```

N (horizontal-axis) is divided by 3 if the input images are in *jpg* or *bmp* format

```

N = round (N/3);
N2 = round (N2/3);
  
```

Check the sizes of the first and the second input images

```

if M == M2 && N == N2
  
```

Display a message when the input images are not the same sizes

```

else
  disp('The sizes of the input images are not the same');
end
  
```

Prompt the user to enter the image resolution in x and y directions

```

disp ('== Enter the respective image resolution ==');
image_res_x = input ('Enter the value of image resolution in x direction: ');
image_res_y = input ('Enter the value of the image resolution in y direction: ');
  
```

Conversion of the image format and enhance the images' features

```
BW = (im2bw (I, 0.30));  
BW2 = (im2bw (I2, 0.30));
```

Selection of the four speckles from the random speckles pattern (Undeformed image)

```
BW3 = bwselect (~BW,4);
```

Used to display the BW and BW3 binary images

```
imshow (BW)  
figure, imshow (BW3)
```

Label the selected speckles in the undeformed image

```
L = bwlabel (BW3);
```

Make sure no rounding is happened during the determination of the strain measurement

```
format long eng  
format compact
```

Define the structure array that stored the speckles' centroid in the undeformed image

```
s = regionprops (L, 'Centroid')  
imshow (L == 1)  
centroid_1 = s(1).Centroid  
imshow (L == 2)  
centroid_2 = s(2).Centroid  
imshow (L == 3)  
centroid_3 = s(3).Centroid  
imshow (L == 4)  
centroid_4 = s(4).Centroid
```

Selection of the four speckles from the random speckles pattern (Deformed Images)

```
BW4 = bwselect (~BW2,4);
```

Used to display the BW2 and BW4 binary images

```
imshow (BW2)  
figure, imshow (BW4)
```

Label the selected speckles in the deformed image

```
L2 = bwlabel (BW4);
```

Define the structure array that stored the speckles' centroid in the deformed image

```
s2 = regionprops (L2, 'Centroid')
imshow (L2 == 1)
centroid_1d = s2(1).Centroid
imshow (L2 == 2)
centroid_2d = s2(2).Centroid
imshow (L2 == 3)
centroid_3d = s2(3).Centroid
imshow (L2 == 4)
centroid_4d = s2(4).Centroid
```

Plot the numbers onto the centre of the selected speckles in the undeformed image

```
imshow (BW3)
hold on
    for k = 1:numel(s)
        t = s(k).Centroid;
        text (t(1), t(2), sprintf('%d', k), ...
            'Color','r',...
            'FontWeight', 'bold',...
            'HorizontalAlignment', 'left', ...
            'VerticalAlignment', 'bottom');
        plot (s(k).Centroid(1), s(k).Centroid(2), 'r*')
    end
hold off
```

Plot the numbers onto the centre of the selected speckles in the deformed image

```
figure,
imshow(BW4)
hold on
    for k = 1:numel(s2)
        t = s2(k).Centroid;
        text (t(1), t(2), sprintf('%d', k), ...
            'Color', 'r',...
            'FontWeight', 'bold',...
            'HorizontalAlignment', 'left', ...
            'VerticalAlignment', 'bottom');
        Plot (s2(k).Centroid(1), s2(k).Centroid(2), 'r*')
    end
hold off
```

Conversion of the centroids' unit from pixel to millimetre

```
centroid_1_x = centroid_1(1)/image_res_x  
centroid_1_y = centroid_1(2)/image_res_y  
centroid_2_x = centroid_2(1)/image_res_x  
centroid_2_y = centroid_2(2)/image_res_y  
centroid_3_x = centroid_3(1)/image_res_x  
centroid_3_y = centroid_3(2)/image_res_y  
centroid_4_x = centroid_4(1)/image_res_x  
centroid_4_y = centroid_4(2)/image_res_y  
centroid_1d_x = centroid_1d(1)/image_res_x  
centroid_1d_y = centroid_1d(2)/image_res_y  
centroid_2d_x = centroid_2d(1)/image_res_x  
centroid_2d_y = centroid_2d(2)/image_res_y  
centroid_3d_x = centroid_3d(1)/image_res_x  
centroid_3d_y = centroid_3d(2)/image_res_y  
centroid_4d_x = centroid_4d(1)/image_res_x  
centroid_4d_y = centroid_4d(2)/image_res_y
```

Calculate the length between the two speckles in the undeformed image

```
s1 = sqrt ((centroid_2_x - centroid_1_x)^2 + (centroid_2_y - centroid_1_y)^2)  
s2 = sqrt ((centroid_3_x - centroid_1_x)^2 + (centroid_3_y - centroid_1_y)^2)  
s3 = sqrt ((centroid_4_x - centroid_1_x)^2 + (centroid_4_y - centroid_1_y)^2)
```

% Calculate the length between the two speckles in the deformed image

```
s1d = sqrt ((centroid_2d_x - centroid_1d_x)^2 + (centroid_2d_y - centroid_1d_y)^2)  
s2d = sqrt ((centroid_3d_x - centroid_1d_x)^2 + (centroid_3d_y - centroid_1d_y)^2)  
s3d = sqrt ((centroid_4d_x - centroid_1d_x)^2 + (centroid_4d_y - centroid_1d_y)^2)
```

Calculate the relative change in distance between the two speckles

```
strain_1 = (s1d - s1)/s1  
strain_2 = (s2d - s2)/s2  
strain_3 = (s3d - s3)/s3
```

Calculate the orientations of the line element between the two speckles in undeformed image

```
cos_x1 = (centroid_2_x - centroid_1_x)/s1  
cos_x2 = (centroid_3_x - centroid_1_x)/s2  
cos_x3 = (centroid_4_x - centroid_1_x)/s3  
cos_y1 = (centroid_2_y - centroid_1_y)/s1  
cos_y2 = (centroid_3_y - centroid_1_y)/s2  
cos_y3 = (centroid_4_y - centroid_1_y)/s3
```

The embedded Geometric Approach Equation is applied to solve the three simultaneous equations

```
a = [cos_x1^2 cos_y1^2 2*cos_x1*cos_y1  
     cos_x2^2 cos_y2^2 2*cos_x2*cos_y2  
     cos_x3^2 cos_y3^2 2*cos_x3*cos_y3];
```

```
b = [strain_1*(1+0.5*(strain_1))  
     strain_2*(1+0.5*(strain_2))  
     strain_3*(1+0.5*(strain_3))];
```

Solve the three simultaneous equations and determine the strain values

```
c = inv (a)*b;
```

The obtained strain values are displayed in the MATLAB command windows

```
str_1 = ['Exx = ' num2str(c(1))];  
disp (str_1)  
str_2 = ['Eyy = ' num2str(c(2))];  
disp (str_2)  
str_3 = ['Exy = ' num2str(c(3))];  
disp (str_3)
```

APPENDIX C

STRESS-STRAIN CURVES FOR THE MILD STEEL SPECIMENS

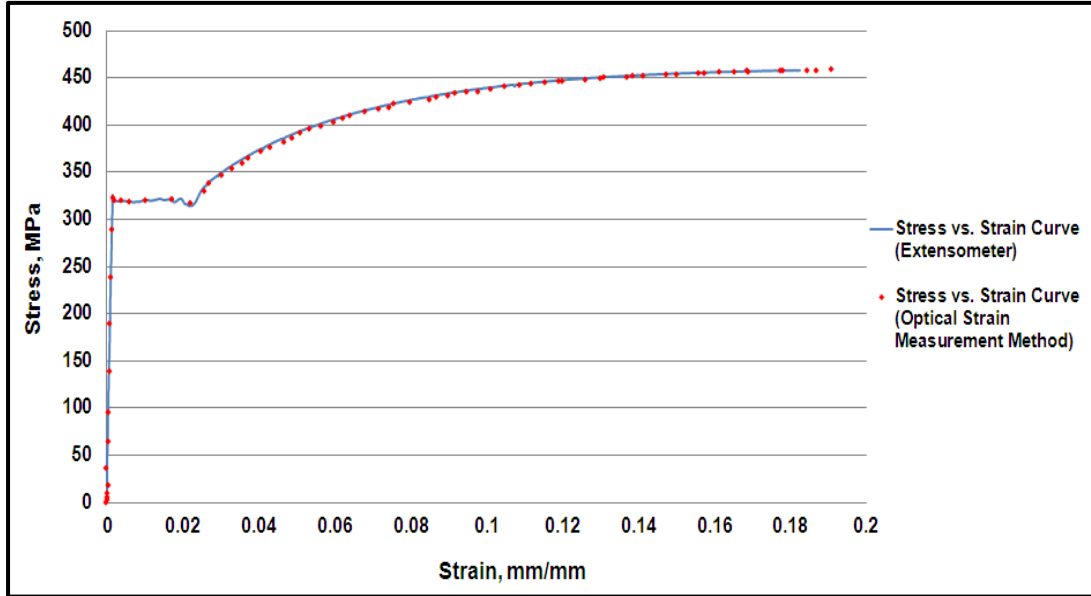


Fig. 1 Stress-strain curve for the second mild steel specimen

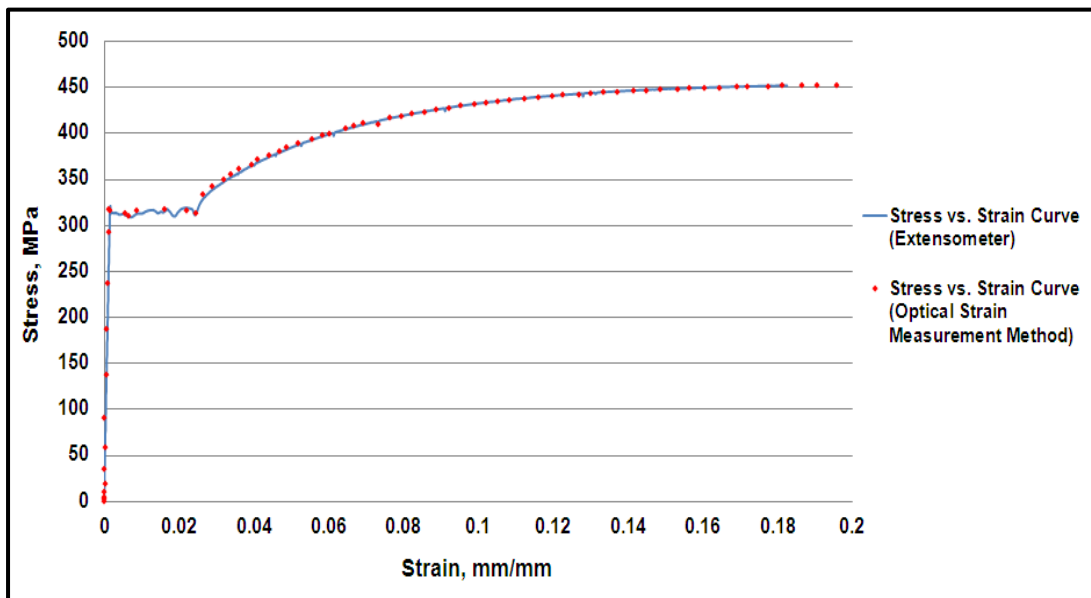


Fig. 2 Stress-strain curve for the third mild steel specimen

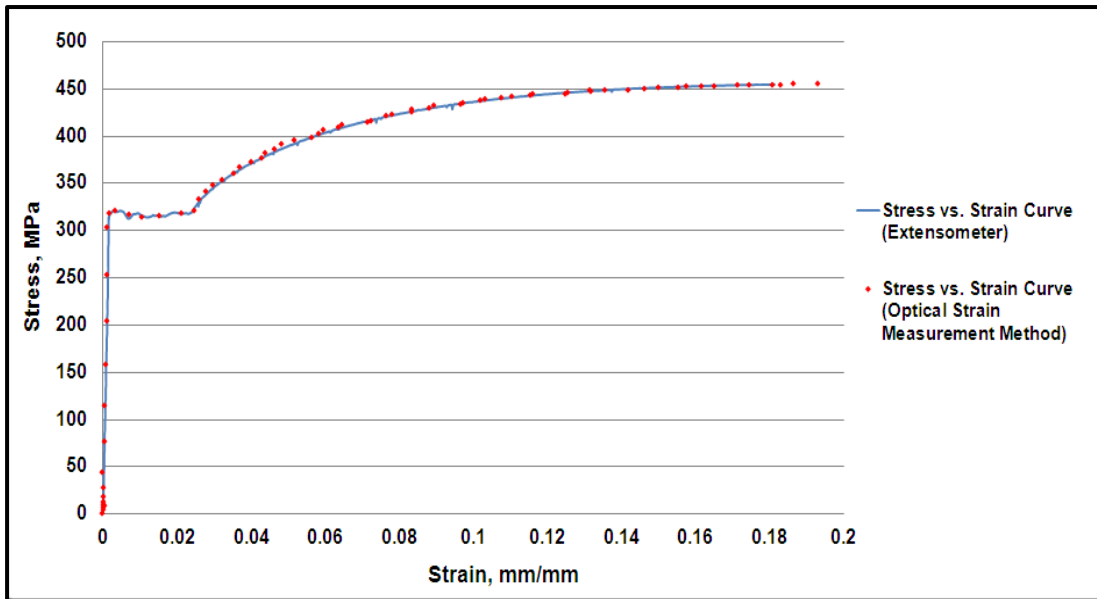


Fig. 3 Stress-strain curve for the fourth mild steel specimen

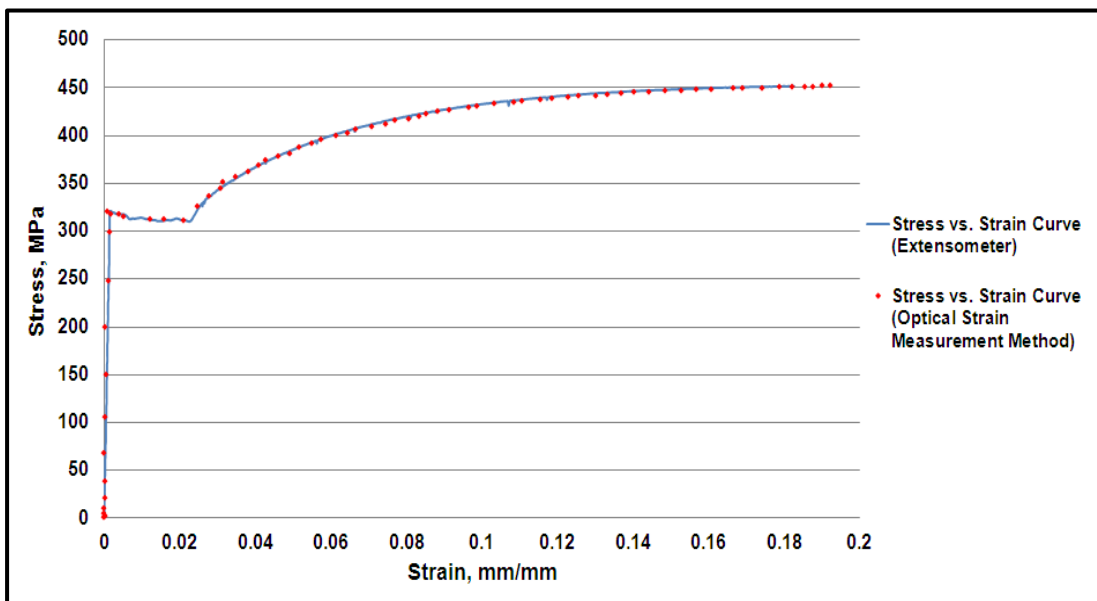


Fig. 4 Stress-strain curve for the fifth mild steel specimen

APPENDIX D

STRESS-STRAIN CURVES FOR THE POLYPROPYLENE SPECIMENS

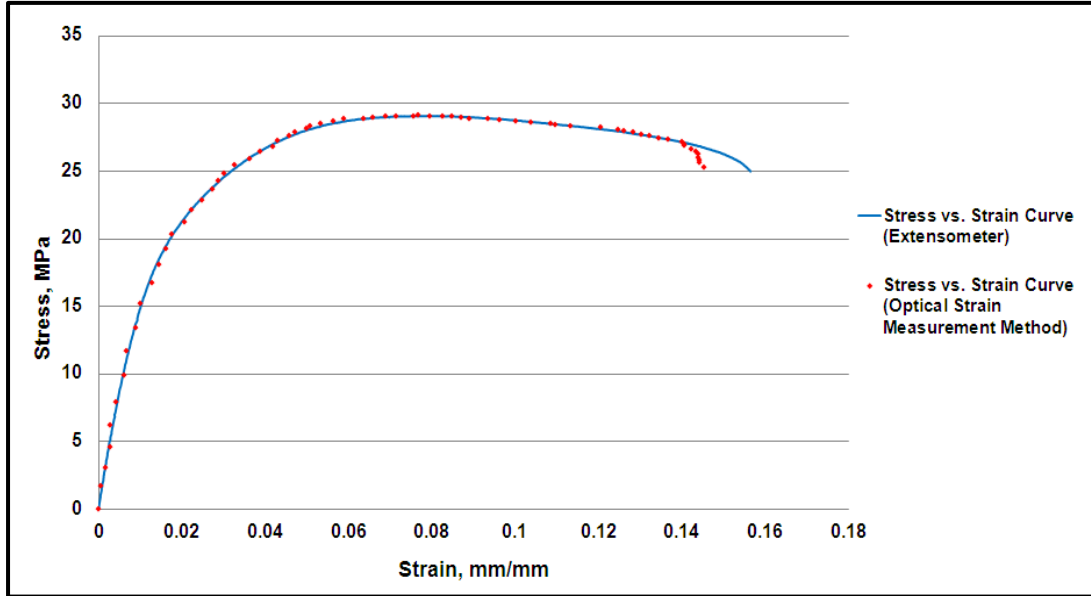


Fig. 1 Stress-strain curve for the second polypropylene specimen

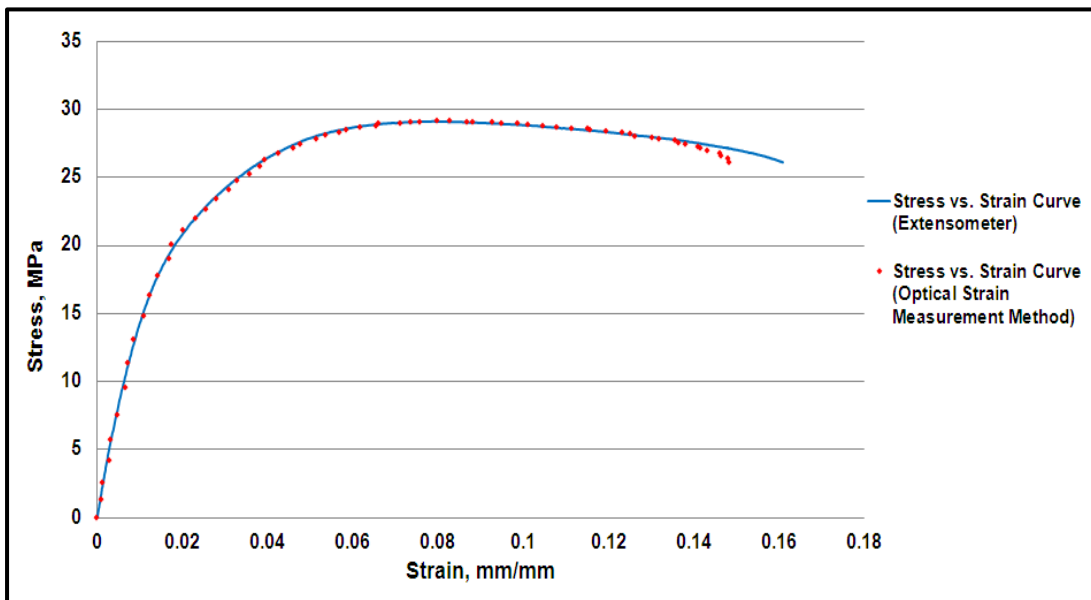


Fig. 2 Stress-strain curve for the third polypropylene specimen

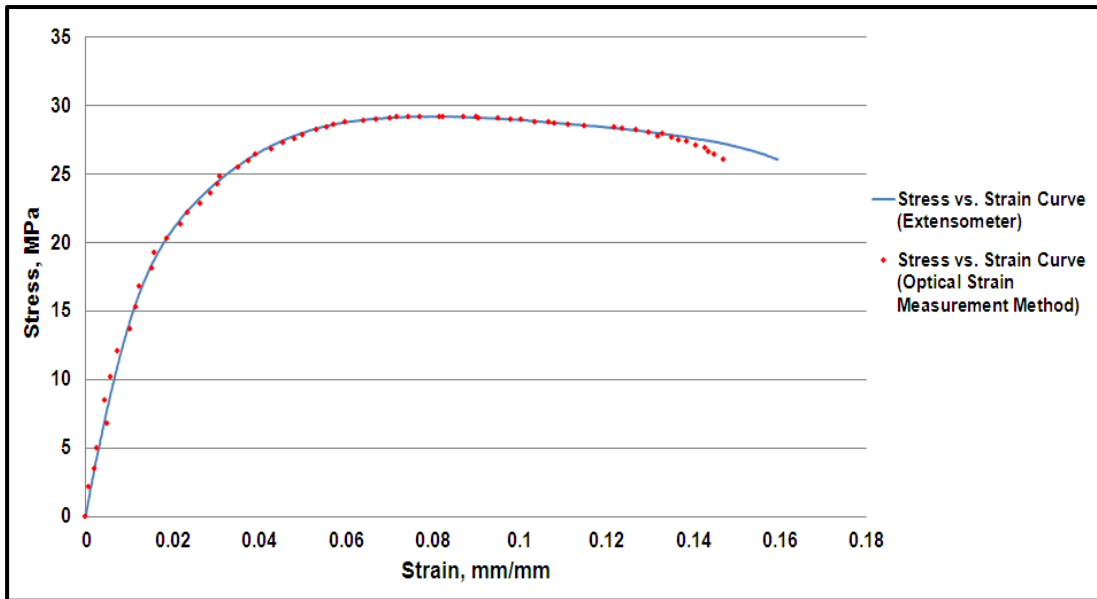


Fig. 3 Stress-strain curve for the fourth polypropylene specimen

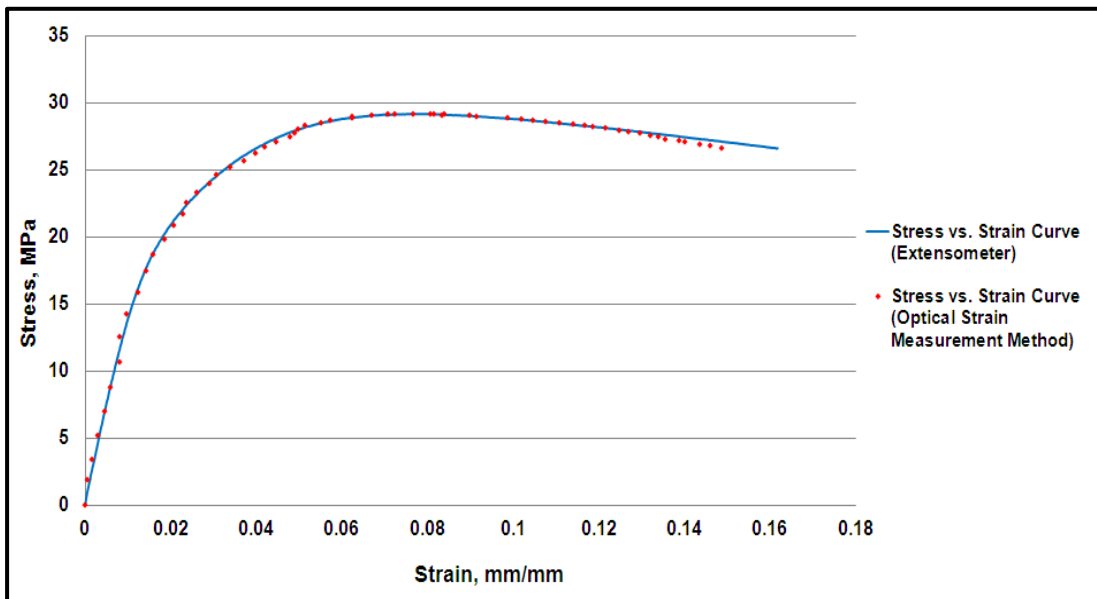


Fig. 4 Stress-strain curve for the fifth polypropylene specimen

APPENDIX E

DETERMINATION OF THE MODULUS OF ELASTICITY FOR THE MILD STEEL SPECIMENS

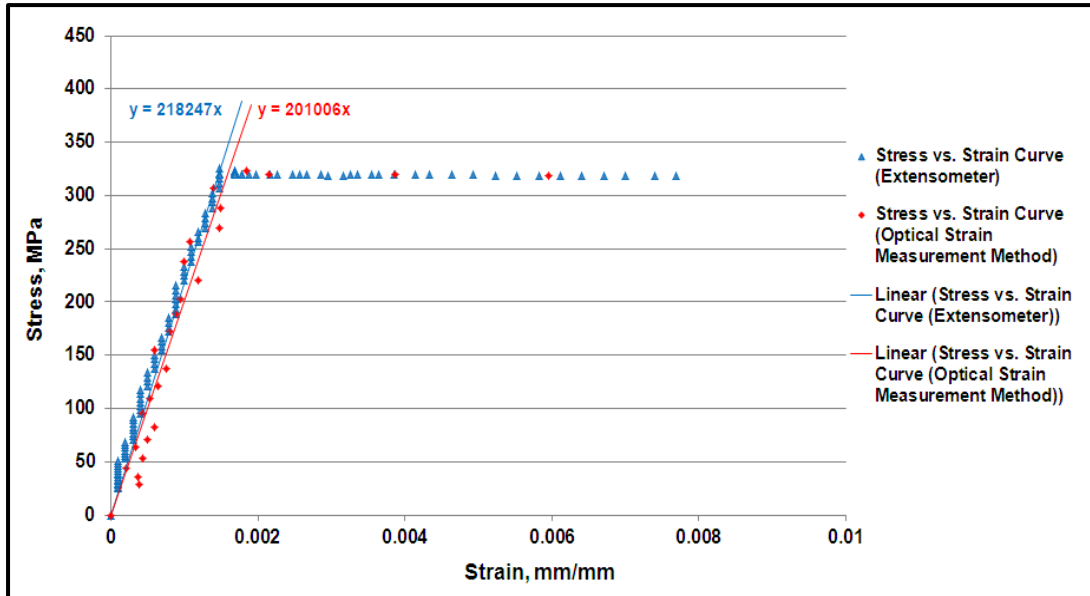


Fig. 1 Determination of the modulus of elasticity for the second mild steel specimen

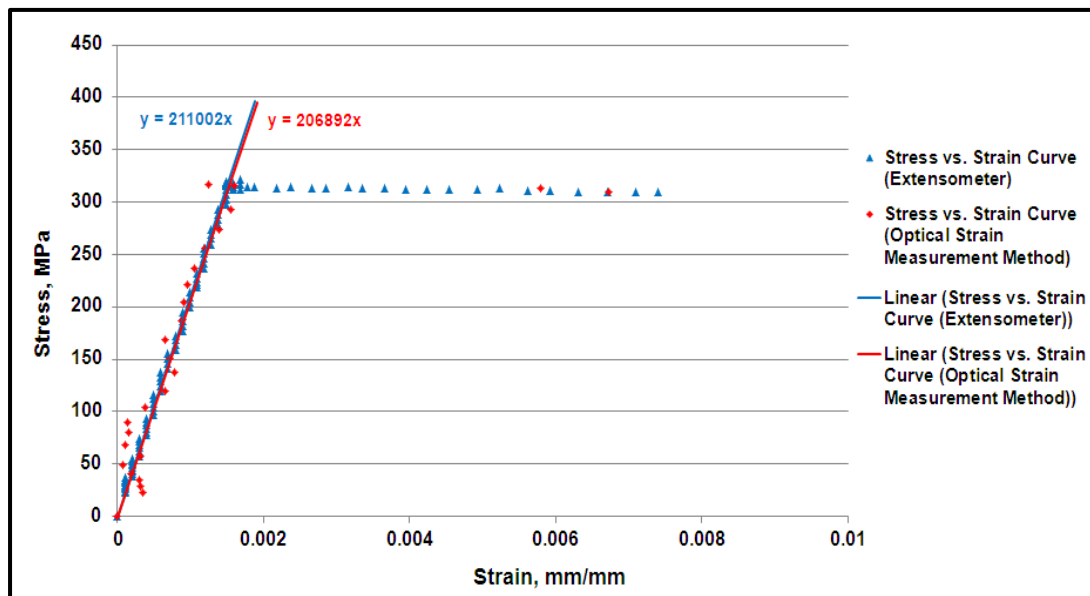


Fig. 2 Determination of the modulus of elasticity for the third mild steel specimen

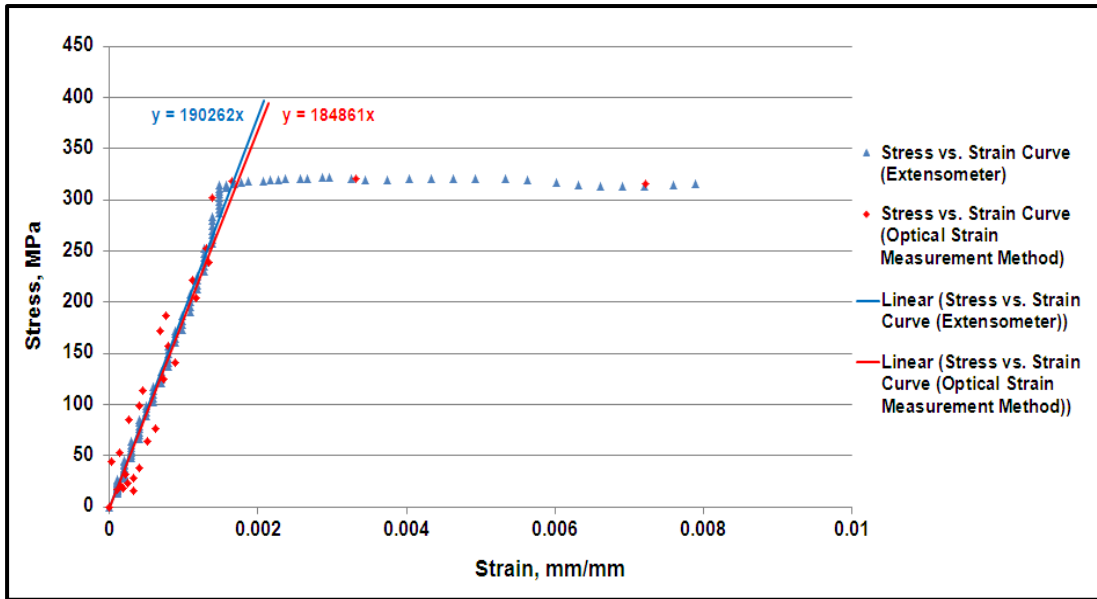


Fig. 3 Determination of the modulus of elasticity for the fourth mild steel specimen

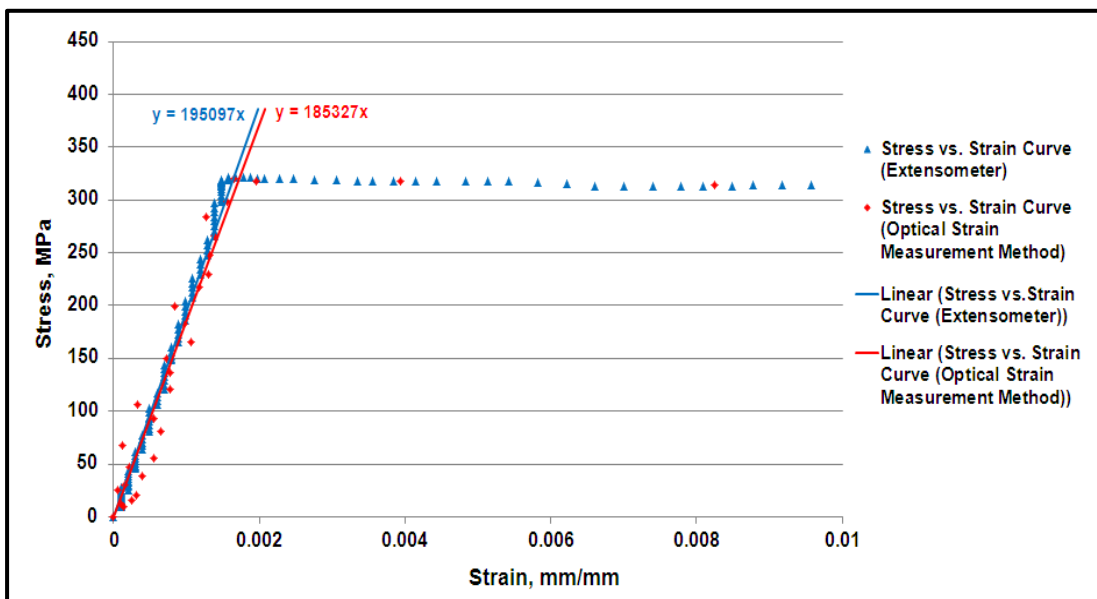


Fig. 4 Determination of the modulus of elasticity for the fifth mild steel specimen

APPENDIX F

DETERMINATION OF THE MODULUS OF ELASTICITY FOR THE POLYPROPYLENE SPECIMENS

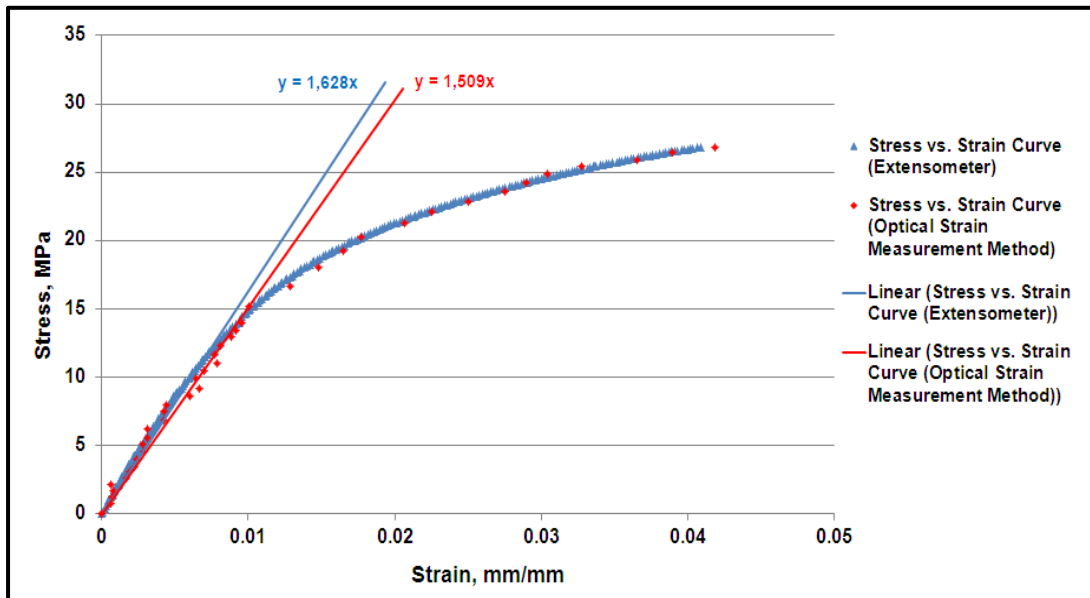


Fig. 1 Determination of the modulus of elasticity for the second polypropylene specimen

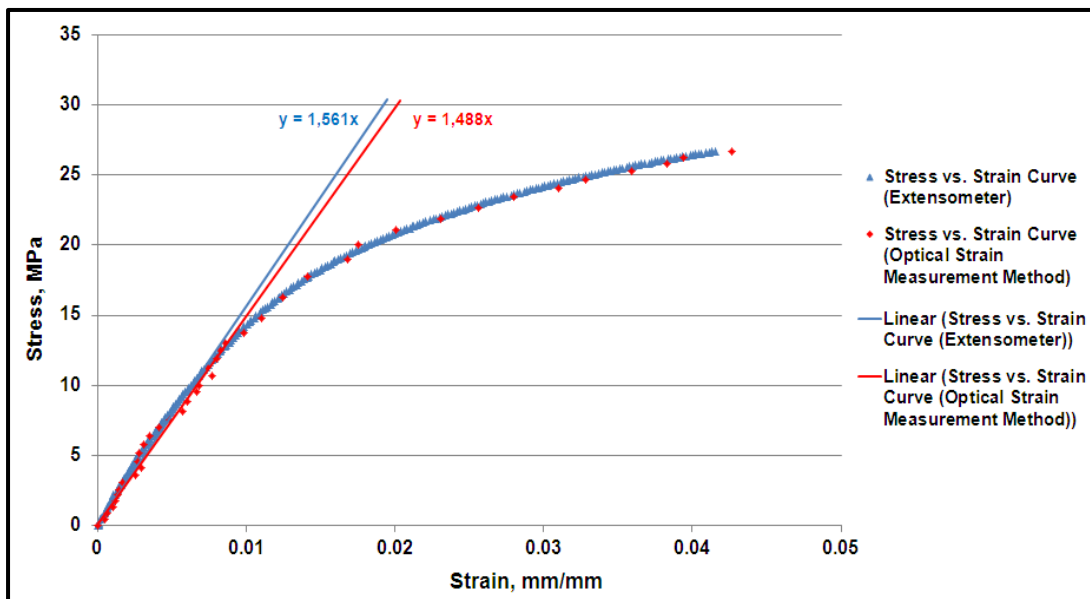


Fig. 2 Determination of the modulus of elasticity for the third polypropylene specimen

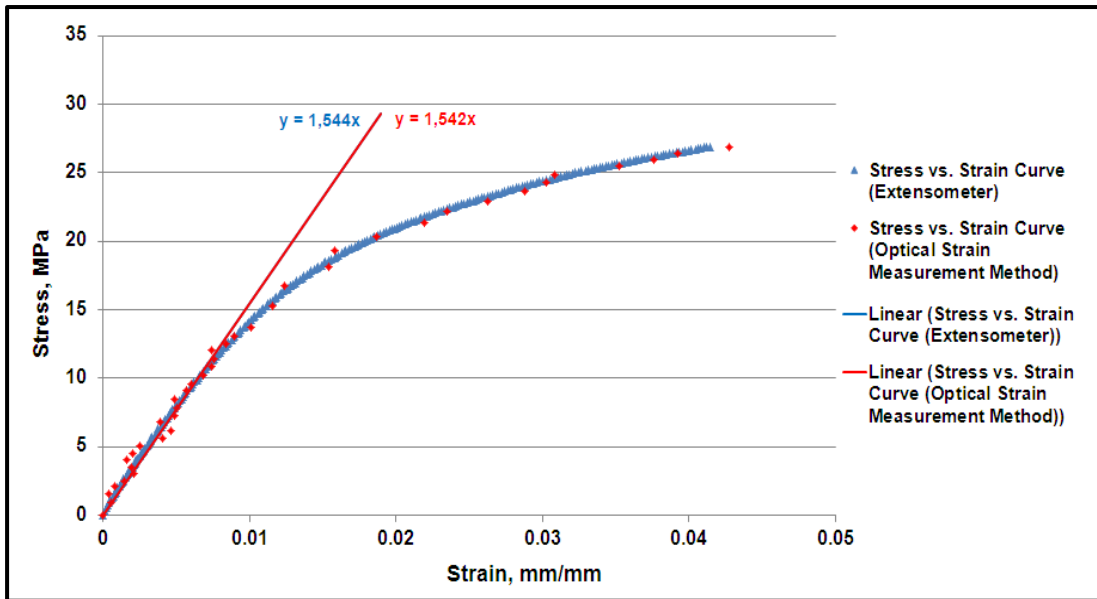


Fig. 3 Determination of the modulus of elasticity for the fourth polypropylene specimen

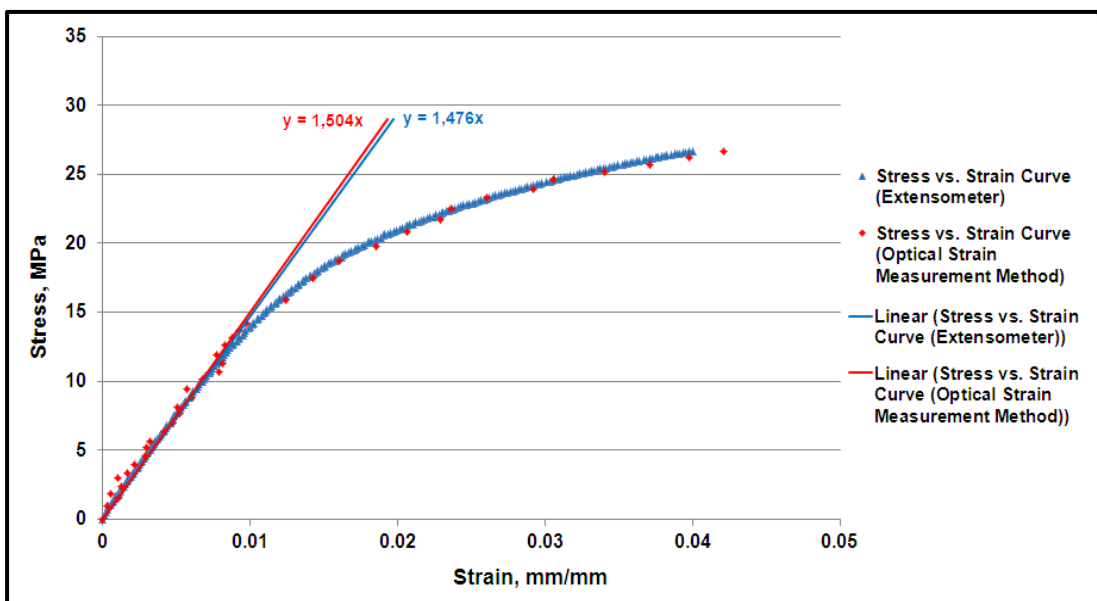


Fig. 4 Determination of the modulus of elasticity for the fifth polypropylene specimen